Deep-ultraviolet frequency metrology with a narrowband titanium:sapphire laser

VRIJE UNIVERSITEIT

Deep-ultraviolet frequency metrology with a narrowband titanium:sapphire laser

ACADEMISCH PROEFSCHRIFT

ter verkrijging van de graad Doctor aan
de Vrije Universiteit Amsterdam,
op gezag van de rector magnificus
prof.dr. L.M. Bouter,
in het openbaar te verdedigen
ten overstaan van de promotiecommissie
van de faculteit der Exacte Wetenschappen
op donderdag 24 mei 2007 om 15.45 uur
in het auditorium van de universiteit
De Boelelaan 1105

door

Sandro Hannemann

geboren te Treuenbrietzen, Duitsland

promotor: prof.dr. W.M.G. Ubachs
copromotor: dr. E.-J. van Duijn

Für Jule und Jannik

Science is a way of trying not to fool yourself.
The first principle is that you must not fool yourself,
and you are the easiest person to fool.

When you are solving a problem, don't worry.
Now, after you have solved the problem,
then that's the time to worry.

(Richard Feynman)

This thesis was reviewed by:

Prof. Dr. W. M. G. Ubachs (promotor)
Dr. E.-J. van Duijn (copromotor)

And by the members of the reading committee:

Prof. Dr. W. Hogervorst (Vrije Universiteit)
Prof. Dr. H. B. van Linden van den Heuvell (Universiteit van Amsterdam)
Prof. Dr. W. L. Meerts (Radboud Universiteit Nijmegen / Vrije Universiteit)
Prof. Dr. F. Merkt (ETH Zürich, Switzerland)
Prof. Dr. M. Weidemüller (Albert Ludwigs Universität, Freiburg, Germany)

An online-pdf version of this thesis is available at:
http://www.ubvu.vu.nl/dissertations/getpdf.cfm?promid=7954

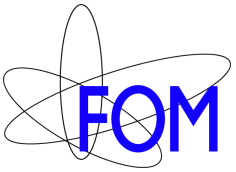

The work described in this thesis was performed as part of the research program of the “Stichting voor Fundamenteel Onderzoek der Materie” (FOM) and was carried out at the Laser Centre of the Vrije Universiteit Amsterdam.

Contents

Chapter 1

Introduction and Summary

The present thesis describes experimental investigations in the fields of laser physics and laser spectroscopy. A laser system was built, initially for the purpose of generating extreme ultraviolet (XUV) radiation by means of resonance-enhanced four-wave mixing (REFWM). Though an experiment on REFWM was successfully carried out and is presented in chapter 6, focus changed during the course of the investigations towards precision metrologies in the deep ultraviolet (UV) wavelength range.

The laser system built at the start of the project is an injection-seeded pulsed titanium:sapphire oscillator-amplifier system. Pulsed operation is achieved using gain-switched oscillation in a low-finesse cavity. In order to further enhance the output intensity, external traveling wave amplification in a bow-tie setup is applied. The pulsed output combines high peak intensities in typical durations of $\approx 20\,\mathrm{ns}$ with relatively narrow bandwidths of $\approx 20\,\mathrm{MHz}$. The laser system is suitable for frequency upconversion to produce narrow bandwidth pulses in the ultraviolet and deep-ultraviolet wavelength ranges that can be applied in high resolution spectroscopies.

In order to perform high precision metrology, the injection seeding light is referenced to absolute frequency standards: to Doppler-free saturable absorption spectroscopy on iodine, or to a femto-second frequency comb. These options for precise absolute calibration made it necessary to investigate, whether or not the pulsed output of the oscillator-amplifier system exhibits the same center-frequency as the provided injection seeded light. The utilized method described in Chapters 2 and 5 is a single-shot technique known as "chirp-analysis". It is performed and taken into account simultaneously during the spectroscopic scans. Application of this technique reduces the uncertainty budget for the absolute frequency calibration by more than an order of magnitude — precision at the MHz level is achieved and available over a wide wavelength range.

For precise laser frequency calibrations a special method to reduce first order Doppler shifts in crossed atomic/molecular and laser beam setups using a Sagnac interferometer was implemented. The method, presented in chapter 3, is based on optimizing the spatial overlap of two counterpropagating beams — both being part of the interferometer. When aligned perfectly, the interferometer exit port shows

a “dark fringe” and both beams are subject to identical Doppler shifts of opposite signs. Minute deviations from perfect antiparallelism are indicated by fringe patterns. This ‘Sagnac’ technique reduces experimental frequency uncertainties related to Doppler shifts in crossed atomic/molecular and laser beam experiments to a level below systematic uncertainties resulting from the laser characteristics. The ‘Sagnac’ method is helpful wherever classic Doppler-free methods are difficult to implement, e.g. at deep-UV and vacuum-UV transitions exhibiting high saturation intensity. Moreover, Doppler-free methods are only Doppler-free in the sense of ’not broadened’ but subject to Doppler-shifting when applied to samples exhibiting non-isotropic velocity distributions — e.g. atomic beams. In such cases it is essential to align the two counterpropagating beams in perfect overlap. The ‘Sagnac’ method of Doppler-reduction is demonstrated both for one-photon and two-photon spectroscopies.

The combination of narrow bandwidth, controlled chirp characteristics, pulsed operation for efficient upconversion, minimization of Doppler shifts using interferometric techniques, and a precise absolute frequency reference (a phase-locked femto-second frequency comb) made it possible to attain accuracy levels below 10^{-9} over a wide wavelength range. The wide tunability range of the laser active medium and the achievable accuracy of the frequency calibration makes this light source a versatile tool for different methods of precision spectroscopy. In the framework of the project the deep UV output (fourth harmonic) was applied in a cavity ring-down spectroscopy (CRDS) scheme, for light-induced fluorescence (LIF) spectroscopy, for Doppler-free two-photon excitation, and for REFWM.

The thesis is organized as follows: In chapter 2 the titanium:sapphire laser source is described in detail. The laser dynamics of the oscillator is quantitatively characterized, at different pump pulse energies and seeding wavelengths. In view of the frequency metrologic applications, the instantaneous frequency dynamics of the pulsed output is measured and characterized in detail. Means to control the frequency dynamics are identified and employed in precision metrologies presented in chapters 3 – 5. The influence of the multi-pass amplification on the spectral and temporal pulse shape is investigated. Optically induced refractive index changes in titanium:sapphire are quantified as well.

In Chapter 3 the Sagnac-interferometric method for reducing first order Doppler-shifts is described and demonstrated. The atomic ytterbium $6s^2 \rightarrow 6s\,30p_{3/2}$ $J = 1$ one-photon transition at 199 nm is investigated in a LIF detection scheme and the $4p^6 \rightarrow 4p^5 5p[1/2]_0$ transition in krypton gas is recalibrated in a TOF detection scheme. Experimental frequency uncertainties are reduced to the 6×10^{-10} accuracy level, at which systematic effects arising from the laser characteristics are dominating.

In Chapter 4 the $3s^2\,{}^1S \rightarrow 3s4p\,{}^1P$ transition in atomic magnesium near 202.5 nm is calibrated to the 1 MHz (7×10^{-10}) precision level. This experiment was motivated by a technical interest of achieving the highest accuracy in a spectroscopic experiment using nanosecond pulsed laser sources. Moreover, this line is a candidate

for inclusion in many-multiplet methods for comparison with quasar absorption spectra in order to detect a possible change in the fine-structure constant α.[1] This research requires precise laboratory data for reference frequencies at zero red-shift.[2]

Chapter 5 addresses frequency metrology on the EF $^1\Sigma_g^+ \leftarrow$ X $^1\Sigma_g^+(0,0)$ two-photon transition in molecular hydrogen and isotopomers. The EF state is of particular interest, because different precise measurements of ionization and dissociation limits exist which are calibrated relative to the EF double-well state. Hence, absolute calibration of the EF state will improve the known values of the ionization and dissociation limits, which are an important test ground for *ab initio* calculations. The attained accuracy of the measured EF $\leftarrow$ X transitions is 10^{-9}.

A demonstration of resonance-enhanced four-wave mixing using the fourth harmonic of the laser system at 212.5 nm for exciting the Kr $4p^6 \rightarrow 4p^5 5p[1/2]_0$ resonance is presented in Chapter 6. For this experiment a noncollinear sum-frequency mixing scheme was applied in a pulsed gas jet which allowed for selecting the light at desired wavelength $\lambda \approx 91$ nm simply by adjusting a slit rather than using a grating. Lines of the b$' \leftarrow$ X (8–0) band and the b $\leftarrow$ X (12–0) band in molecular nitrogen and of the B $\leftarrow$ X (19–0) Lyman band in molecular hydrogen are calibrated. The latter spectral lines are part of the database of H_2 spectra that can be used for probing a possible time variation of the proton-electron mass ratio on a cosmological timescale.[3]

In Chapter 7 cavity ring-down spectroscopy (CRDS) at deep UV wavelengths $\lambda = 197 - 204$ nm is presented — the shortest wavelengths ever applied in a CRDS scheme. Extinction cross sections in various gases were measured. Schumann-Runge (SR) bands in O_2, thereby resolving the fine-structure, and extinction cross sections in the Herzberg continuum of O_2 are measured.

In Chapter 8 detailed CRD spectroscopy on the Schumann-Runge (2–0), (1–0), (0–0), (2–1) bands in $^{16}O_2$ and on the (1–0), (0–0) bands in $^{18}O_2$ is presented. The resolution of the spectroscopic scans helped improving the accuracy of the values of the molecular constants. Since the SR bands represent the first dipole allowed transition in molecular oxygen, these spectral features are important in connection to UV light absorption in Earth's atmosphere. Detailed knowledge of the molecular constants is needed for modeling the radiation budget in the atmosphere. Additionally, in Chapter 9 the high resolution of the laser was used to investigate collision broadening and shifting parameters on the B $^3\Sigma_u^-$, $v = 0$ state. From a combined set of laser induced fluorescence and CRDS measurements fine-structure dependent predissociation rates for the B $^3\Sigma_u^-$, $v = 0$, F_i states were obtained.

The wide range of demonstrated applications and the convenient characteristics of the laser, most notably its wide tunability, efficient upconversion, reliable solid state active medium, and the availability of means for absolute calibration, prove that the developed laser system is a versatile tool in a spectroscopy lab.

Chapter 2

A narrow-band injection-seeded titanium:sapphire oscillator-amplifier system

A narrow band and tunable injection-seeded pulsed titanium:sapphire lasersystem has been developed for application in high-resolution spectroscopic studies at the fundamental wavelengths in the near-infrared as well as in the ultraviolet, deep ultraviolet, and extreme ultraviolet after upconversion. Special focus is on the quantitative assessment of the frequency characteristics of the oscillator-amplifier system. Frequency offsets between continuous wave seed-light and the pulsed output are measured as well as linear chirps attributed mainly to mode-pulling effects in the oscillator cavity. Operational conditions of the laser are found in which these offset and chirp effects are minimal. Absolute frequency calibration at the MHz level of accuracy is demonstrated on various atomic and molecular resonance lines.

2.1 Introduction

Titanium:sapphire (Ti:sapphire, Ti:Al_2O_3) lasers share the advantages of broad wavelength coverage and tunability with the ease-of-use of an all-solid-state laser system. Besides continuous-wave lasing at ultra-narrow bandwidths, and employing the Kerr-lens mode-locking characteristic of the Ti:sapphire material to produce ultrashort laser pulses, pulsed lasing of Ti:sapphire in the nanosecond domain is a third often-used mode of operation. In applications where both narrow bandwidth and laser intensity are important, such as in non-linear spectroscopic applications as well as in LIDAR experiments, a ns pulsed Ti:sapphire may be a system of choice. In particular satellite-based LIDAR systems benefit from the advantageous characteristics and the all-solid-state design of pulsed Ti:sapphire lasers.

In view of the fact that Ti:Al_2O_3 exhibits a rather long excited state lifetime of 3.15 μs,[4] the laser pulses generated in Ti:sapphire do not straightforwardly copy the pulse structure of typical Q-switched pump lasers, as is the case for dye lasers.

Moreover, the broad gain profile requires careful wavelength selection, if the goal is narrow bandwidth single longitudinal mode (SLM) operation. In an early study by Brockman *et al.*[5] both the pulse structure and wavelength selection were accomplished by injection-seeding with the output of a pulsed dye laser. Injection-seeding has remained a persistent theme in the design of narrowband pulsed Ti:sapphire lasers. Georges *et al.*[6] have shown that in injection-seeded passive amplifiers, gain saturation in combination with an appropriate number of traversals through the medium, provides desired pulse durations down to 20 ns. Rhines and Moulton[7] demonstrated SLM operation of a pulsed Ti:sapphire resonator by injection seeding with the output of a CW Ti:sapphire laser, while Bair *et al.*[8] and Raymond and Smith[9] showed that the low seed-power of a CW diode laser was sufficient to produce narrowband 30 ns pulses.

In recent years further developments of pulsed Ti:sapphire lasers have been pursued along various directions. Brandi *et al.*[10] have generated Fourier-transform (FT) limited laser pulses in excess of 200 mJ at durations of 300 ps. The high peak intensities delivered were upconverted in gaseous jets to produce FT-limited pulses at XUV wavelengths as low as 40 nm.[11] Merkt and coworkers followed a different strategy also aiming at producing narrowband XUV radiation. They pre-programmed pulse envelopes, in the range of durations between 10 ns and 1 μs, by AOM-intensity modulating the output of a cw Ti:sapphire laser and subsequently amplifying these in a series of multipass amplifiers; this led to XUV pulses at bandwidths as low as 55 MHz.[12] Dupré and Miller extended the development of injection-seeded pulsed Ti:sapphire lasers, focusing on methods to optimize cavity stabilization, to achieve pulse energies of 100 mJ at bandwidths as low as 12 – 30 MHz (FWHM) for use in high resolution spectroscopy.[13]

When using injection-seeded pulsed laser systems in high-resolution spectroscopic applications, either at the fundamental wavelength or at generated harmonics, effects of time-dependent gain in the amplifier will give rise to phase excursions deviating from the carrier wave. These result in a phenomenon known as chirp: time-dependent variations of the output frequency of the laser over the time period of the pulse. The chirp effects may cause a net-offset between the carrier frequency and the time-averaged frequency of the pulse and result in problems with frequency calibration of the spectroscopic lines under study. Such calibration problems were already identified by Wieman and Hänsch in the early study of atomic hydrogen,[14] where dye lasers were used. Chu and coworkers[15,16] addressed the chirp issues of dye-amplifiers and their consequences for precise frequency calibration in relation to spectroscopy of positronium. Eyler and coworkers[17,18] thereupon investigated the phase dynamics of dye amplifiers in further detail, while Reinhard *et al.*[19] and Eikema *et al.*[20] developed methods to compensate for chirp effects by manipulating the phase of the seed-light via an electro-optic modulator before amplification.

While the chirp phenomenon in traveling-wave dye-amplifiers originates in time-dependence of the gain in the lasing medium, solid-state oscillator laser cavities exhibit similar frequency excursions, although these have a different cause. Here, as a

result of a change of refractive index in the gain material during gain build-up, the optical path length of the cavity changes during the creation of the population inversion; as a result the frequency of the generated pulse does not coincide with the seed-frequency to which the empty cavity is locked; this phenomenon is a frequency-pulling effect and may be associated with chirp during the pulse. Such phenomena have been studied in alexandrite lasers[21] as well as in optical parametric oscillator devices.[22–25]

In this paper we describe the operation of a pulsed Ti:sapphire laser system consisting of an injection-seeded oscillator and a bow-tie amplifier. In the characterization the frequency pulling and chirp effects are measured and quantified, while methods to reduce these disturbing effects for high-resolution application of the system are discussed as well.

2.2 Design and operation of the laser system

2.2.1 The Ti:sapphire oscillator

The Ti:sapphire laser system consists of two main components: the oscillator cavity in which nanosecond pulses are generated and the amplifier, where the cavity output is further enhanced for subsequent efficient harmonic generation. The pulsed Ti:sapphire oscillator is built in the form of a stable ring cavity in which a Brewster-cut Ti:sapphire crystal of length 1.57 cm and front area $4 \times 4\,\mathrm{mm}^2$ is placed. The titanium-ion doping is chosen such, that 90 % of the pump light at 532 nm is absorbed over the length of the crystal. A schematic view of the setup is shown in Fig. 2.1. The cavity length of 40 cm corresponds to a longitudinal mode spacing of 750 MHz. The two mirrors close to the crystal are concave with identical radius-of-curvature (ROC) $r = -0.5\,\mathrm{m}$. They have dichroic coatings, designed to transmit the pump light at wavelength 532 nm and to reflect the Ti:sapphire fluorescent light with $R = 99.9\,\%$ efficiency. The remaining mirrors are both flat. One of them is a highly reflective mirror (for Ti:sapphire fluorescence) mounted on a piezo electric actuator in order to control the cavity length using the Hänsch-Couillaud locking scheme.[26] The other one is an output coupling mirror with a typical reflectivity of $R_{\mathrm{oc}} = 90\,\%$. The finesse varies depending on the seeding wavelength and used mirror set and attains values between 20 and 35.

For pumping, the second harmonic light from an injection seeded Q-switched Nd:YAG laser operating at 10 Hz repetition rate (Quanta Ray GCR 3 by Spectra Physics) is used. It provides Fourier-transform (FT) limited pulses of 7 ns duration with a pulse timing root-mean-square (RMS) jitter of 1.1 ns. From the maximum pulsed output of about 250 mJ at 532 nm, a fraction of 12 mJ is branched off for pumping the oscillator. The Ti:sapphire crystal is pumped from two sides in order to increase the maximum amount of pump energy possible to apply without exceeding the damage threshold of the Ti:sapphire crystal surface. The FWHM diameter $d_{\mathrm{p}} = 0.38\,\mathrm{mm}$ of the intensity profile of the pump beam is matched to the cavity mode in the Ti:sapphire crystal.

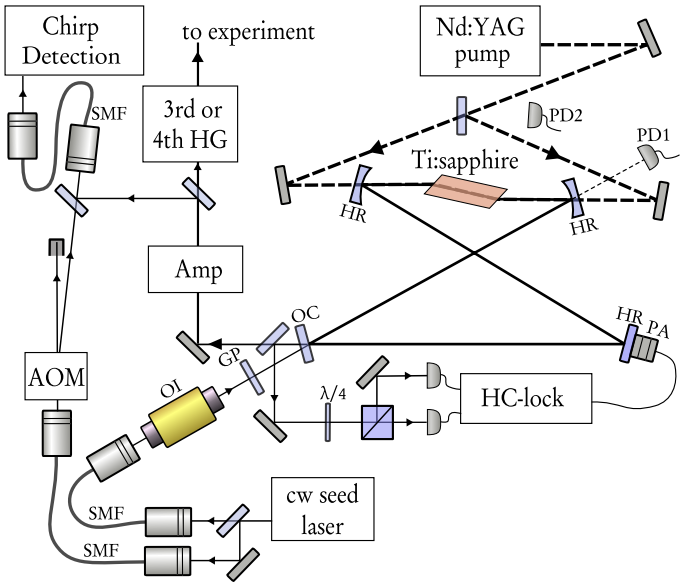

Figure 2.1 – *(color online) Schematic overview on the pulsed Ti:sapphire narrowband oscillator. The cavity contains three high reflective (HR) mirrors, one output coupling mirror (OC) and a Ti:sapphire crystal. One of the HR mirrors is mounted on a piezo actuator (PA) which is for maintaining the cavity length using the Hänsch-Couillaud (HC) locking scheme. For injection seeding light is coupled from a CW laser source through a single mode fiber (SMF). The fiber tip is protected from pulsed amplification with an optical isolator (OI) and a glass plate (GP). The build up process is monitored using two fast photodiodes (Thorlabs DET 210): PD2 detects scattered pump light, PD1 monitors cavity leak-out. The amplifier (Amp) is depicted in Fig. 2.2.*

Pumping the bare cavity without injection seeding produces broadband superfluorescence pulses in both directions. In order to obtain FT-limited pulses at a defined and controllable wavelength the cavity is injection seeded using a few mW of CW light from a Ti:sapphire ring laser (Coherent 899) or from an external cavity diode laser (Toptica DL 100) coupled through a single-mode polarization maintaining fiber. In order to protect the fiber tip from destructive effects of pulsed light traveling back to the aligned fiber, an optical isolator and a glass plate are placed between fiber tip and cavity. The idea of the glass plate is the following: when aligned properly — at normal angle of incidence with the cavity mode — the amplified fluorescence propagating in the "wrong" direction towards the fiber tip is partially reflected ($R = 4\,\%$) by the glass plate into the "right" direction. By this means, part of the gain into the "wrong" direction is transfered to the gain at "right" direction leading to an almost complete extinction of the amplification towards the fiber tip, while the pulse is formed. Thus the glass plate ensures unidirectional pulse generation even for a non-seeded cavity providing additional safety for the tip.

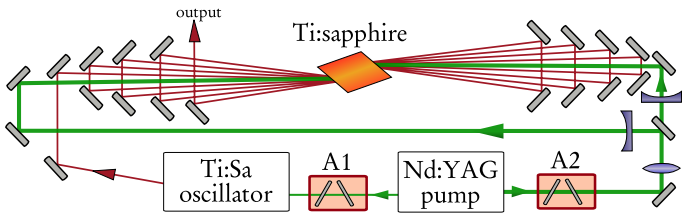

Figure 2.2 – *(color online) Schematic overview on the multi-pass amplifier system. The pump energies for both the oscillator and the amplifier can be varied between zero and full power using adjustable attenuators.*

2.2.2 The Ti:sapphire amplifier

Since the spatial cavity mode is rather narrow — with typical beam diameters of about 0.5 mm — the maximum output energy is restricted by the damage thresholds of the surfaces of the mirrors and the Ti:sapphire crystal. Pulse energies of up to 1 mJ can be generated from the Ti:sapphire oscillator. However, for reducing the probability of optical damage, typical output energies of 0.2 – 0.7 mJ are used. In order to enhance the pulse energies to about 10 – 40 mJ, an external multi-path bow-tie shaped amplifier is available which is schematically depicted in Fig. 2.2. It is pumped from two sides using the major part of the green output of the Nd:YAG laser which pumps the oscillator. The amplification can be varied using an adjustable pump light attenuator or by varying the number of amplification steps through the crystal.

2.2.3 Frequency upconversion

For most spectroscopic applications carried out with the Ti:sapphire laser system, harmonics of the near infrared output are used. In Fig. 2.3 the frequency upconversion setup as it has been used for the fourth harmonic is depicted. It involves second harmonic generation (SHG) using a BBO cut at $\vartheta = 30°$, subsequent frequency mixing of the second harmonic with the fundamental frequency light using a BBO $\vartheta = 45°$, and finally mixing the third harmonic with the fundamental frequency provided by the remainder of the SHG stage in BBO $\vartheta = 65°$.

All mixing stages use Type-I phase-matching, for which $\lambda/2$-retarder plates are placed to adjust the polarization planes of the second harmonic and of the third harmonic in front of the next upconversion step. The advantage of such a mixing scheme over a simpler double SHG scheme is its wide tunability range. While a double SHG system provides phase matching for $\lambda > 206\,\text{nm}$, the mixing scheme over three upconversion stages extends the working range to $\lambda > 189\,\text{nm}$ limited by the absorption wavelength of BBO.

The achieved upconversion efficiencies are 50 % for the SHG, 30 % of the blue for the third harmonic, and finally about 10 % of the third harmonic for the fourth

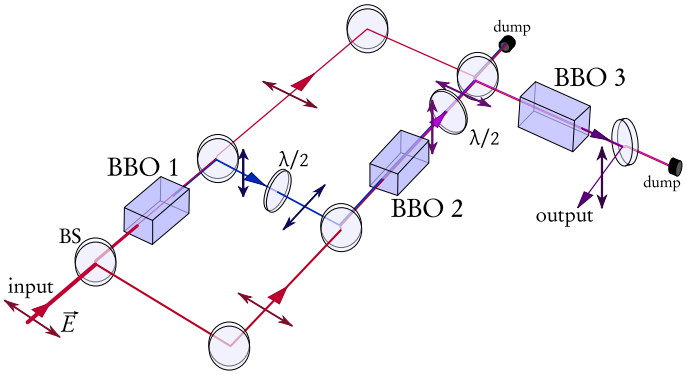

Figure 2.3 – *(color online) Schematic overview of the upconversion stages for the production of up to the fourth harmonic. The polarization planes are indicated with arrowed lines. All phase matching is of Type-I. λ/2-retardation plates turn the polarization to the desired plane.*

harmonic. The maximum output energies obtained at 212 – 196 nm were 0.1 – 0.3 mJ. For the double SHG stage system larger output energies are achieved since it involves only two nonlinear conversion stages. For infrared output energies of about 16 mJ, output energies of 2 mJ were reached at $\lambda = 212$ nm.

2.3 Results on laser operation

In this section the focus is on the following properties of the Ti:sapphire oscillator: the build-up time and pulse length of the generated infrared pulses, the energy conversion efficiency, possible frequency chirps and offsets between seed light and produced pulses. It will be investigated, how those characteristics depend on the seeding wavelength and the pump energy provided, their shot-to-shot statistics, and the influence of the Hänsch–Couillaud locking. Additionally the effects of the amplifier on the pulse will be discussed, and results of indirect measurements of the bandwidth of the generated pulses will be presented.

2.3.1 Pulse build-up time and pulse length

First of all, the lasing dynamics of the cavity determining both the time delay between pump pulse arrival and infra-red pulse generation and the pulse duration are investigated. In Fig. 2.4 oscilloscope traces of a typical pulse timing sequence are shown. It depicts the signals of the fast photodiodes (Thorlabs DET 210) PD1 and PD2 (see Fig. 2.1) registered on a fast oscilloscope (LeCroy 9360, bandwidth: 600 MHz, sampling rate: 5 Gsample/s). The response time of the photodetection system is estimated to be about 1 ns. PD2 monitors stray light of the pump and PD1 cavity leak-out. The short leading pulse is the 7 ns pump pulse registered by PD2. The other two traces depict the PD1 photodiode signal for seeded and non-seeded

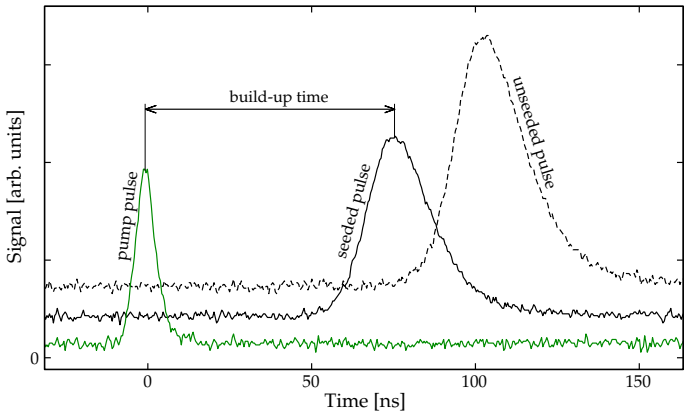

Figure 2.4 – *(color online) Oscilloscope traces of a pulse build-up process inside the cavity registered for one single injection seeded pulse event and one without the seeding. The pump pulse is monitored from scattered light detected by photodiode PD2 (see Fig. 2.1). The two traces with the delayed somewhat longer pulses are taken by photodiode PD1 (Fig. 2.1).*

operation. In the following the timing difference between peak intensities of pump and output pulses is defined as pulse build-up time. A correction is made for delays in cables and detection between PD1 and PD2. The full width half maximum (FWHM) of the photodiode signals will be identified with the pulse duration. From Fig. 2.4 it is concluded, that the unseeded build-up process takes somewhat longer than the injection seeded process. This observation is consistent throughout the entire wavelength range (764 – 856 nm) over which the seeding light was tuned.

The dynamics of the build-up process is strongly affected by the pulse energy of the pump laser, because it determines the population inversion and thereby the initial gain in the active laser medium. As the lifetime of the excited state in Ti:sapphire is 3.15 μs[4] the pulse amplification continues over several cavity round trip times until the population inversion is depleted by the amplification process. At the level where laser gain and cavity loss are equal the infrared pulse intensity reaches its maximum; thereafter the gain decreases further and the pulse intensity drops to zero. In the example of Fig. 2.4 the seeded build-up process takes about 70 ns, or correspondingly, 53 cavity round trips.

Since the pump energy determines the strength of the population inversion and likewise the initial gain, it is expected that the build-up time is smaller for higher pump energies. In order to quantitatively investigate this relation the pump energy imposed on the oscillator was varied using an adjustable attenuator. In Fig. 2.5 a measurement is shown where the pump pulse energy is varied from 2 mJ to about 7 mJ. The signals of the photodiodes PD1 and PD2 were monitored and integrated on the oscilloscope after being calibrated using a thermal power meter (Scientech Vector H310). One can see that the pulse production process becomes faster for higher pump pulse energies. It is also apparent, that the pump pulse is suf-

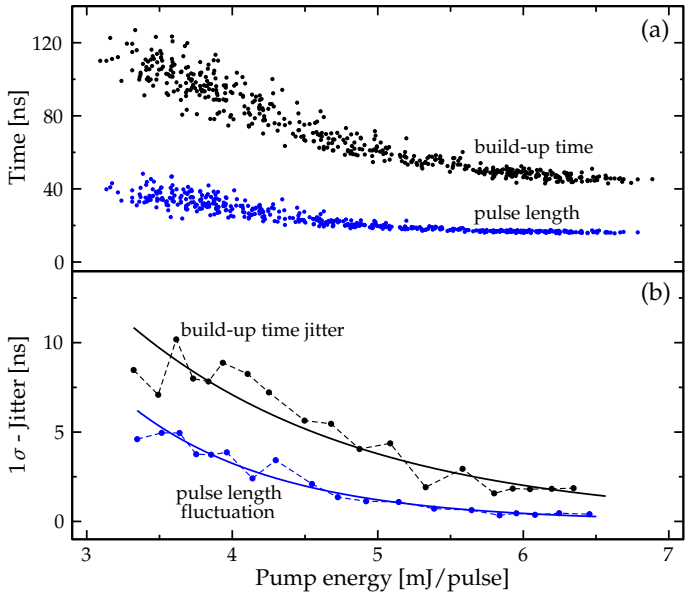

Figure 2.5 – *(color online) (a) Pulse generation dynamics depending on the pump energy. The build-up process becomes faster for higher pump energies. The same holds for the pulse duration, which becomes sorter. (b) Statistical fluctuations given as local standard deviations (from 25 shots per measurement) of the build-up time and the pulse duration decrease with rising pump energy.*

ficiently short to induce exactly one output pulse, while the build-up time is about one order of magnitude larger than the pump pulse duration. The lower part (b) of the figure shows locally calculated standard deviations of the build-up time and the pulse duration taken from 25 pulses each. Apparently the pulse timing jitter of the oscillator is stronger for lower pump energies, i.e. closer to laser threshold.

Since the pulse timing strongly depends on the pump power it is a natural consequence of the power fluctuations of the Nd:YAG pump laser, which exhibit RMS shot-to-shot energy fluctuations of 4.4 %, that the generated pulses show timing jitter. Another source of fluctuations in the generated pulses is noise on the Hänsch-Couillaud (HC) lock.[26] One strategy of avoiding timing jitter is to strongly pump the oscillator in order to reach a saturated regime. Unfortunately, this has disadvantageous effects on the frequency characteristics of the produced pulses, which will be quantified below.

2.3.2 Conversion efficiency

The conversion efficiency of the Ti:sapphire oscillator was investigated in the range 764 – 856 nm, covered by three mirror sets: a long wave set (LW) for 856 – 840 nm and two configurations for middle wave (MW 840 – 806 nm) and short wave (SW 813 – 764 nm). While for the MW and SW sets only the output coupling mirror

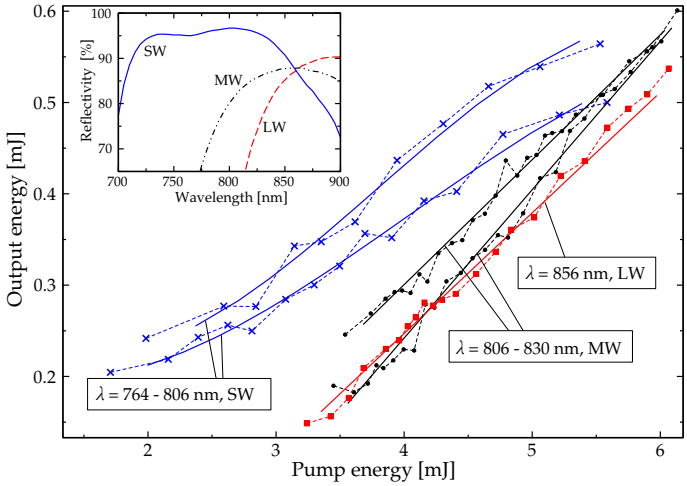

Figure 2.6 – *(color online) Energy conversion in the Ti:sapphire oscillator for different wavelengths using three different mirror sets (SW, MW, LW). The reflectivities of the output coupling mirrors are shown in the inset.*

is different, the LW mirrors form a completely different set. At each wavelength setting the pump energy was varied and about 300 – 500 shots were acquired. The result of these conversion efficiency measurements is shown in Fig. 2.6. For each data set a polynomial regression (3rd order) is performed and depicted as a solid line. The data points shown in the figure are averaged over 25 shots and connected with a dashed line.

The most significant result is, that the SW mirror set provides a superior conversion efficiency over the other two mirror sets. Although uncertainties may arise in the absolute energy calibration, the relative energy calibration for the data pertaining to each curve in Fig. 2.6 is correct. The main difference between the SW and LW/MW mirror sets is the reflectivity of the output coupling mirror. The SW output coupler has a reflectivity of $R = 95\,\%$ and the other two of about 88 %. Correspondingly, the pump energies at which the oscillator reaches laser threshold are smaller for the SW mirrors than for the other sets. The conversion efficiency varies between 5 % and 10 %. As will be investigated later, the cavity lock setting also affects the performance of the cavity. However, at settings where frequency offsets between CW seed light and pulsed output are zero, the "best" conversion is achieved. For now it is noted, that for the conversion efficiency measurements such HC-settings were used.

2.3.3 Frequency evolution

After investigating the intensity dynamics of the pulse generation, we will now focus on frequency shifting effects between the CW seeding light and the pulsed output. In

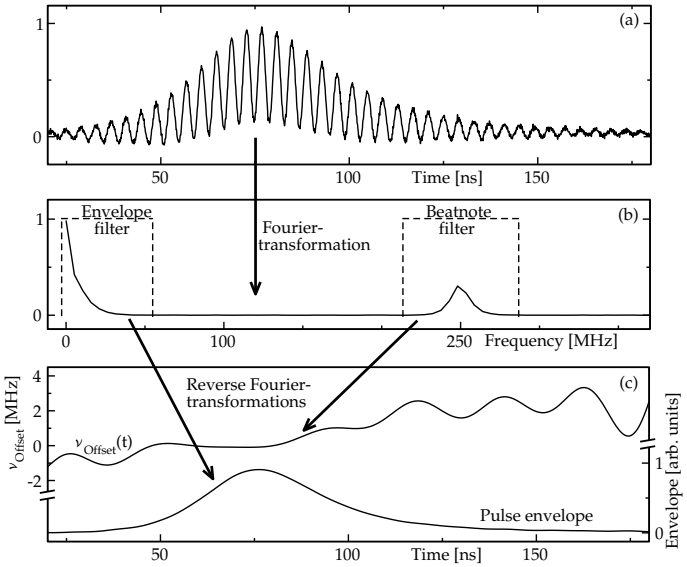

Figure 2.7 – *Overview on the steps of the chirp analysis procedure. (a) The beat pattern between frequency shifted seeding light and the pulsed output of the cavity recorded on a fast photodiode and an fast oscilloscope. (b) The power spectrum showing the two main frequency components from the pulse envelope and from the beatnote. (c) Applying the frequency filters as sketched and reverse Fourier transformation yields the envelope and the instantaneous frequency of the pulse.*

particular for precision spectroscopy this is a crucial issue, because highly accurate wavelength calibration techniques are preferably performed on the CW injection seeding light, while the spectroscopic signal is retrieved from the pulsed output. For instance, Doppler-free saturation spectroscopy for absolute calibration and etalon reference scanning for relative calibration work best with the seeding light. Another method of absolute frequency calibration relies on detecting a beatnote between a femtosecond laser frequency comb and the injection seeding light.[27–29] Therefore it is important to study possible frequency shifts between output pulses and seeding light and to devise methods to measure and control them.

From pulsed dye amplification (PDA) it is known that the produced pulses do not only suffer a net frequency shift but also that their instantaneous frequency changes during the pulse.[16,20] The latter effect is called frequency chirp. To measure instantaneous frequency deviations between pulses and seeding light we used methods based on Fourier analysis which were originally presented by Fee *et al.*[16] and explored for PDA's,[17–20] for alexandrite lasers,[21] for optical parametric oscillators,[22–25] and for pulsed Ti:sapphire lasers.[10–13]

The setup for a quantitative assessment of the instantaneous frequency excursions in the pulsed output is included in Fig. 2.1. Part of the seeding light is first shifted in frequency using an acousto-optical modulator (AOM) and then hetero-

dyned with the pulsed output of the oscillator. The generated beat pattern is detected using a fast photodiode and a fast oscilloscope (Tektronix TDS 7440, 4 GHz, 20 GSample/s). The acquired beat signal traces are transferred from the oscilloscope via GPIB connection to the computer and analyzed. Any beatnote deviations from the AOM frequency ($\nu_{\mathrm{AOM}} = 250\,\mathrm{MHz}$) will be attributed to instantaneous frequency shifts between pulsed output and CW seeding light. The chirp analysis is performed on-line, during all following measurements.

In Fig. 2.7 the process of the Fourier analysis is schematically presented. In the upper part (a) a typical beat pattern is shown. First the signal is Fourier transformed. In the power spectrum — depicted in Fig. 2.7(b) — one recognizes two characteristic peaks. The low frequency part results from the pulse envelope, while the frequencies around 250 MHz arise from the beatnote wiggle. As shown, the two components are well separated in frequency space. After applying simple box shaped spectral filters, the subset of the Fourier transformed data are reversely Fourier transformed, yielding a noise reduced pulse envelope $\varepsilon(t)$ and the phase evolution $\Phi(t)$ of the beatnote wiggle. The time derivative of the phase evolution $\Phi(t)$ gives the instantaneous frequency of the beatnote wiggle, from which the AOM frequency ν_{AOM} is to be subtracted in order to obtain the temporal evolution of the pulsed – CW frequency offset:

$$\nu_{\mathrm{offs}}(t) \;=\; \frac{1}{2\pi}\frac{\mathrm{d}\Phi}{\mathrm{d}t} - \nu_{\mathrm{AOM}}. \tag{2.1}$$

Examples of both the noise reduced envelope $\varepsilon(t)$ and the frequency offset are depicted in Fig 2.7(c). The resulting instantaneous frequency offset can be approximated by a net frequency shift $\bar{\nu}_{\mathrm{offs}}$ and a linear frequency change in time $\tilde{\nu}_{\mathrm{lin}}$, which will be referred to as linear chirp. In the following, focus is on how $\bar{\nu}_{\mathrm{offs}}$ and $\tilde{\nu}_{\mathrm{lin}}$ are affected by the pump energy, the seeding wavelength and the HC-lock settings.

In order to calculate the net frequency offset $\bar{\nu}_{\mathrm{offs}}$ a weighted average on $\nu_{\mathrm{offs}}(t)$ is performed:

$$\bar{\nu}_{\mathrm{offs}} \;=\; \int \nu_{\mathrm{offs}}(t)\,w(t)\,\mathrm{d}t, \quad w(t) = \frac{\varepsilon(t)}{\int \varepsilon(t)\,\mathrm{d}t}, \tag{2.2}$$

where $w(t)$ is the normalized noise-filtered pulse envelope $\varepsilon(t)$. The linear frequency chirp $\tilde{\nu}_{\mathrm{lin}}$ is extracted from the instantaneous frequency evolution $\nu_{\mathrm{offs}}(t)$ by a weighted linear regression using the same weight function $w(t)$. For that a similar method as outlined in Press *et al.*[30] is applied. A linear approximation $\tilde{\nu}_{\mathrm{offs}}(t)$ of the instantaneous pulsed – CW frequency offset $\nu_{\mathrm{offs}}(t)$ is written as:

$$\tilde{\nu}_{\mathrm{offs}}(t) \;=\; \tilde{\nu}_0 + \tilde{\nu}_{\mathrm{lin}}\,t. \tag{2.3}$$

The parameters $\tilde{\nu}_0$ and $\tilde{\nu}_{\mathrm{lin}}$ are extracted using a weighted linear regression which is defined using a χ^2-function:

$$\chi^2(\tilde{\nu}_0, \tilde{\nu}_{\mathrm{lin}}) \;=\; \int \left(\nu_{\mathrm{offs}}(t) - \tilde{\nu}_0 - \tilde{\nu}_{\mathrm{lin}}\,t\right)^2 w(t)\,\mathrm{d}t. \tag{2.4}$$

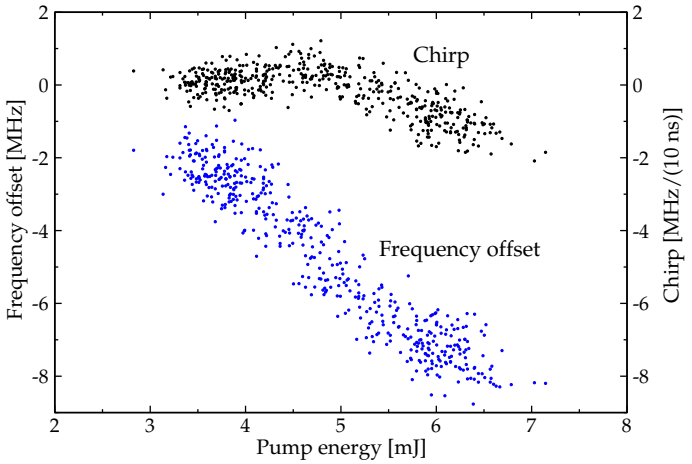

Figure 2.8 – *(color online) Typical behavior of the frequency offset $\bar{\nu}_{offs}$ and the linear chirp $\tilde{\nu}_{lin}$ of the pulsed output of the oscillator at a fixed wavelength $\lambda = 810\,nm$ and fixed HC-setting for varying pump pulse energies. The linear chirp contribution starts around 0 MHz/(10 ns), rises slightly at low energies, and eventually becomes increasingly negative for larger pump energies. At the same time the net pulsed – CW frequency shift $\bar{\nu}_{offs}$ becomes more negative for higher pump energies.*

The optimal regression is achieved when the partial derivatives of χ^2 to the parameters $\tilde{\nu}_0$ and $\tilde{\nu}_{\mathrm{lin}}$ vanish. Using the following definitions:

$$S_t = \int t\, w(t)\,\mathrm{d}t, \quad S_\nu = \int \nu_{\mathrm{offs}}(t)\, w(t)\,\mathrm{d}t, \tag{2.5}$$

$$S_{tt} = \int t^2 w(t)\,\mathrm{d}t, \quad S_{t\nu} = \int t\, \nu_{\mathrm{offs}}(t)\, w(t)\,\mathrm{d}t, \tag{2.6}$$

$$\Delta = S_{tt} - (S_t)^2 \tag{2.7}$$

the regression leads to the following result:

$$\tilde{\nu}_0 = \frac{S_{tt} S_\nu - S_t S_{t\nu}}{\Delta}, \tag{2.8}$$

$$\tilde{\nu}_{\mathrm{lin}} = \frac{S_{t\nu} - S_t S_\nu}{\Delta}. \tag{2.9}$$

It should be noted that in general $\tilde{\nu}_0$ is different from the net frequency shift $\bar{\nu}_{\mathrm{offs}}$.

Experimentally, it is important to know the net frequency shift $\bar{\nu}_{\mathrm{offs}}$ precisely and take it into account for an absolute frequency calibration. For giving an uncertainty value one can use the weighted standard deviation:

$$\sigma_w = \sqrt{\int \left(\left(\bar{\nu}_{\mathrm{offs}} - \nu_{\mathrm{offs}}(t) \right) w(t) \right)^2 \mathrm{d}t} \tag{2.10}$$

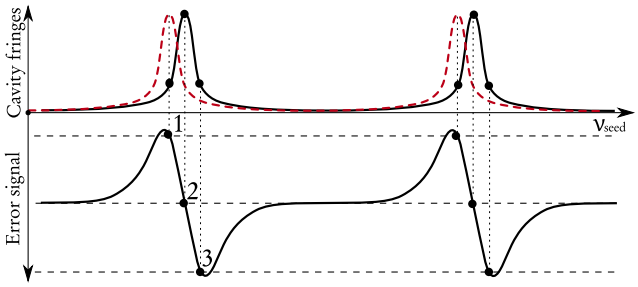

Figure 2.9 – *(color online) The Hänsch-Couillaud locking scheme. The error signal and the cavity fringes versus the seed frequency ν_{seed} are depicted. The thin dashed lines show three different voltage offset settings and the resulting lock point position relative to the cavity mode structure. The second and slightly displaced fringe pattern depicted as a (red) dashed line illustrates the fringe positions right after pumping the cavity.*

Systematic effects can result from non-vanishing linear and higher order chirps, so that the value for the linear chirp can be taken into account as an additional contribution to an estimate of a calibration uncertainty. In Fig. 2.8 the frequency offset $\overline{\nu}_{\text{offs}}$ and the linear frequency chirp $\widetilde{\nu}_{\text{lin}}$ are measured and analyzed via Eqs. (2.1-2.9) as a function of the pump energy at a fixed wavelength of $\lambda = 810\,\text{nm}$. From the figure one can see, that the offset frequency $\overline{\nu}_{\text{offs}}$ decreases with rising pump energies. At low pump energies, the linear chirp rises slightly with increasing pump energies and obtains increasingly negative values for larger pump powers.

2.3.4 Cavity mode pulling

As mentioned before, the oscillator cavity is locked to the seed frequency using the technique devised by Hänsch and Couillaud.[26] In Fig. 2.9 the longitudinal cavity mode structure and the HC error signal are shown as functions of the seed-light frequency. For optimal coupling of the seeding light into the cavity, the electronics has to be set such that the cavity is in perfect resonance with the frequency of the seeding light. This setting is labeled as "2" in Fig. 2.9. Since the build-up time in the pulsed oscillator is about three times longer than the actual pulse duration, the center frequency of the pulsed output will be strongly affected by the cavity mode structure. Such an effect, referred to as "cavity mode pulling", has been observed before in other laser materials.[31,32] Also in a theoretical model by Bowers and Moody[33] it is predicted, that the output of injection-seeded pulsed laser systems, where the cavity round trip time is much shorter than the actual build-up time, the longitudinal mode structure of the cavity rather than the seed frequency determines the center frequency of the output pulses. The seed frequency merely selects the cavity resonance frequency at which the output is pulled to. As a consequence, any deviation of the HC-lock from the ideal setting "2" will lead to frequency offsets between seeding light and pulsed output.

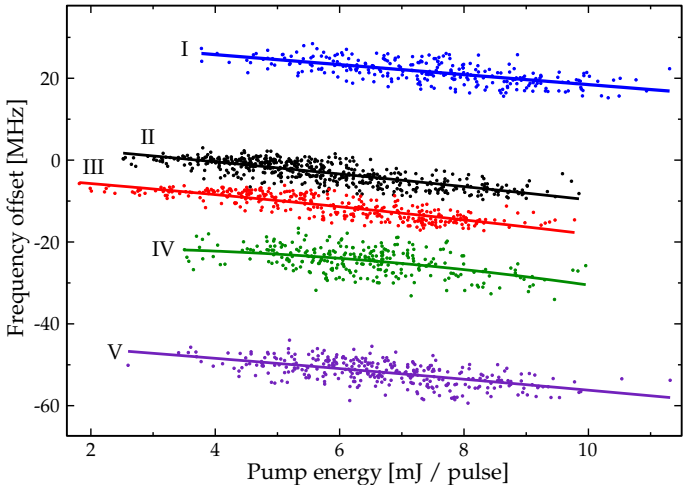

Figure 2.10 – *(color online) Set of measurements of the pulsed – CW frequency offset $\bar{\nu}_{offs}$ at $\lambda = 810\,nm$ and at different HC-settings. With rising pump energies $\bar{\nu}_{offs}$ becomes more negative. Using different HC-settings (numbered from I to V) it is possible to tune the net frequency shift $\bar{\nu}_{offs}$ within a range between −50 MHz and 25 MHz.*

However, this is valid for the non-pumped cavity only. When the pump pulse arrives, the refractive index of the Ti:sapphire crystal[34] and therewith the optical path length of the cavity is changed on a nanosecond time scale, which is instantaneous for the cavity mechanics. As a result of this optically induced refractive index change, the cavity resonances are shifted by a certain amount depending on the pump intensity and of the wavelength of the seeding light. In Fig. 2.9 the shifted cavity resonance pattern is depicted with a (red) dashed line.

In order to investigate the cavity mode pulling mechanism, a series of measurements has been performed at a fixed wavelength $\lambda = 810\,nm$. For different HC-settings, the pulsed – CW frequency offset $\bar{\nu}_{offs}$ is measured as a function of the pump pulse energy. The data in Fig. 2.8 pertain to one particular HC-setting. In order to exclude possible effects from wavelength drifts, a high accuracy wavemeter (ATOS λ-meter) was used to check the long term stability of the seed frequency within 30 MHz throughout the set of measurements in the figure. It is assumed that optical characteristics of the cavity components (the mirrors and the Ti:sapphire crystal) are constant within that frequency interval. However, since the pulsed – CW frequency offset is measured relative to the seed frequency it is not necessary to lock the frequency to an absolute standard.

The results of these measurements are depicted in Fig. 2.10. It shows that the pulsed – CW frequency offset strongly depends on the HC-setting and to a lesser extend on the pump energy. For all tested HC-lock settings the pulsed – CW offset $\bar{\nu}_{offs}$ is increasingly negative for increasing pump energies. An important practical

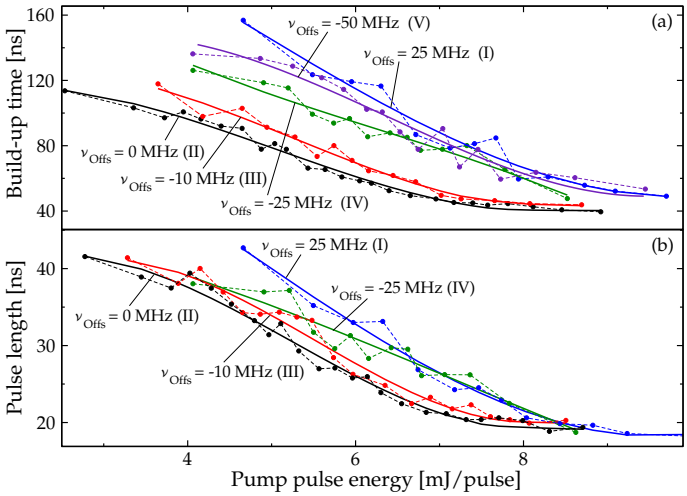

Figure 2.11 – *(color online) Build-up times and pulse durations measured at different HC-lock settings and varying pump energies. Numbering and color coding is consistent with Fig. 2.10. The trace for the pulse durations for a −50 MHz frequency offset setting (V) is not depicted in aid of a better overview — it is located in the vicinity of settings (I) and (IV).*

conclusion from this measurement is that the HC-lock can always be set such that $\bar{\nu}_{\text{offs}}$ is about zero. It should be noted that the range of pulsed – CW frequency offsets being accessible by tuning the HC-lock point is related to the finesse of the oscillator cavity, because that determines the width of the HC-error signal. The fact that $\bar{\nu}_{\text{offs}}$ depends on the pump pulse energy, can be used to derive the refractive index change in the Ti:sapphire crystal as a function of the wavelength and of the pump fluence. This will be discussed below.

Since the HC-setting and the applied pump energy both affect the cavity length, the influence of the HC-lock on the build-up timing, the pulse length, and the linear chirp is further investigated. In Fig. 2.11 the pulse build-up times and pulse durations are plotted for different HC-lock settings and varying pump energies. Indeed the build-up times are shorter for HC-settings, which produce small pulsed – CW frequency offsets and become longer for larger offsets. This can be explained by the influence of the longitudinal mode structure on the amplification gain. When the seeding light is in exact resonance with a specific mode of the pumped cavity, the injection seeded amplification is most efficient as consecutive round trips are perfectly in phase. Slight phase mismatches are disadvantageous for the amplification. This frequency discrimination in the end causes the center frequency of the pulsed amplification being pulled towards the cavity resonance even when it starts with a considerable frequency mismatch between seed and cavity resonance. However such a mode pulling process takes a number of round trips with disadvantageous mutual phase relations. Thus the build-up time is shortest for a zero frequency off-

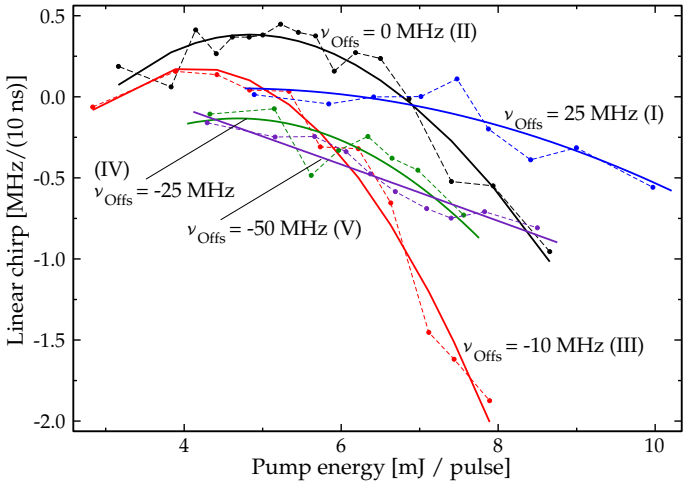

Figure 2.12 – *(color online) Experimental data for the linear frequency chirp $\widetilde{\nu}_{lin}$ derived according to Eq. (2.9) measured at $\lambda = 810$ nm and different HC-settings at varying pump energies. For higher pump energies the linear chirp becomes increasingly negative.*

set setting; this phenomenon could possibly be used in an improved cavity locking scheme.

In Fig. 2.12 the results for the measurements of the linear chirp $\widetilde{\nu}_{\mathrm{lin}}$ are shown. The five traces for the different HC-settings denoted with the corresponding pulsed – CW frequency offset have in common that for higher pump energies the chirp becomes increasingly negative. However, for HC-settings with low pulsed – CW frequency offsets, the linear chirps change more drastically for increasing pump power. A possible explanation is that the pulses are shorter for lower pulsed – CW offsets. Even an equal difference of the instantaneous frequency between pulse head and pulse tail results in a larger linear chirp in shorter pulses.

2.3.5 Wavelength dependence

In the following the influence of the seeding wavelength on both the lasing dynamics and the frequency evolution will be investigated. In the two previous sections the frequency evolution and its dependence on the HC-lock was characterized in detail for one specific wavelength setting ($\lambda = 810$ nm). As was shown, the HC-settings can be used to tune the pulsed – CW offset $\overline{\nu}_{\mathrm{offs}}$ to zero. Moreover, the zero offset point coincides with the setting of shortest build-up time and pulse length at a given seeding wavelength and pump energy. In order to retain control over the measurement procedures, the following studies are restricted to such zero pulsed – CW frequency offset conditions.

In Fig. 2.13 the build-up timing and pulse durations are plotted for different wavelengths and different mirror sets. Conditions of wavelengths and mirror sets

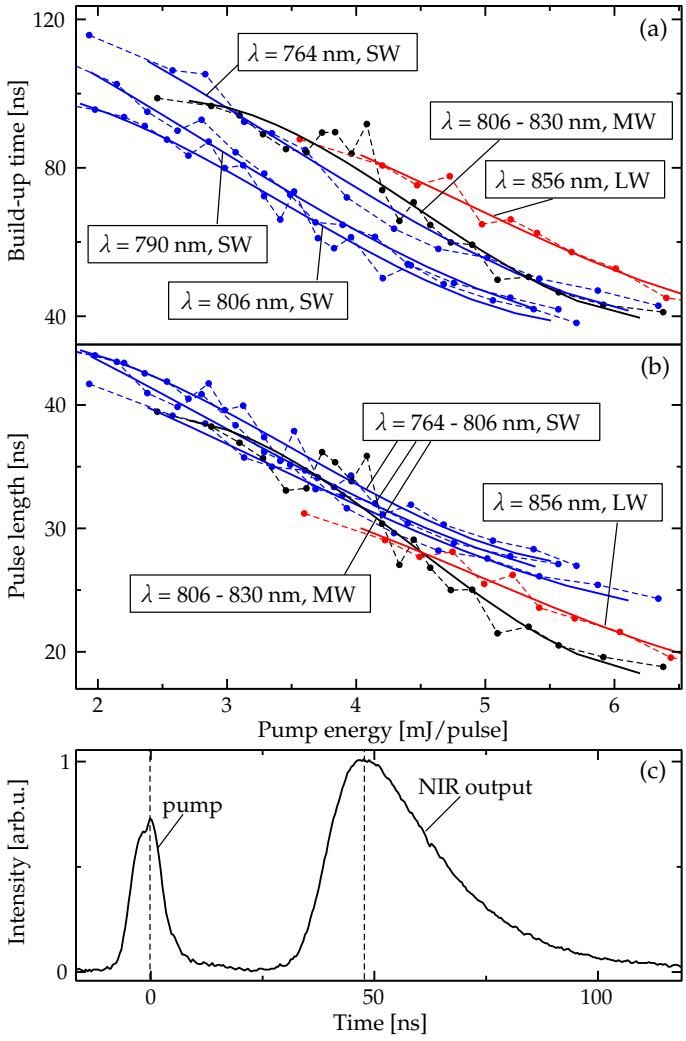

Figure 2.13 – *(color online) Wavelength dependence of the build-up time (a) and pulse duration (b) at zero pulsed – CW frequency offset and varying pump energies. Labels indicate additionally the used mirror set (cf. inset in Fig. 2.6). Part (c) shows a build-up process for the SW mirror pertaining to lower cavity round trip losses than the MW and LW sets (cf. Fig. 2.4).*

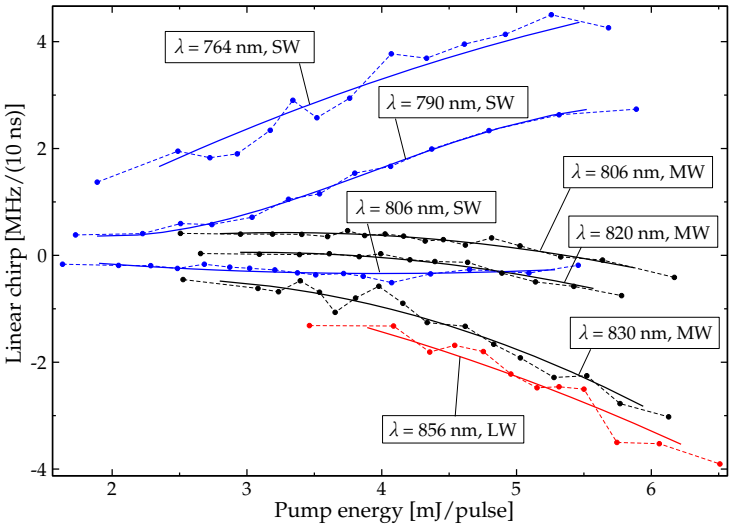

Figure 2.14 – *(color online) Linear chirp $\widetilde{\nu}_{lin}$ measured at different wavelength, zero pulsed – CW frequency offset, and varying pump energy.*

delivering the largest amplification gain per cavity round trip are expected to provide the shortest build-up times. In part (a) of the figure the build-up times for the SW mirror set are the shortest. This is a result of cavity losses with the SW mirrors being a factor of 2 smaller than for the other sets. It is also for this reason, that in comparison to the MW and LW mirrors, the pulses from the SW set are longer in duration. The SW build-up process, depicted in Fig. 2.13(c) yields a skewed time evolution: a steep build-up and a slower pulse depletion. This is in contrast to the time evolution in Fig. 2.4 obtained with the MW mirror set.

Next to the lasing dynamics, an important question is how the linear chirp depends on the wavelength. To investigate this, the linear chirp $\widetilde{\nu}_{\mathrm{lin}}$ was measured as a function of the pump energy at different seed wavelengths, still retaining zero frequency offset conditions. In Fig. 2.14 the measured linear chirp values are shown. In the figure one can clearly see that the linear chirps attain values close to zero for wavelengths in the vicinity of 800 nm. Even for increased pump energies the pulses maintain their low chirp characteristic. For shorter wavelengths the linear chirp becomes increasingly positive and for longer wavelengths increasingly negative. The linear chirp becomes generally stronger for higher pump energies. Below, we will further discuss how the chirp and cavity mode-pulling effects relate to dynamics in population inversion and refractive index.

2.3.6 Amplifier effects

For the investigation on how the pulse characteristics are affected by the external amplification, systematic measurements are performed on the pulse duration, the pulse

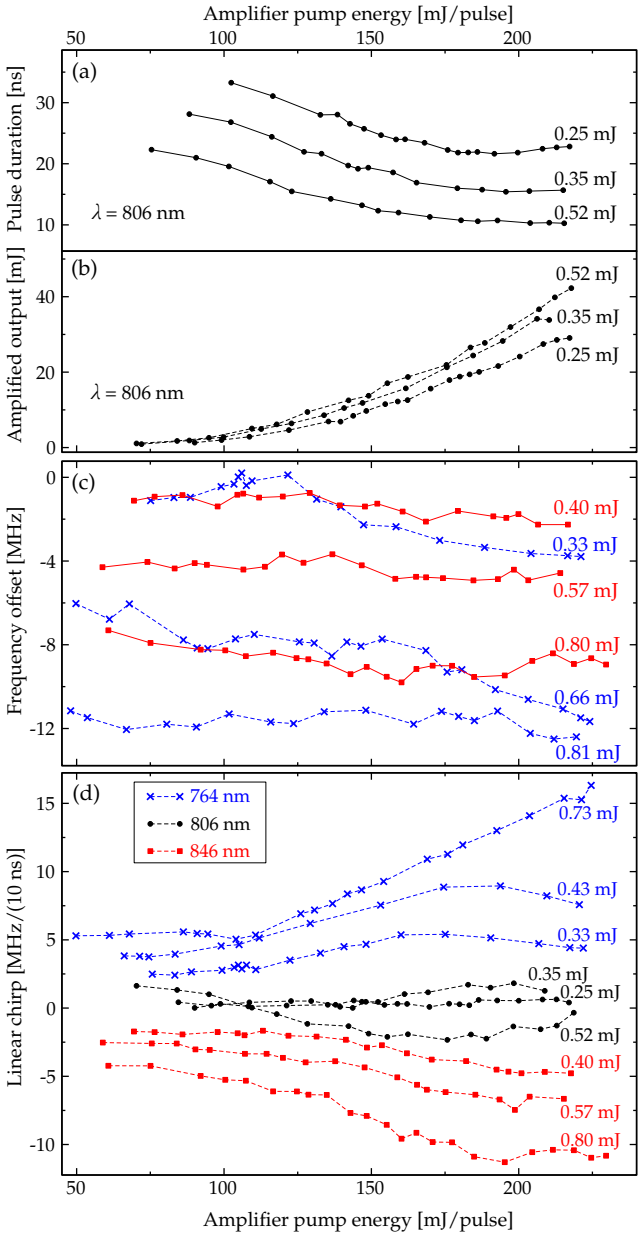

Figure 2.15 – *(color online) Effect of the external amplification on several characteristics of the pulsed output of the oscillator: (a) pulse duration, (b) pulse energy, (c) pulsed – CW frequency offset* $\overline{\nu}_{off}$*, and the (d) linear chirp* $\widetilde{\nu}_{lin}$*. The pulse energies indicated as data labels represent the values before amplification.*

energy, the mean pulsed – CW frequency offset $\overline{\nu}_{\text{offs}}$, and the linear chirp $\widetilde{\nu}_{\text{lin}}$. Three different seeding wavelengths were chosen at which all of the listed characteristics are measured: one wavelength (806 nm) close to the top of the Ti:sapphire gain profile, and two wavelengths at the long wavelength (846 nm) and the short wavelength (764 nm) side of the range of operation of the laser. For all measurements, the external amplification comprises of 8 passes through the Ti:sapphire crystal. For each wavelength setting a series of measurements was performed: at a number of fixed oscillator pump settings the pulse characteristics were recorded as a function of the amplifier pump energy. The results of these series are depicted in Fig. 2.15.

For the pulse duration and pulse output energies the obtained results are rather similar and do not depend on the wavelengths. Therefore in Fig. 2.15(a) and 2.15(b) only results for $\lambda = 806\,\text{nm}$ are represented. For three different oscillator pulsed output energy levels the pulse duration and the pulse energies for the amplified output are shown. The output energy increases with the pump energy applied to the Ti:sapphire crystal and with the oscillator output energy. A maximum of 41 mJ amplified output is achieved, corresponding to a conversion efficiency of 18 %. Apparently, the pulse duration is shortened for strong external amplification. For instance, at the particular setting at which the oscillator produces 0.25 mJ in a pulse duration of about 35 ns the amplified output is shortened to 22 ns at maximum amplification. Also for the other wavelengths maximum pulsed output energies of 35 – 40 mJ are reached.

In Fig. 2.15(c) the results for the measurements of the mean pulsed – CW frequency offset $\overline{\nu}_{\text{offs}}$ of the amplified output are shown. Here, the results for wavelengths 764 nm and 846 nm are displayed. The results at $\lambda = 806\,\text{nm}$ are similar to these. Apparently, the amplification changes $\overline{\nu}_{\text{offs}}$ by maximally 5 MHz at wavelength 764 nm for the medium cavity pump setting at which the oscillator output was 0.66 mJ. In spectroscopic applications it is possible, if desired, to compensate for such frequency offsets using the HC-lock settings at the oscillator cavity.

Measurements of the linear chirp $\widetilde{\nu}_{\text{lin}}$ at wavelengths 764 nm, 806 nm, and 846 nm are depicted in Fig. 2.15(d). The result shows that the linear chirp becomes more pronounced by the amplifier. For the short wavelength 764 nm the linear chirp is positive and increases for higher oscillator output energies and increasing amplifier pump energies, while at the long wavelength 846 nm the chirp is negative and becomes more negative under conditions of more intense pumping. At wavelength 806 nm the linear chirp remains in the vicinity of zero during external amplification.

2.3.7 Laser bandwidth

For application in laser spectroscopic experiments the spectral bandwidth of a laser source is a crucial parameter. Here the bandwidth is derived from measurement of a spectral lineshape under conditions at which the profile is fully determined by the laser bandwidth properties. The Q(1) line in the EF – X (0,0) band in the D_2 molecule is probed via $2 + 1$ resonance-enhanced multi-photon ionization using a wavelength near $\lambda = 202\,\text{nm}$. The spectrum is displayed in Fig. 2.16

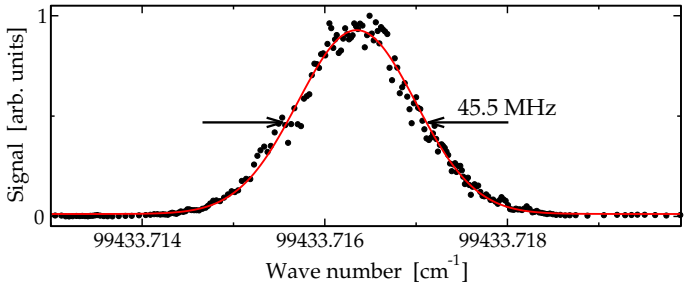

Figure 2.16 – *(color online) The Q(1) line of the EF ← X (0,0) band in D_2 measured in a 2 + 1 REMPI process with the FWHM of 45.5 MHz indicated.*

The measurement conditions entail: (i) two-photon excitation with counter-propagating beams, thus imposing Doppler-free circumstances; (ii) collision-free conditions of a molecular beam, therewith avoiding collisional broadening (iii) excitation with low laser intensity to ensure that the AC Stark effect broadening is below 1 MHz; (iv) an excited state lifetime of about 200 ns[35] causing lifetime broadening below 1 MHz. Under these conditions the spectral line profile represented by a Gaussian with a width of $\Delta\nu = 45.5$ MHz is entirely determined by the spectral bandwidth properties of the laser at its fourth harmonic. Taking into account the two-photon excitation and fourth harmonic generation, as well as a Gaussian profile, the spectral output of the Ti:sapphire laser can be derived at $\Delta\nu_{IR} = 16$ MHz.

During the spectroscopy on the D_2 line the following laser settings were used: In order to generate chirp reduced pulses at reasonably stable lasing conditions, regarding timing jitter and output energy fluctuations, the oscillator pump was adjusted such that the pulse build-up time in the oscillator was consistently maintained at 80 ns. The amplifier output was adjusted to 8 mJ. Using the MW mirror set the oscillator produced pulses of 0.3 mJ energy and 30 ns duration. The amplifier shortened the pulses to about 25(3) ns which corresponds to a Fourier-transform limited spectral width 17.5(2.5) MHz for ideally Gaussian shaped pulses which is in reasonable agreement with the estimated value of 16 MHz derived from the spectral measurement shown in Fig 2.16.

2.4 Optically induced refractive index change in Ti:sapphire

The results in Fig. 2.8 and Fig. 2.10 show, that the pulsed – CW frequency offset $\bar{\nu}_{offs}$ varies with the applied pump energy. The reason for this behavior is an optically induced refractive index change Δn in the Ti:sapphire crystal, which depends on the applied pump energy and affects the longitudinal mode structure of the cavity. Since the build-up time is much longer than the round-trip time of the cavity, and the amplification from the seed light intensity level to the maximum pulsed intensity exceeds 4 orders of magnitude, the pulsed output frequency ν_{out} will be completely

pulled from the seed frequency ν_{cw} to the closest pumped cavity resonance position ν_p. This phenomenon has previously been observed in other laser materials[31,32] and is explained in a numerical model.[33] In the following, a relation between the refractive index change Δn and the pulsed – CW frequency offset $\bar{\nu}_{off} = \nu_p - \nu_{cw}$ as functions of the pump fluence is derived and measurements for different wavelengths are discussed.

Since the pump fluence is provided in a two-sided pumping scheme, and the Ti:sapphire crystal is designed such that it absorbs 90 % of the incident pump light, the resulting locally varying fluence is approximated by an averaged fluence $F_p = 0.9/\ln 10 \cdot E_p/A \approx 0.39\, E_p/A$ within the cavity mode volume in the crystal (E_p: pump energy, $A = 4/\pi d^2$: cavity mode area, d: FWHM diameter 0.38 mm). The key to the refractive index change dn/dF_p is to measure the slope $d\bar{\nu}_{offs}/dE_p$ of the pulsed – CW frequency offset as a function of the pump energy. The relation between the two is given by:

$$\frac{dn}{dF_p} = \frac{dn}{d\bar{\nu}_{offs}} \frac{A}{0.39} \frac{d\bar{\nu}_{offs}}{dE_p}. \tag{2.11}$$

Since the pulsed output frequency ν_{out} is in resonance with the cavity, it is a multiple of the longitudinal mode spacing ν_{FSR}:

$$\frac{\nu_{out}}{m} = \nu_{FSR} = \frac{c}{n\,l + L} \tag{2.12}$$

where m is the mode number of the pulsed output frequency ν_{out}, n the refractive index of the Ti:sapphire crystal, l the crystal length, and $n\,l + L$ the optical path length of the cavity. Inserting $\bar{\nu}_{offs} = \nu_{out} - \nu_{seed}$ and rearranging Eq. (2.12) delivers:

$$(\bar{\nu}_{offs} + \nu_{seed})\,(n\,l + L) = c\,m \tag{2.13}$$

$$\Longrightarrow\ d\bar{\nu}_{off}\,(n\,l + L) + (\bar{\nu}_{off} + \nu_{seed})\,l\,dn = 0 \tag{2.14}$$

The differentiation of Eq. 2.13 yields:

$$\Longrightarrow\ \frac{dn}{d\bar{\nu}_{offs}} = -\frac{1}{l}\,\frac{n\,l + L}{\bar{\nu}_{offs} + \nu_{seed}} = -\frac{\lambda}{l\,\nu_{FSR}}. \tag{2.15}$$

Inserting this result into Eq. (2.11) yields:

$$\frac{dn}{dF_p} = -\frac{A\,\lambda}{0.39\,l\,\nu_{FSR}}\,\frac{d\bar{\nu}_{offs}}{dE_p}, \tag{2.16}$$

where λ is the seeding wavelength.

In a series of measurements at different seeding wavelengths λ between 764 nm and 856 nm the pulsed – CW frequency offset $\bar{\nu}_{offs}(E_p)$ was measured as a function of the applied pump pulse energy E_p. In order to maintain comparable HC-lock conditions, the pulsed – CW frequency offset was first adjusted to zero for low pump

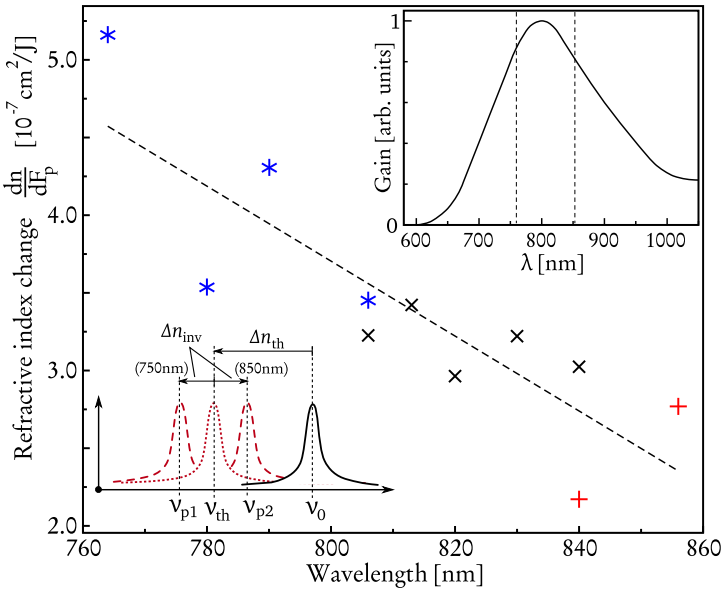

Figure 2.17 – *(color online) Optically induced change of the refractive index of the Ti:sapphire crystal in the pulsed oscillator as a function of the seeding wavelength. Pump fluences have been varied between 1.5 – 7 J/cm² for each wavelength. A graphical representation of the laser gain curve of Ti:sapphire is shown as a small inlay. The symbols for the data points indicate the used mirror set ('star' for SW, 'X' for MW, '+' for LW, cf. Fig. 2.6).*

fluences before the variation of the pump energy was carried out (*cf.* result for frequency offset in Fig. 2.8 at $\lambda = 810\,\mathrm{nm}$). From the acquired data, the slope $d\bar{\nu}_{\mathrm{offs}}/dE_{\mathrm{p}}$ is obtained using linear regression at each seeding wavelength setting. The values are inserted into Eq. 2.16 to calculate the refractive index change dn/dF_{p} at each seeding wavelength setting. The results depicted in Fig. 2.17 show an approximately linear wavelength dependence. The refractive index change has a positive sign and is stronger for the short wavelength side of the investigated range.

It has to be pointed out, that the relation given in Eq. 2.16 is based on the assumption that the refractive index does not change during the pulse amplification and that the cavity-mode pulling is complete in the sense that the output frequency is identical with the cavity resonance. However, as Wall *et al.*[34] noted, the optically induced refractive index change $\Delta n = \Delta n_{\mathrm{th}} + \Delta n_{\mathrm{inv}}$ consists of two contributions, which relax on different timescales. The thermal contribution Δn_{th} relaxes within several milliseconds, while the contribution Δn_{inv} related to the population inversion relaxes synchronically with the decay of the excited state of the Ti:sapphire crystal. For the cavity mode pulling, the relaxation of the thermal contribution Δn_{th} can be neglected, because it is much slower than the build-up time. The relaxation of the contribution from the population inversion, however, affects the values obtained in Fig. 2.17.

In the lower left inset of Fig. 2.17 different positions of the cavity resonance fringes are depicted. Considering the resonance of the non-pumped cavity at ν_0 a positive refractive index change shifts this resonance to a somewhat lower frequency ν_p. The indicated resonance fringes in the inset represent the positions: ν_{th} for a purely thermal and positive refractive index change $\Delta n = \Delta n_{th} > 0$, ν_{p1} for an additional positive contribution Δn_{inv} from the population inversion, and ν_{p2} for a negative contribution Δn_{inv}.

For the process of the pulse amplification this has the following consequences: During the first phase of the amplification from the pump arrival to the head of the pulse the intra cavity mode intensity is amplified by several orders of magnitude without having substantially broken down the population inversion. Hence, the instantaneous frequency of the leading part of the pulse is completely pulled to the modified cavity resonance corresponding to the full optically induced refractive index change $\Delta n = \Delta n_{th} + \Delta n_{inv}$. Subsequently the population inversion relaxes during the main part of the pulse evolution, which shifts the cavity resonance dynamically and changes the mode pulling conditions. For a negative Δn_{inv} a relaxation towards increasing refractive index is expected. That would decrease the cavity mode spacing and hence decrease the cavity resonance frequency. Consequently, dynamic mode-pulling should cause negative frequency chirp on the pulsed output, and vice versa for positive Δn_{inv} positive frequency chirp is expected.

When comparing these findings with the results in section 2.3.5, the refractive index relaxation provides an explanation for the behaviour of the linear chirp $\tilde{\nu}_{lin}$ at different wavelengths (*cf.* Fig 2.14): The positive linear chirp $\tilde{\nu}_{lin}$ found for wavelengths $\lambda < 800\,\text{nm}$ points to a positive contribution Δn_{inv} while the negative chirp for $\lambda > 800\,\text{nm}$ would correspond to a negative Δn_{inv}. In the vicinity of $\lambda = 800\,\text{nm}$ however the chirp is approximately zero, because Δn_{inv} is zero and does not change during the excited state relaxation. This qualitative result for Δn_{inv} matches with the measurements on the refractive index change in Fig. 2.17: Assuming that dn_{th}/dF_p is not wavelength dependent within the investigated range, the values for $dn_{inv}/dF_p(\lambda)$ given in Fig. 2.17 can be approximated:

$$\frac{dn_{inv}}{dF_p} = \tilde{n}(\lambda - \lambda_0) - \frac{dn_{th}}{dF_p}, \tag{2.17}$$

where dn_{th}/dF_p is obtained at wavelength $\lambda_0 \approx 800\,\text{nm}$ — the linear chirp is minimal at that wavelength — and $\tilde{n}$ a dispersion coefficient.

It should be noted that the behavior of the refractive index of the pumped Ti:sapphire crystal can best be compared with anomalous-dispersion around an absorption feature. The difference is that the amplification in pumped Ti:sapphire can be considered as negative absorption which results in an inverted anomalous-dispersion relation. This effect has been confirmed earlier in ruby by Bean *et al.*[36] and can be derived from the complex index of refraction using Kramers-Kronig relations in which the real and imaginary parts of the index are integrally related to each other.[37] In this context, the wavelength range at which the refractive index is investigated, is

Table 2.1 – *Optically induced refractive index changes in Ti:sapphire. Δn_{th}: thermal contribution, $\tilde{n}$: dispersion coefficient (see Eq. 2.17, $\lambda_0 = 800\,nm$). Both values have an error budget of a factor of two resulting from calibration errors on the optical fluence. Additionally, the given observed dispersion coefficient $\tilde{n}$ can be systematically lessened by another factor ranging between 1 and 2. Doping characteristics of the crystal are given as well: α_{532}: linear absorption coefficient at $\lambda = 532\,nm$, $N_{Ti_2O_3}$: titanate number density, C_π: constant defined in Eq. 2.18.*

Δn_{th}	$3.6 \cdot 10^{-7}$	$\mathrm{cm^2/J}$
$\tilde{n}$	$-2.5 \cdot 10^{-9}$	$\mathrm{cm^2/(J\,nm)}$
α_{532}	1.47	$\mathrm{cm^{-1}}$
$N_{\mathrm{Ti_2O_3}}$	$1.60 \cdot 10^{19}$	$\mathrm{cm^{-3}}$
C_π (this work)	$2.3 \cdot 10^{-25}$	$\mathrm{cm^3}$
C_π (Wall *et al.*[34])	$(1.1 \pm 0.5) \cdot 10^{-24}$	$\mathrm{cm^3}$

in the center of a broad gain profile (cf. Fig. 2.17) and the observed refractive index change is the central linear part of the dispersion curve. In travelling pulse dye amplifiers dispersively depending chirp characteristics have been observed as well. Melikechi *et al.*[18] described the phenomenon in detail and presented a theoretical model. Since the fluorescence lifetimes in dyes are typically smaller then 1 ns, the refractive index of the amplifying medium is instantaneously modulated with the pump pulse intensity. This results in frequency chirp in the output pulses, which changes its sign around the maximum of the gain curve of the laser active medium.

The values obtained in Fig. 2.17 can be expressed as:

$$\frac{dn}{dF_{\mathrm{p}}} = C\,\frac{N_{\mathrm{ex}}}{F_{\mathrm{p}}}. \tag{2.18}$$

The refractive index change is proportional the number density N_{ex} of Ti atoms in the exited state. The constant C is polarization dependent. According to the nomenclature of Moulton[4] and Wall *et al.*[34] the π-polarization is used here. The number density N_{ex} of excited Ti atoms is identified with the ratio of the number of absorbed photons $\mathcal{N}_{\mathrm{abs}} = 0.9\mathcal{N}_{\mathrm{p}}$ to the mode volume $V = A\,l$ in the crystal:

$$N_{\mathrm{ex}} = \frac{\mathcal{N}_{\mathrm{abs}}}{A\,l} = \frac{0.9F_{\mathrm{p}}\lambda}{hcl}, \tag{2.19}$$

h: Plancks constant, c: speed-of-light. Inserting this into Eq. 2.18 yields:

$$C = \frac{hcl}{0.9\lambda}\,\frac{dn}{dF_{\mathrm{p}}} \tag{2.20}$$

The obtained C_π-value for wavelength $\lambda = 800\,\mathrm{nm}$ is listed in Table 2.1 and about a factor of 5 smaller than the value Wall *et al.*[34] had measured at $\lambda = 632.8\,\mathrm{nm}$ even though the Ti-doping and linear absorption α are comparable — $1.47\,\mathrm{cm^{-1}}$ here and $1.27\,\mathrm{cm^{-1}}$ in Wall *et al.* The method used in Wall *et al.* is a direct interferometric approach using a Mach-Zehnder interferometer. The major uncertainty in that

measurement results from assessing the beam size using a "burned spot" technique. Additionally, light at wavelength 632.8 nm is affected by the anomalous-dispersion caused by the absorption band of Ti:sapphire. If, on the other hand, the refractive index change would be as strong at 800 nm as stated in Wall *et al.*, the cavity-mode-pulling should cause pulsed – CW frequency offsets of several 100 MHz which is not experimentally observed. Here the spotsize of the pump beam is measured with a commercial beam profiling system based on a CCD and adjusted such that the full pump intensity profile fits well in the mode volume of the cavity. For the fluence calculation the cavity mode area is used in preference to the slightly smaller pump profile, because the pulse amplification takes a number of cavity round trips and averages over the full cavity mode volume. A total error budget in the determination of the pump fluence F_p of a factor of two is assessed. An additional error in the investigation of the dispersive value $\tilde{n}$ arises from a simplification in the derivation of Eq. (2.16) which neglects the relaxation of the population inversion related refractive index change Δn_{inv}. The frequency chirp caused by it will give a net pulsed – CW frequency shift slightly shifted from the cavity resonance frequency corresponding to the full optically induced refractive index change. This effect systematically yields smaller absolute values for Δn_{inv}. Depending on how efficient the cavity-mode pulling during the main part of the pulse is, the obtained values Δn_{inv} can be up to a factor of two smaller than they actually are.

In the external amplifier, optically induced refractive index changes also affect the frequency evolution of the output pulses (*cf.* Fig. 2.15). While the effect of the thermal contribution to the refractive index change should be negligible, the relaxation of the population inversion modulates the refractive index of the crystal and distorts the instantaneous frequency evolution of the amplified pulse. This phenomenon is additionally complicated by the fact that the pulse length is longer than a single amplification pass. A full numerical analysis is needed to simulate all amplification effects, which was not done within this framework.

We note that optically induced refractive index changes are a major source of the frequency excursions in the output pulses of the oscillator-amplifier system. A detailed investigation of the pulsed – CW frequency offset in turn allowed for a quantification of the optically induced refractive index changes the crystal exhibits.

2.5 Spectroscopic applications of the Ti:sapphire source in the deep ultraviolet

The combination of the pulsed mode of operation providing high peak intensities with the Fourier-transform limited spectral properties, this Ti:sapphire laser system is suitable for nonlinear frequency upconversion and high precision spectroscopies in the deep UV. Various spectroscopic investigations have been performed employing, in particular the fourth harmonic at about 200 nm of the output pulses. In one-photon laser-induced-fluorescence (LIF) atomic beam studies the transition frequency of the singlet $3s \rightarrow 4p$ resonance in Mg at $\lambda = 202\,\mathrm{nm}$ was investigated yield-

ing a transition frequency at an accuracy of ≈ 1 MHz.[28] Also the $3s \rightarrow 3p$ resonance in Mg at $\lambda = 285$ nm was calibrated to the MHz-level of accuracy using the third harmonic ultraviolet output.[29] Several two-photon excitation frequency metrologies were performed as well: on the EF $\leftarrow$ X transition in molecular hydrogen and some of its isotopomers,[27] and on the $4p^6 \rightarrow 4p5p[1/2]_0$ transition in krypton, both yielding accuracies at the MHz-level. In addition this krypton transition was employed in a resonance enhanced sum-frequency mixing scheme, for efficient upconversion of the narrowband output at $\lambda = 212$ nm to the, the XUV-range near 90 nm; at these wavelengths high-resolution spectroscopy was performed on narrow resonances in the H_2 and N_2 molecules.[38]

Furthermore, the laser system was employed in a demonstration experiment where cavity ring-down spectroscopy (CRDS) at the shortest wavelengths so far — down to 197 nm — was performed.[39] Using the CRDS setup, lower vibrational bands of the Schumann-Runge system in molecular oxygen and isotopomeres were measured, and more accurate values of molecular constants were derived.[40] Spectral lines in the lowest (0,0) Schuman-Runge band of molecular oxygen were investigated in more detail (also near $\lambda = 202$ nm), both by laser-induced fluorescence and cavity ring-down methods.[41] The ultra-narrow bandwidth in the deep-UV region allowed for a determination of the pressure shift as well as of the predissociation rate of single resolved fine-structure states in the $B\,^3\Sigma_u^-$, $v = 0$ state of the molecule. These studies amply demonstrate the versatility of the Ti:sapphire laser system for high resolution spectroscopic applications.

In the resonance enhanced sum-frequency mixing experiment a CW laser diode operating at wavelengths about 850 nm was implemented,[38] showing that a system of diode lasers, covering the wavelength range of Ti:sapphire lasers can be used alternatively as seed light source.

2.6 Conclusion

The perspective of the present investigation and analysis of the characteristics of the laser system is aimed at precision calibration application in high resolution spectroscopy, rather than obtaining a full physical understanding of the processes occurring in the laser. Next to the lasing dynamics which include the pulse build-up time, pulse duration and conversion efficiency, special emphasis was put on the frequency evolution of the generated pulses, because that usually is the limiting factor in the determination of the transition frequency of a spectral feature.

We note that, although the quantitative chirp phenomena are similar in effect, the underlying physical mechanisms in the Ti:sapphire oscillator are different from traveling wave optical systems as the external Ti:sapphire amplifier or pulsed dye amplifiers (PDA). The performed measurements revealed the influence of the mode-structure of the oscillator cavity on the pulses ("cavity mode-pulling"), most notably on the net pulsed – CW frequency offset. Such influences are absent in traveling wave amplifiers. However, although the presented external amplification system

and PDAs are both traveling wave systems, their mode of action is different, because the excited state lifetime in Ti:sapphire ($\tau_{\text{Ti:sapphire}} = 3.15\,\mu\text{s}$) is about three orders of magnitude longer than in PDAs ($\tau_{\text{dye}} < 1\,\text{ns}$). In both laser active media, optically induced refractive index changes cause chirp effects on the pulsed output. In PDAs the laser gain and the refractive index are modulated quasi simultaneously with the pump intensity, while in Ti:sapphire multi-pass amplifiers, the relaxation of the population inversion during to the amplification process is the dominating reason for refractive index modulations.

The presented chirp analysis is a single-shot technique the made it possible to monitor frequency differences between seed light and pulsed output at realtime. The cavity mode pulling can be "tuned" using the Hänsch-Couillaud lock yielding zero pulsed – CW frequency offsets. The chirp effects depending on the seed wavelength and the pump intensity are less controllable: working with low pump intensities is the most efficient, but not always available option to minimize the chirp.

The wide wavelength range of Ti:sapphire, the narrow band pulsed characteristics, accurate frequency control and referencing techniques make this laser a flexible instrument for high precision metrology in the deep ultraviolet.

Acknowledgment

The Netherlands Foundation for Fundamental Research on Matter (FOM) is gratefully acknowledged for financial support.

Chapter 3

Reducing first order Doppler shifts in a Sagnac interferometer

We demonstrate a technique to reduce first order Doppler shifts in crossed atomic/molecular and laser beam setups by aligning two counter-propagating laser beams as part of a Sagnac interferometer. Interference fringes on the exit port of the interferometer reveal minute deviations from perfect anti-parallelism. Residual Doppler shifts of this method scale with the ratio $v/(4d)$ of the typical atomic/molecular velocity v and the laser beam diameter d. The method is implemented for precision frequency calibration studies at deep-UV wavelengths, both in one and two-photon excitation schemes: the $6s^2 \rightarrow 6s\,30p_{3/2}\,J=1$ line in Yb at 199 nm and the $4p^6 \rightarrow 4p^5\,5p[1/2]_0$ transition in Kr at $\lambda = 212$ nm. The achieved precision of 6×10^{-10} is limited by the characteristics of the laser system.

This chapter is accepted for publication in Optics Letters.

3.1 Introduction

The Doppler effect, giving rise to line broadening and shifting is an inherent obstacle in precision spectroscopy. In the past a number of Doppler-free techniques were developed to reduce or eliminate those influences.[42] Doppler-free saturated absorption spectroscopy[43] has become a standard method for absolute calibration of continuous wave (CW) frequencies to sub-MHz precision. Doppler-free polarization spectroscopy,[44] where a circularly polarized pump beam causes birefringence in a gaseous medium, tilting the polarization of a counter-propagating linearly polarized probe beam, can be considered a variant of the same concept. Other techniques are based on multi-photon excitation, most prominently, Doppler-free two-photon spectroscopy.[45]

Atomic and molecular beams are a widespread means to reduce Doppler-broadening. Here it is essential to align the laser excitation beam under perfect perpendicular angle in order to reduce Doppler shifts in the spectroscopy. A method to solve this problem is to use a pair of counter-propagating laser beams, and optimize their

overlap such that both beams are subject to identical Doppler-shifts with opposite signs. Moreover, when applying Doppler-free techniques, e.g. Doppler-free two-photon spectroscopy, saturable absorption or polarization spectroscopy, on atomic or molecular samples with anisotropic velocity distribution (such as in beams), the Doppler-free signal can be Doppler-shifted within the bandwidth of the excitation light, when the beams are not perfectly anti-parallel. Under such conditions, the attainable precision is restricted by the accuracy of the alignment procedure.

In the following, we demonstrate a method to reduce experimental uncertainties related to the first order Doppler shift in atomic and molecular spectroscopy based on a Sagnac interferometer. Originally designed for rotation sensing,[46,47] Sagnac interferometers were since then employed in a wide variety of laser-based applications: a.o. for cleaning chirped-pulse amplified pulses from fluorescence background,[48] for generation entangled photon pairs,[49] for frequency stabilization of lasers,[50] and for measuring length and dispersion of optical fibers.[51] Furthermore they are considered for the detection of gravitational waves.[52–54] Here, a Sagnac interferometer is used to align two counter-propagating beams to high precision. We demonstrate the technique for single-photon and Doppler-free two-photon excitation. Doppler uncertainties were reduced to the 10^{-10} accuracy level and can be reduced considerably further.

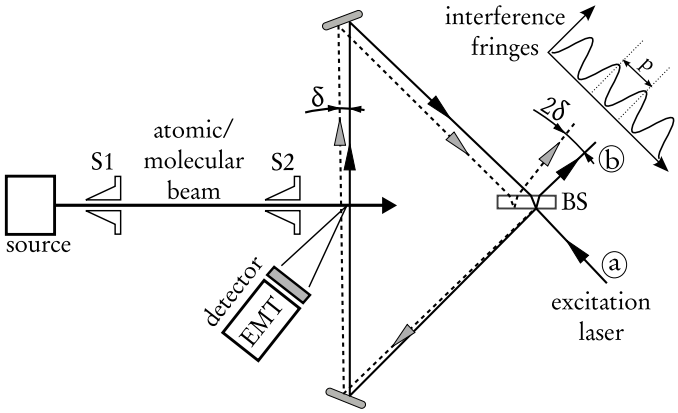

Figure 3.1 – *Generic atomic/molecular beam setup combined with a Sagnac interferometer. A skimmed beam crosses two counter-propagating laser beams in the interaction zone. The incident light coming from port (a) follows the solid line in either direction when the ring is perfectly aligned. If one mirror is tilted by $\delta/2$ — here the beam splitter — the clockwise and counter-clockwise beams generate a fringe pattern as depicted at port (b).*

3.2 Working principle

A generic atomic or molecular beam experimental apparatus with the interaction zone placed in a Sagnac interferometer is depicted in Fig. 3.1. When the interferometer is aligned, one observes two-beam interference as depicted in the figure — parallel fringes with a periodic distance p and a certain inclination depending on the size and the orientation of the angle δ between the two branches in the ring interferometer. An important advantage of such a ring interferometer is its stability with respect to acoustic perturbations: since the two interfering beams follow identical paths, just in opposite directions, the identical effects cancel out. Moreover, even if the coherence length of the laser light is short compared to the ring perimeter, fringes are still observable.

In a two beam interference fringe pattern, the fringe period $p = \lambda/\sin\theta$ is determined by the angle θ between the two beams, and the wavelength λ. In Fig. 3.1 it is illustrated how θ is related to the angular mismatch δ of the counter-propagating beams inside the interferometer: The identical counter-propagating beam paths in a perfectly aligned interferometer are depicted as a solid line. The dashed line shows the beam which is reflected by a beam splitter tilted by an angle $\delta/2$. The transmitted beam, however, is only transversally shifted and follows the same direction as the beam of the perfectly aligned Sagnac interferometer. Hence, the angle between the transmitted and the reflected beam within the ring is δ. When the reflected beam leaves the interferometer after being reflected by the beam splitter it picks up another angular shift by δ so that an angle $\theta = 2\delta$ defines the fringe period on the screen. The same result holds for any mirror tilted by $\delta/2$ within the ring interferometer.

Consequently, the fringe periodic distance p increases for smaller δ. In practice the interferometer is aligned until dark fringe is achieved at port (b) and a bright fringe at port (a). This is due to the beam splitting interface at which the transmitted beam suffers no phase shift at all. The reflected beam, on the other hand, obtains a phase shift π at the first reflection at the beam splitter, but it does not when it is reflected the second time towards port (b), because then it is a reflection within a higher index medium (splitter substrate) at an interface to a lower refractive one (air). Achieving the "dark fringe" condition means, that p is larger than the beam diameter d. Accordingly, a large laser beam diameter helps for a precise alignment. If under experimental conditions the dark fringe alignment does not drift further than to the appearance of the first order bright fringe, it is valid to state:

$$2\delta = \theta \approx \sin\theta = \lambda/p < \lambda/d. \tag{3.1}$$

This will be used as a conservative estimate for the deviation of δ from zero. For a final frequency uncertainty Δf resulting from the angular uncertainty δ, an atomic beam of velocity v is considered at nearly perpendicular alignment with respect to the two counter-propagating laser beams of the ring interferometer. For one photon excitation, the spectra from the counter-propagating arms are registered separately; after the ring interferometer is aligned and dark fringe is achieved, the light of one

branch is blocked and the spectrum from the other beam is acquired and vice versa. The error Δf on the Doppler-free frequency calculated from the two spectra can be estimated from the error in δ using Eq. (3.1) by inserting into the following:

$$\Delta f = \frac{v}{\lambda} \sin \frac{\delta}{2} < \frac{v}{4d}. \tag{3.2}$$

3.3 Experimental setup

The Sagnac alignment method is demonstrated here for one-photon excitation LIF and two-photon REMPI spectroscopies on atomic beams (setup: *c*f. Fig. 3.1). The laser system employed, providing the fourth harmonic of an injection seeded titanium:sapphire (Ti:sapphire) narrowband oscillator with a pulse length of about 25 ns (repetition rate 10 Hz, linewidth $\approx$ 20 MHz) has been documented before,[39] as well as the application in one-photon[28] and two-photon[27] spectroscopies. The absolute calibration is performed on the seed light from a Coherent 899 (Ti:sapphire) ring laser using a femto-second frequency comb. In order to exclude any ambiguity on the choice of the right mode number of the frequency comb, a saturable absorption I_2-spectroscopy setup is available for pre-calibration and its use for the Yb spectroscopy is shown in Fig. 3.2. Frequency offsets between seed light and output of the pulsed oscillator — caused by frequency chirp and mode pulling — are taken into account by an online chirp-analysis.[27]

3.4 Results and Discussion

For demonstration in a one-photon LIF experiment the $6s^2 \rightarrow 6s\,30p_{3/2}$ $J = 1$ line in Yb I is investigated. Fig. 3.2 shows an overview recording for seven Yb isotopic lines, as well as a highly resolved spectrum of ^{74}Yb at a width of 43 MHz. The precision calibrations for Yb, as listed in Table 3.1, are obtained from averaging over LIF measurements for each of the counter-propagating laser beams crossing the Yb atomic beam. An analysis of the uncertainty budget is presented in Table 3.2. A similar precision calibration was performed on the $3s^2\,{}^1S \rightarrow 3s4p\,{}^1P$ line in Mg I, at an accuracy of 1 MHz.[28]

Two-photon Doppler-free spectroscopy on atomic beams is also affected by Doppler-shifts when the counter-propagating beams are not perfectly anti-parallel. The frequency deviation Δf on the two-photon level is a factor of 2 larger than given in Eq. (3.2). In this excitation scheme both beams are present in the interaction volume, so that a single scan yields a Doppler-free value. The signal is obtained by ionized product extraction using a time-of-flight (TOF) setup. Two-photon spectroscopy was performed on the $4p^6 \rightarrow 4p^5 5p[1/2]_0$ line in krypton. Calibration results are also displayed in Tables 3.1 and 3.2. Since the laser beam is collimated to about 1 mm diameter, the estimated accuracy of the beam overlap for 200 nm light is better than 0.1 mrad according to Eq. (3.1).

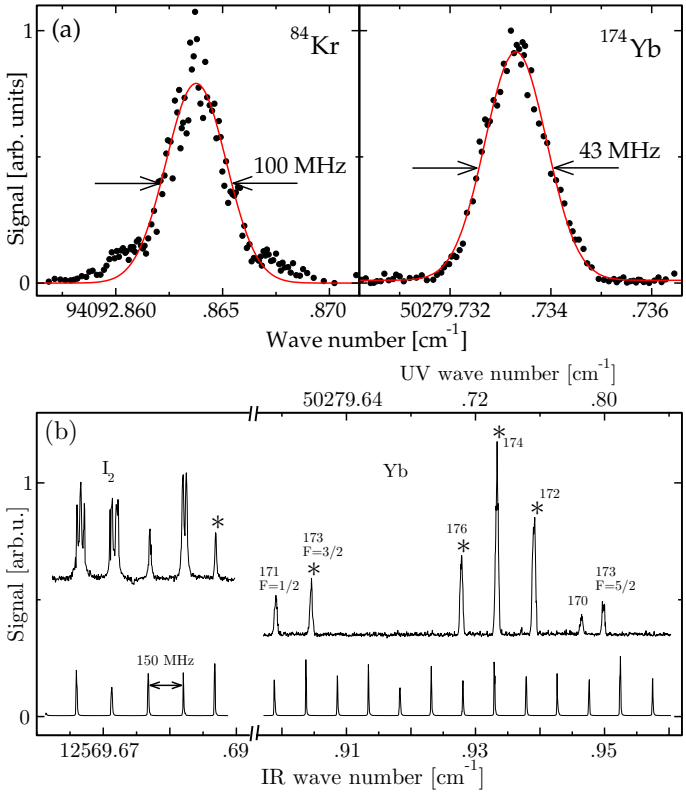

Figure 3.2 – *(color online) (a) Frequency comb calibration of the $4p^6 \rightarrow 4p^5 5p[1/2]_0$ two-photon transition in ^{84}Kr and the $6s^2 \rightarrow 6s\,30p_{3/2}$ $J = 1$ transition in the main ytterbium isotope. (b) Overview on the $6s^2 \rightarrow 6s\,30p_{3/2}$ $J = 1$ transition in Yb: a pre-calibration was performed using the b-component (marked with an asterisk) of the P(200) line of the $B \leftarrow X$ (0-14) band in I_2 at 12569.68739 cm^{-1}. Frequency comb calibrations are performed for Yb isotopic lines marked with an asterisk.*

The uncertainties of the frequency calibrations resulting from the first order Doppler effect depend on the typical beam velocities. For both cases (Yb and Kr) it is estimated to be smaller than 100 kHz. The dominating uncertainties in these experiments result from the characteristics of the laser output, most notably the frequency chirp, which depends on the pump energy applied on the pulsed oscillator and on the seeding wavelength. For the Krypton spectroscopy a seeding wavelength of $\lambda = 850$ nm is used, which gives rise to more pronounced frequency chirp as at wavelengths $\lambda = 800$ nm used for the ytterbium. In order to reduce chirp influences on the Kr calibration, the pulsed oscillator was operated at low pulse energies, which in turn increased the statistical fluctuations of the laser output energies and leads to a somewhat greater fit uncertainty.

The obtained transition frequency for the ^{84}Kr-line $\bar{\nu} = 94092.86387(25)\,\mathrm{cm}^{-1}$ is

Table 3.1 – *Results of the absolute calibrations.*

species	# scans	position [cm^{-1}]
^{84}Kr	20	94092.86387(25)
^{172}Yb	2 · 2	50279.711932(60)
^{174}Yb	8 · 2	50279.733339(33)
^{176}Yb	2 · 2	50279.755754(60)
^{173}Yb	2 · 2	50279.620239(80)

Table 3.2 – *Error budgets for each species. All values in MHz.*

uncertainty	Kr	^{174}Yb	other Yb
1st order Doppler	0.1	0.1	0.1
frequency comb	< 0.1	< 0.1	< 0.1
chirp	4	0.5	0.5
fit	3	0.5	2
AC-Stark	0.4	< 0.1	< 0.1
total	6	1	2

in good agreement with Witte *et al.*[55] who measured 94092.86399(12) cm^{-1} and with Brandi *et al.*[56] who provides a calibration for ^{86}Kr. Taking the accurately measured isotopic shift $\nu_{86} - \nu_{84} = 135.99(17)$ MHz from Witte *et al.* into account, Brandi's calibration corresponds to 94092.8627(13) cm^{-1} for ^{84}Kr, well within the specified confidence intervals.

In conclusion, Sagnac interferometry is an elegant technique to align two counter-propagating beams to exactly overlap. Calibration errors due to Doppler shifts in crossed beam configurations were reduced below the intrinsic accuracy limitations of the excitation laser system. The $6s^2 \rightarrow 6s\,30p_{3/2}$ $J = 1$ transition for ^{174}Yb was calibrated to the 6×10^{-10} accuracy level. The alignment precision is limited by the beam diameter of the excitation laser and can be improved by using larger diameters. Further improvement of the method can be accomplished by combining a fringe detection system with piezo actuators in an electronic feedback loop. The Sagnac interferometric method is especially useful, where "classical" methods of Doppler reduction fail. Additionally, no fiber coupling is involved — hence the method can be used for deep UV light as demonstrated. The Sagnac interferometer produces fringes even for light exhibiting short coherence lengths, which potentially makes it useful for quantum interference spectroscopies as presented in Witte *et al.*[55] at deep-UV wavelengths and by Zinkstok *et al.*[57] in the VUV.

Chapter 4

Frequency metrology on the Mg $3s^2\ ^1S \rightarrow 3s4p\ ^1P$ line for comparison with quasar data

We report a frequency metrology study on the Mg $3s^2\ ^1S \rightarrow 3s4p\ ^1P$ transition near 202.5 nm. For this purpose, the fourth harmonic of the output from an injection-seeded Ti:sapphire pulsed laser is employed in a Mg atomic beam experiment with LIF-detection. Absolute frequency calibration with a frequency comb laser is performed on the CW-seeding radiation, while the chirp induced frequency shift between the pulsed output and the seed light is monitored on-line. The resulting transition frequency for the main isotope ^{24}Mg is determined at 49346.756809(35) cm^{-1}. This value is three orders of magnitude more precise than the best value in literature. The line positions of the other isotopes ^{25}Mg and ^{26}Mg are also measured at comparable accuracy, giving rise to very exact values for the isotopic shifts. The achieved precision for the transition frequency at 7×10^{-10} level, makes this second resonance line of Mg I an additional candidate for inclusion in many-multiplet methods, aimed at detecting a possible temporal variation of the fine structure constant α from comparison with quasar spectra. The isotopic shifts obtained are also important to correct for possible systematic shifts due to evolution of isotopic abundances, that may mimic α-variation effects.

This chapter is published in Physical Review A **74**, 012505 (2006).

4.1 Introduction

The recent findings[1] claiming a possible variation of the fine structure constant $\alpha = e^2/4\pi\epsilon_0\hbar c$ touch upon the very foundations of physics. In a recent analysis by Murphy *et al.*[58] combining data from 128 quasar absorption systems over redshift ranges of $0.2 < z_{\rm abs} < 3.7$ show $\Delta\alpha/\alpha = (-0.543 \pm 0.116) \times 10^{-5}$, a result at the 5σ confidence level. Notwithstanding the detailed data reduction and error analysis[59] the findings of the Australian based group, using the Keck telescope for observations of quasars on the northern hemisphere, are disputed by other groups, using the

Very Large Telescope of the European Southern Observatory, monitoring quasar absorption systems on the southern hemisphere.[60,61]

The method used to extract information on a possible variation of α, the many-multiplet (MM) method,[62] includes a number of atomic (and ionic) fine-structure splittings in a comparison between quasar and zero-redshift absorption features. The method requires extensive first principles atomic-structure calculations of relativistic corrections to level energies, resulting in characteristic q-factors for each atomic transition that represent the sensitivity for a certain spectral line to depend on a variation of α. The q-factors for a number of atomic and ionic spectral lines including magnesium have been calculated.[63] For the transition frequencies at $z = 0$ the most accurate literature values are used in the comparisons, but for many lines the uncertainties in the laboratory spectra are equally large, or even larger, than those of the quasar features. Recently Berengut *et al.*[2] have produced a list of lines that could be implemented in the MM-method to improve constraints on variation of α, if improved laboratory data would become available. The $3s^2\,{}^1S \rightarrow 3s4p\,{}^1P$ transition in Mg I was identified as one that needed a more accurate rest-frame frequency determination.

In addition, because isotope abundances in the early universe and at distant locations in space may differ from those on Earth, accurate measurements of isotope shifts are required to quantify systematic effects and to prevent varying isotope abundances from mimicking variations of α. In particular for magnesium, contributing several lines to the MM-methods with large isotopic shifts, there exists an ongoing dispute on the isotopic evolution of the abundance ratio and its consequences for variations of α.[64–66] For these reasons a renewed interest has arisen in the determination of isotope shifts through refined *ab initio* calculations.[67,68]

In view of the need for improved spectral data the Mg I $3s^2\,{}^1S \rightarrow 3s4p\,{}^1P$ spectral line near 202 nm is reinvestigated. The most accurate determination of the transition frequency for this second resonance line in the singlet system of magnesium dates back to the classical study of Risberg.[69] While the $3s^2\,{}^1S \rightarrow 3s3p\,{}^1P$ first resonance line has been the subject of many high resolution investigations, focusing on the absolute transition frequency,[70,71] the isotope shift,[72–74] and even the hyperfine structure of ^{25}Mg,[75] such detailed studies have not been performed for the 4p level.

In the present experimental investigation, a pulsed laser source, tunable near 202 nm, is used for exciting the $3s^2\,{}^1S \rightarrow 3s4p\,{}^1P$ in Mg. This approach, with the unavoidable intrinsic broadening due to the pulse structure of the light source, is chosen because of the difficulty in producing radiation in the deep-UV via nonlinear conversion with continuous-wave lasers. Using a novel-design pulsed titanium:sapphire (Ti:sapphire) oscillator in the near infrared range, three stages of nonlinear conversion are required to attain deep-UV wavelengths.[39] The frequency metrology using a home-built frequency comb laser setup[55,76] is performed on the output of the continuous-wave (CW) laser, which also seeds the oscillator cavity of the pulsed laser system. As is known from pulsed-dye laser systems, frequency excursions during the temporal pulse evolution (known as frequency chirp) may cause

a net shift between the center frequency of the pulse and the CW-frequency seeding the pulsed amplifier.[16,18,20] For the calibration of the singlet 3s4p level in Mg extensive measurements on these chirp effects were performed. It turned out that they are a limiting factor to the attainable accuracy in the transition frequency.

4.2 Experimental setup and procedures

4.2.1 Mg atomic beam setup

Fig. 4.1 depicts the term levels of the singlet system in Mg which are relevant for the excitation and detection scheme used in the present study. The excited 3s4p state has a lifetime of 14 ns[77] and decays back to the ground state via three channels. While the resonant decay has a branching ratio[78] of ≈ 85 %, both of the remaining two channels — 2 % via 3s4s, 13 % via 3s3d — decay to the 3s3p level that eventually emits 285 nm light upon relaxation to the ground state. This allows for off-resonant fluorescence detection at 285 nm with the advantage of efficient filtering of the 202 nm background with a Schott UG5 color filter.

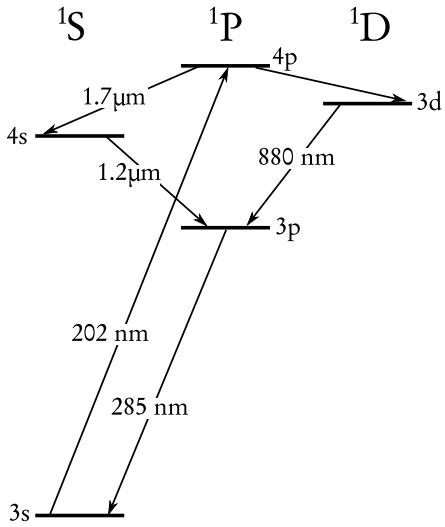

Figure 4.1 – *Term level scheme of the singlet system of Mg showing the excitation and decay channels of the 3s4p ^{1}P level investigated. The laser excitation is at 202 nm and the 285 nm fluorescence from the 3s3p to the ground state is monitored in the experiment.*

A schematic of the atomic beam apparatus including the laser excitation and laser-induced fluorescence (LIF) detection zone is shown in Fig. 4.2. Magnesium pellets are heated in an oven to about 700 K producing an effusive atomic beam that is collimated downstream by two skimmers (S1: 0.5 mm diameter and S2: 2 mm diameter) to reduce the transversal velocity spread. The line broadening due to the transversal velocity spread of the skimmed atomic beam is about 20 MHz.

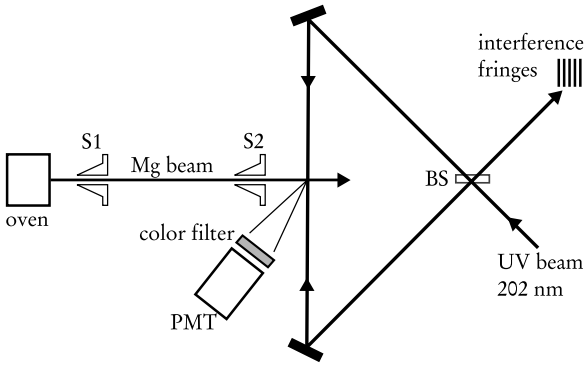

Figure 4.2 – *Experimental arrangement of the off-resonance laser-induced fluorescence detection using a collimated Mg atomic beam. The excitation laser beam is split and the two paths are aligned to be perfectly counterpropagating, making use of the Sagnac-interferometer configuration. S1 and S2 – skimmers; BS – beam splitter; PMT – photomultiplier tube.*

Any deviation from perpendicular alignment of the atomic and laser beams will result in a Doppler shift. To address this issue, the laser beam is split into two paths and then aligned such that the laser beams are counterpropagating collinearly as they cross the atomic beam. As long as the two laser beams are exactly counter-propagating, the first-order Doppler shifts in both beams will be of opposite signs and the unshifted line position can be obtained by taking the average of the line positions resulting from either laser path. The burden of establishing perpendicular atomic and laser beam alignment is then transposed to ensuring that the counter-propagating laser beams are perfectly aligned. However, it should be noted, that the laser beams are aligned preferably perpendicularly to the atomic beam in order to achieve maximum signal to noise ratio.

An interferometric technique is employed in order to align the counterpropagating beams to less than $\delta = 0.1\,\mathrm{mrad}$ misalignment, which corresponds to a Doppler shift of about 350 kHz in the deep-UV. As shown in Fig. 4.2, the excitation laser beam is split into two paths and then recombined to form a Sagnac interferometer. Special care was taken to ensure that the distances between beam splitter and interaction region are equally long for both light branches and that the two arms are of comparable intensity. Moreover, the light is collimated with a beam diameter of about 1 mm at the interaction region. The advantage of the Sagnac setup is its robustness against acoustic disturbances which modulate the arm length of the interferometer. Since those disturbances affect both counter-propagating light beams in the same way, the path difference and likewise the interference pattern remains unchanged. In fact the interference pattern is predominantly influenced by the angle δ between the two contributing arms. When δ is lowered to zero the interference will show a dark fringe, which is especially useful as a sensitive alignment technique. In a two beam interference pattern the relation between fringe periodic distance L

and the angular misalignment θ of the two interfering beams is given by:

$$\frac{\lambda}{L} = \sin\theta \approx \theta = 2\delta. \tag{4.1}$$

Geometric consideration shows that an angular mismatch δ between the counter-propagating beams within the Sagnac interferometer will lead to an angle $\theta = 2\delta$ on the screen. The attainable accuracy for the angular alignment is restricted by the beam diameter, because it determines the spot size on the screen and likewise the maximum resolvable fringe period L. Identifying the fringe period L with the beam diameter $d = 1\,\text{mm}$ yields the aforementioned possible misalignment of $\delta = 0.1\,\text{mrad}$. Since the interferometer alignment does not drift from dark fringe to the first order fringe pattern showing up on the screen the accuracy for δ is actually better. Still this uncertainty level is kept as a conservative measure. A more detailed discussion of the interferometric alignment to eliminate first-order Doppler shifts shall be provided in a forthcoming article.

4.2.2 The deep-UV laser source

A schematic representation of the laser system and frequency metrology setup is shown in Fig. 4.3. The UV laser source has been described in some detail before.[39] The system consists of a Ti:sapphire pulsed oscillator that is injection-seeded with light from a CW Ti:sapphire ring laser and is actively locked using the Hänsch-Couillaud (HC) scheme. The pulsed oscillator produces Fourier-limited pulses of 20 MHz linewidth centered at the CW-seed wavelength of about 810 nm, with a typical pulse energy of 0.1 mJ. The pulses are subsequently sent through an 8-pass amplification stage to enhance the pulse energy to about 8 mJ. In order to produce the fourth harmonic at 202.5 nm, three consecutive nonlinear upconversion stages — BBO crystals cut at appropriate type-I phase matching angles — are used.[39] The resulting radiation near 202.5 nm has a repetition rate of 10 Hz, bandwidth 40 MHz, and a typical pulse length of about 15 ns. The pulse energy of the excitation laser beam can be chosen by varying the pump power sent to the multi-pass amplifier. The laser system reaches maximum output energies of 0.2 mJ/pulse at the 4th harmonic. However, in order to reduce saturation effects typical pulse energies of not more than $0.1\,\mu$J were applied, corresponding to a peak intensity of about $1\,\text{kW/cm}^2$ at the interaction zone. Observed linewidths were about 50 MHz, which corresponds to the width one expects when convoluting the laser linewidth, the residual Doppler broadening and the natural linewidth of the $3s^2\,{}^1S \rightarrow 3s4p\,{}^1P$ transition.

Since the absolute frequency calibration is performed on the CW Ti:sapphire seeding radiation, it is necessary to assess the possible frequency difference between the pulsed output and the injected seeding light. Such frequency offsets might be caused by frequency excursions during the temporal pulse evolution (chirp) due to the intensity-dependent refraction index of the lasing medium [16,18,20] and by dynamical mode-pulling effects in the pulsed oscillator resonator. In order to address both effects, strategies were followed recently explored by White *et al.*[22,24] for determining

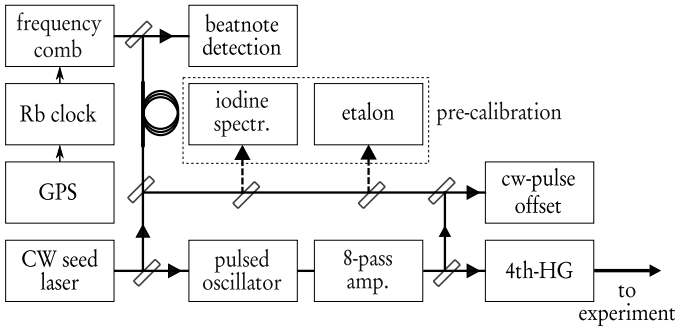

Figure 4.3 – *Schematic representation of the experiment. The amplified output of a Ti:sapphire pulsed oscillator is upconverted to the 4th harmonic, and the resulting 202.5 nm light is used in the atomic beam setup as depicted in Fig. 4.2. The CW – pulse frequency offset is monitored throughout the measurement. The frequency of the CW Ti:sapphire seed radiation is measured with a fs-frequency comb, which is referenced to a Rb-frequency standard with GPS time correction. A pre-calibration with an I_2 saturation set-up is performed to determine the correct mode of the frequency comb.*

chirp phenomena in an injection-seeded and pulsed optical parametric oscillator. A more extensive description of the CW – pulse frequency offset characterization will be given in a forthcoming publication.[27]

It is possible to adjust the CW – pulse offset and set it close to zero by changing parameters of the pulsed oscillator HC-lock. The frequency chirp is minimized by lowering the pump power to the pulsed oscillator. Typically, the CW – pulse frequency offset is centered around zero and has a standard deviation of less than 0.5 MHz, for the entire duration of the measurement. During the spectroscopic scans a multitude of data from each single pulse is registered. We use a single oscilloscope to measure the LIF signal, the UV power, and the net CW – pulsed frequency difference from each laser pulse acquired. This correlated acquisition technique allows for data filtering in the analysis procedure. Thus it is possible to use the power fluctuations of the UV-laser output, simply by taking many data points during one scan. The acquired data is subsequently binned with respect to the UV pulse intensity. By this means possible excitation intensity dependent line shifts can be assessed during the scans.

4.2.3 Absolute calibration procedures

The absolute calibration is performed on the CW seeding light from the Ti:sapphire ring laser. Part of the CW seed light is coupled through a 100 m single-mode optical fiber towards the lab where a frequency comb reference laser[55] is located. The CW-light is heterodyned with the output of this frequency comb and the radio-frequency beatnote is detected in a spectrometer setup using an avalanche photodiode (PD).

Typically, the beatnote detection reached a s/n of 45 db. The two main parameters of the frequency comb are its carrier-envelope phase offset frequency ν_{ceo} and its repetition rate ν_{rep}. Both are locked to a Rubidium-clock standard, which is further referenced to the synchronization signal of the global positioning system (GPS). From the locking characteristics, and from the fact that a scan over one isotopic line takes about two minutes the precision of the calibration with the frequency comb is estimated to be better than 25 kHz — which corresponds to an accuracy of < 100 kHz in the deep-UV.

An absolute calibration with a frequency comb requires the frequency to be known in advance within a fraction of the frequency spacing of neighboring modes in the comb, which is equal to the repetition rate of the laser ($\nu_{rep} \approx 75$ MHz). Since the $3s^2\,{}^1S \rightarrow 3s4p\,{}^1P$ transition frequency is only known[69] within 0.07 cm^{-1}, a precalibration procedure is required. For that purpose, part of the CW seeding light is used to perform iodine saturation spectroscopy in a setup developed by the Hannover group[79] specially suited for the near-infrared wavelength region. It consists of an iodine cell which is heated to about 900 K in order to populate high rovibrational levels in the $X\,{}^1\Sigma_g^+$ ground state of I_2. For reducing the pressure in the cell, it has a cold finger extension which is temperature stabilized at room temperature. After the precalibration the transition frequency of the Mg $3s^2\,{}^1S \rightarrow 3s4p\,{}^1P$ line is known to a 10 MHz level of accuracy, which is sufficient for the final calibration using the frequency comb.

4.2.4 Measurement procedures

Since the frequency comb laser is situated in a different laboratory, the data acquisition and scan control software is divided on two separate PCs which are linked via TCP/IP on a 100 Mbit/s ethernet connection. The system will be described in a forthcoming paper in detail.[27] In short, the PC in the spectroscopy lab runs the actual laser scan and acquires and stores all retrieved data. On each scan step it sends a beatnote count request to the PC which controls the frequency comb, and receives the essential data from the frequency comb: the repetition rate ν_{rep}, the carrier envelope offset frequency ν_{ceo}, and the measured beatnote frequency ν_{bn} between frequency comb and CW-seed light.

The experimental procedure is as follows: The seed laser is tuned stepwise in frequency with an external control voltage provided by an arbitrary waveform generator (Agilent AWG 33250A). Each scan is about 200 MHz wide (in the deep-UV) and consists of about 300 equidistant voltage steps. While the CW-laser frequency is scanned the beatnote between frequency comb and CW-light changes likewise. In order to keep the beatnote frequency within a range of 21.7 ± 2 MHz — which is the working range of a frequency band pass filter in the electronic beatnote frequency counting circuitry — the repetition rate of the frequency comb is adjusted after each scan step, so that the frequency components of the comb spectrum follow the seed light scan.[27] At each scan step the acquisition software obtains the relative UV-power, the CW – pulse frequency offset, and the LIF signal of 10 laser shots. At

the same time the computer, which controls the frequency comb, counts the beat-note frequency 10 times per scan step within time gates of 0.1 s for each individual count. From those 10 frequency counts the average value is used for the calibration, while the standard deviation is a measure for the short term frequency jitter of the seed laser, which is about 1 MHz.

4.3 Results

The Mg spectrum with the I_2 calibration line and the etalon markers are shown in Fig. 4.4. The spectrum obtained from the counter-propagating beam is also indicated in the same figure. The angle between the light beam and the atomic beam was purposely misaligned from the near-perpendicular orientation to demonstrate a clear separation of the line centers obtained from either light beam paths. For the subsequent calibrations using the frequency comb, the light beams were aligned back to the perpendicular setting. The positions of the hyperfine components of the I_2 R144 (0-16) rovibrational line of the B – X transition used for the calibration were taken from the prediction software developed by the Hannover group.[79] The CW – pulse offset was set to be approximately zero throughout the measurements.

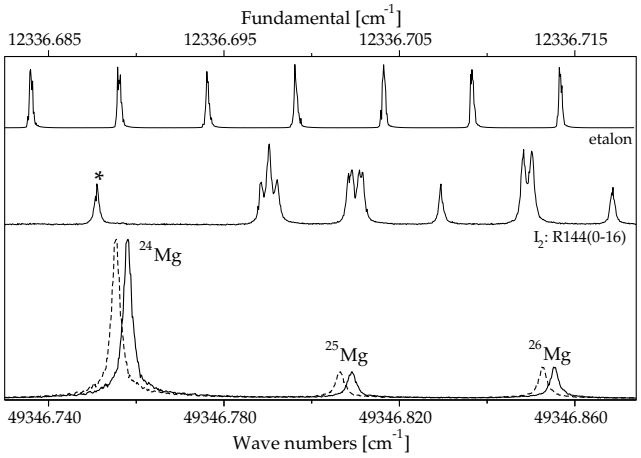

Figure 4.4 – *The $3s^2\,{}^1S \rightarrow 3s4p\,{}^1P$ Mg spectrum showing the isotope splittings. A fraction of the seeding radiation at the fundamental wavelength is used to record the I_2 saturation signal and etalon markers (150 MHz-FSR) for pre-calibration. The Mg spectrum obtained for the counter-propagating laser beam is drawn with a dashed curve. The t-hyperfine component of the R144 line in the B – X (0-16) band, predicted[79] at 12336.68774 cm^{-1}, is marked with an asterisk.*

First, calibration scans on the most abundant isotope ^{24}Mg were performed. In order to obtain a Doppler-free frequency value for the $3s^2\,{}^1S \rightarrow 3s4p\,{}^1P$ transition, the Sagnac interferometer is first aligned until dark fringe is achieved. Then for each of the two light branches of the interferometer two scans are performed — one by

tuning the laser from lower to higher frequencies and another scan with opposite tuning direction. For each of the four scans, a center line position is obtained by nonlinear least square fitting. Their arithmetic average gives the final transition frequency.

In order to check the reproducibility of the calibration the full procedure has been repeated 5 times. After each of the four-scan measurements not only the Sagnac dark fringe was realigned, but also the phase-matching of the upconverting nonlinear crystals has been checked and optimized. Hence possible systematic frequency shifts, as a result of imperfectly aligned phase-matching angles or Sagnac dark fringe acquire a statistical characteristic. Additionally, the relative UV excitation intensity has been changed by one order of magnitude, without showing any significant effect on the calibrated line position. In Table 4.1 the average value of the 5 calibrations is given. The contributions to the uncertainty budget are discussed below.

For the ^{25}Mg and ^{26}Mg isotopes two complete scan sets consisting of 4 scans each were registered. The obtained frequencies are also given in Table 4.1. Additionally, since the isotopic shifts can be obtained from relative measurements, after performing one complete scan set on ^{24}Mg the Sagnac interferometer was not realigned. Instead the seed laser was directly tuned to the other isotopic lines where spectroscopic scans were performed and frequency differences obtained by comparing the line positions from a single interferometer arm only. The line positions for the less abundant isotopes given in Table 4.1 result from combined averaging of the two absolute calibrations and a number of relative measurements. The slightly larger uncertainties are due to the lower signal to noise ratio on the LIF signal of the weaker isotopes.

Table 4.1 – *The line positions of the Magnesium isotopes for the $3s^2\,{}^1S \rightarrow 3s4p\,{}^1P$ transition. The isotopic shifts obtained from the experiment are compared to ab initio calculations by Berengut* et al.[68] *The given uncertainty intervals for the experimental values represent the final uncertainties as listed in Table 4.2.*

isotope	position (cm^{-1})	shift from ^{24}Mg (MHz) exp	calc[68]
^{24}Mg	49346.756809(35)	–	–
^{25}Mg	49346.807724(40)	1526.4(1.2)	1530(50)
^{26}Mg	49346.854173(40)	2918.9(1.2)	2950(50)

The scans on ^{25}Mg did not give significantly different measured linewidths compared to the even isotopes, which points to the fact that a possible hyperfine splitting on the odd isotope is very small. *Ab initio* calculations of the hyperfine constant A for the 3s4p ^{1}P state yield a value of $A = -3.3$ MHz,[80] which would lead to the hyperfine levels $\Delta E_{\mathrm{hfs}} = (-8.25, 3.3, 11.55)$ MHz for $F = (7/2, 5/2, 3/2)$. With an observed linewidth of 50 MHz for the main ^{24}Mg isotope — which is the convoluted linewidth of the instrumental width and the natural linewidth of the $3s^2\,{}^1S \rightarrow 3s4p\,{}^1P$ transi-

tion — it is impossible to resolve such a hyperfine structure, which is in agreement with the experiment.

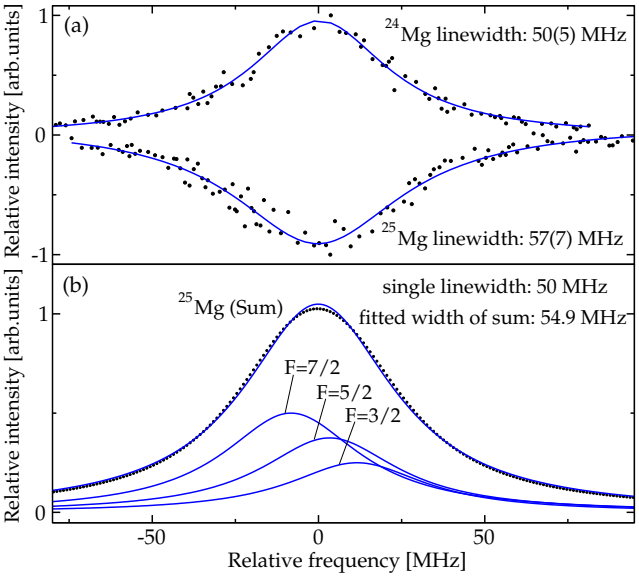

Figure 4.5 – *(Color online) Comparison of the observed lineshapes of the main ^{24}Mg isotope and the odd ^{25}Mg isotope (a). In the lower part (b) the three single hyperfine contributions with a linewidth as found on the main isotope (50 MHz) are separately depicted. The calculated sum of the three overlapping features is also shown as dotted curve and a fit against the result is performed and depicted as solid line. Even though the hyperfine splitting between the F=7/2 and F=3/2 is about 20 MHz, the linewidth of the sum is only marginally larger than a single peak linewidth.*

In order to assess a possible line broadening for the observed ^{25}Mg lineshape as a result of the calculated hyperfine splitting, a superposition of the three hyperfine lines is simulated using the observed linewidth of the ^{24}Mg isotope (see Fig. 4.5). In the upper part (a) of the figure, averaged data is shown as dots for the main ^{24}Mg and the ^{25}Mg isotope. Each dot represents an average of 4 pulses on the ^{24}Mg data and of 7 pulses on the ^{25}Mg data. The solid curves depict fitted Lorentzian lines. The given linewidths in part (a) of the figure represent average values from a multitude of spectroscopic scans. There is no significant difference in the observed lineshapes of the ^{24}Mg and the ^{25}Mg isotopes as the small suggested difference can be explained by noise broadening — the observed linewidth of ^{26}Mg is 60(9) MHz. Figure 4.5(b) shows the three simulated hyperfine lines (Lorentzian shape) which are intensity weighted by their multiplicities. The sum of the hyperfine lines is depicted as a dotted curve, which is fitted by another Lorentzian curve shown as solid line. Even though the hyperfine splitting between $F = 7/2$ and $F = 3/2$ is about 20 MHz the resulting superposition gives only a small additional line broadening by about 5 MHz, which would not be visible in our experiment. It should be noted that

the line center of the fitted curve in Figure 4.5(b) is found exactly on the center-of-gravity of the simulated hyperfine structure. We conclude that the calculated hyperfine splitting constant $A = -3.3\,\mathrm{MHz}$ fits well within our observed linewidth.

Table 4.2 – *Error budgets on the absolute calibration given in kHz at the deep-UV energy scale. The total confidence interval is obtained by taking the quadrature sum of the errors i – vi and linear summation of the result with the errors v–vii. Errors iii and iv represent the 1σ-uncertainties of the nonlinear least square fit.*

	Error	kHz
i	1st order Doppler	350
ii	frequency comb	< 100
iii	fit error ^{24}Mg	200
iv	fit error ^{25}Mg,^{26}Mg	450
v	ac-Stark	100
vi	CW – pulse offset	500
vii	2nd order Doppler	8
	total ^{24}Mg	1050
	total ^{25}Mg,^{26}Mg	1200

The contributions to the experimental error budget are listed in Table 4.2. The table is split into two parts. Since the errors *i*–*iv* have statistical characteristics and are not related, quadrature summation is applied on them. It should be noted that error *iv* is only relevant for the isotopic shifts. The errors *v* and *vi* are of systematic character and estimated as maximum deviations. Error *vii* (second order Doppler) is also systematic, but very small and can be neglected. For the total error budget the quadrature sum over errors *i* – *iv* has been added to the linear summation of errors *v* and *vi*. It represents a final uncertainty for the resulting values for the absolute calibration and isotopic shifts.

As discussed earlier for the 1st order Doppler error (position *i* in Table 4.2) a conservative budget is given. In practice it turns out that the dark fringe alignment is quite stable and does not drift to a bright interference maximum during the measurements. Moreover the persistent realignment of the Sagnac interferometer for each measurement procedure turns this possible systematic error into a statistical one, and can hence be reduced when taking more spectroscopic scans. The actual experimental spread (1σ) for the ^{24}Mg linecenter frequencies is 510 kHz and about 600 kHz for the isotopic shifts, which is well below the given total error bars in Table 4.2. The ac-Stark effect was too weak to be measured at the power levels used in a range $0.03 - 0.3\,\mu\mathrm{J/pulse}$. We estimate an upper limit to the ac-Stark shift based on the obtained statistics. For a more elaborate treatment of the CW – pulse frequency deviations as a result of chirp, we refer to Hannemann *et al.*[27] The frequency

comb measurements result in line positions which are about 15 times more accurate compared to the I_2 pre-calibration procedure.

The final value for the transition frequency of the $3s^2\,{}^1S \rightarrow 3s4p\,{}^1P$ line entails an improvement of about 3 orders of magnitude from the results of classical spectroscopy by Risberg.[69] To our knowledge, the present experiment is the first to resolve the isotopic shifts for this transition. The precision of the isotopic shifts is comparable to those obtained by Hallstadius[72] for the $3s^2 \rightarrow 3s3p$ transition. We also tabulate the calculated isotopic shift using the parameters from Berengut *et al.*[68] The comparison shows very good agreement between the experimental and the theoretical results.

It should be noted that the red shifted quasar absorption spectra do not resolve the isotopic structure of the $3s^2\,{}^1S \rightarrow 3s4p\,{}^1P$ line. Instead the resolution is given[58] as FWHM $\approx 6.6\,\mathrm{km/s}$ which corresponds to 33 GHz at 202 nm. Using our results and the natural isotopic abundances on Earth as found in Rosman *et al.*[81] — ^{24}Mg: 78.99(4) %, ^{25}Mg: 10.00(1) %, ^{26}Mg: 11.01(3) % — a merged line is simulated using the three isotopic lines each having a FWHM of 33 GHz. The resulting line center is found at $49346.77252(7)\,\mathrm{cm}^{-1}$. This value, folded over the isotopic components, agrees within the 1σ uncertainty limit with the value reported by Risberg: $49346.729(70)\,\mathrm{cm}^{-1}$. During the review of this paper we learned about another spectroscopic study of the $3s^2\,{}^1S \rightarrow 3s4p\,{}^1P$ transition in Mg I. Aldenius *et al.*[82] measured $49346.771(3)\,\mathrm{cm}^{-1}$ based on Fourier-transform spectroscopy in which the isotopic components are not resolved. This value is a factor of 20 more accurate than the value of Risberg, and is in perfect agreement (within 1σ limits) with the present value of the folded line.

4.4 Conclusion

We have performed an accurate determination of the $3s^2\,{}^1S \rightarrow 3s4p\,{}^1P$ transition frequencies of the three Magnesium isotopes — ^{24}Mg, ^{25}Mg and ^{26}Mg. This investigation is motivated by current studies on the absorption spectra of extragalactic gas clouds at high redshift to probe a possible variation of the fine-structure constant α. With the frequency determination at the level of 7×10^{-10}, the Mg $3s^2\,{}^1S \rightarrow 3s4p\,{}^1P$ line may represent a welcome addition to the set of transitions used in the many-multiplet analysis in the search for a variation of α.

The isotope shift obtained at an 1 MHz accuracy should be helpful in assessing systematic effects that imitate an α-variation due to the possible evolution of isotopic abundance.[65] For example, when taking the possible change in α as:

$$\frac{\Delta\alpha}{\alpha} = (-0.543 \pm 0.116) \times 10^{-5} \tag{4.2}$$

from Kozlov *et al.*[65] and $q = 87\,\mathrm{cm}^{-1}$ for the $3s^2\,{}^1S \rightarrow 3s4p\,{}^1P$ transition in Mg as given in Berengut *et al.*,[2] the transition frequency ν_{Mg} (unresolved for the isotopic

contributions) should have been different by

$$\Delta\nu_{\mathrm{Mg}} \quad = \quad 2q\frac{\Delta\alpha}{\alpha} = -28.3(6.1)\,\mathrm{MHz} \tag{4.3}$$

10^{10} years ago. With the isotopic shift obtained from this experiment a comparable change in ν_{Mg} could be mimicked by a 1% different abundance of ^{24}Mg in the isotopic composition of the magnesium used in the lab and existing at the point in space-time, where the quasar absorption spectra were imprinted.

In addition, the values of the isotopic shifts for this transition are found to be in good agreement with the *ab initio* calculations of Berengut *et al.*[68] It is reassuring that the theoretical predictions are in such good agreement, since the sensitivity coefficients q for possible variations of α [62,63] are calculated within the same framework.

Acknowledgment

The Netherlands Foundation for Fundamental Research on Matter (FOM) is gratefully acknowledged for financial support. We thank Dr. H. Knöckel (Hannover) for providing us with the I_2-cell for near-IR saturation spectroscopy, Dr. L. Veseth (Oslo) for calculating the hyperfine constant in ^{25}Mg, Dr. J. Berengut (Sydney) for valuable discussions, and Dr. M. T. Murphy (Cambridge) for sending us the manuscript on the recent Fourier-transform measurements prior to publication.

Chapter 5

Frequency metrology on the $EF\,^1\Sigma_g^+ \leftarrow X\,^1\Sigma_g^+$ (0,0) transition in H_2, HD, and D_2

We present a frequency metrology study on the lowest rotational levels of the hydrogen $EF\,^1\Sigma_g^+ \leftarrow X\,^1\Sigma_g^+$ (0,0) two-photon transition near 202 nm. For this purpose the fourth harmonic of an injection-seeded titanium:sapphire pulsed oscillator is employed in a Doppler-free REMPI-detection scheme on a molecular beam of hydrogen. A frequency comb laser is used to perform the absolute frequency calibration on the CW laser that injection-seeds the oscillator. Chirp-induced frequency differences between the output of the pulsed oscillator and the seeding light are monitored on-line, while possible systematic shifts related to the AC-Stark and Doppler effects are addressed in detail. The transition frequencies of the Q(0) to Q(2) lines in H_2 and D_2, and the Q(0) and Q(1) lines in HD are determined with an absolute accuracy at the 10^{-9} level.

This chapter is published in Physical Review A **74**, 062514 (2006).

5.1 Introduction

Accurate determination of the dissociation and ionization energies of the hydrogen molecule and its isotopomers is an important test ground for quantum *ab initio* calculations on molecular systems.[83,84] The pioneers in this field, Kołos[85] and Wolniewicz[86] calculated values for the ionization potential of H_2 ranging from 124 417.491 cm^{-1} to 124 417.496 cm^{-1}, including adiabatic, non-adiabatic, relativistic and radiative corrections to the Born-Oppenheimer results, believed to be accurate to within 0.01 cm^{-1}. The best theoretical value for the adiabatic dissociation limit is calculated to be 36 118.060 cm^{-1}.[86]

At the experimental side, different approaches have been adopted to retrieve increasingly accurate values for these two key quantities. Stoicheff and coworkers[87] directly excited the region near the $n = 2$ dissociation threshold resulting in a value for the ground state dissociation threshold $D_0(H_2)$ with an accuracy of 0.08 cm^{-1}.

Eyler and coworkers showed that the region near the $n = 2$ threshold is prone to spin-orbit and hyperfine effects as well as perturbations between several electronic states, yielding an irregular structure of many resonances near threshold[88] and later obtained a value for $D_0(H_2)$ in a two-step excitation process.[89]

The ionization potential in hydrogen can be determined from direct one-photon excitation of the np Rydberg series and extrapolation to the series limit using multichannel quantum defect theory (MQDT). This approach was taken by Greetham *et al.*[90] to deduce a value for the ionization potential of HD. Alternatively the ionization potential may be derived from a number of consecutive excitation steps bridging the gap between the $X\,^1\Sigma_g^+$, $v = 0, J = 0$ ground state and the ionization limit. One such route was explored by De Lange *et al.*[91] who calibrated a high-lying vibrational level ($v = 19$) in the $EF\,^1\Sigma_g^+$ state and then connected to the ionization limit through the Fourier-transform infrared work on inter-Rydberg transitions by Jungen *et al.*[92] This scheme is fundamentally limited by the fact that a transition needs to be calibrated in the $B\,^1\Sigma_u^+ \rightarrow X\,^1\Sigma_g^+$ system, probing an upper state with a lifetime as short as 0.3 ns.

A promising multi-step scheme involves calibration of the lowest $EF\,^1\Sigma_g^+$, $v = 0$ level (with a lifetime of 200 ns[35] and therewith allowing for precision spectroscopy), which can be reached in a two-photon transition allowing for Doppler-free excitation. This scheme was explored already some time ago by Glab and Hessler[93] and by Eyler and coworkers.[94–97] The concept of the multi-step scheme is to determine the ionization potential from accurate calibration of the $EF\,^1\Sigma_g^+$, $v = 0, J = 0$ level, subsequently excite the long-lived np Rydberg series and then extrapolate this series to the limit with the aid of improved Fourier-transform infrared transitions between high-n levels[98] and by millimeter wave transitions between very high-n levels.[99] A recent reinvestigation of the $EF\,^1\Sigma_g^+ \leftarrow X\,^1\Sigma_g^+(0,0)$ two-photon transition by Eyler and coworkers constitutes an important improvement to this approach. Transition frequencies at an absolute accuracy of 0.008 cm^{-1} were obtained,[100] that differed from earlier investigations by as much as three standard deviations. Such discrepancy warrants an independent validation by alternative methods, and that is the purpose of the present study.

In the present experimental investigation a pulsed laser source, tunable near 202 nm, is used for exciting the Q(0) to Q(2) lines of the $EF\,^1\Sigma_g^+ \leftarrow X\,^1\Sigma_g^+(0,0)$-band in H_2 and D_2, as well as the Q(0) and Q(1) lines in HD, in a two-photon Doppler-free resonance-enhanced multi-photon ionization (REMPI) scheme. Using a novel-design pulsed titanium:sapphire (Ti:sapphire) oscillator in the near infrared range, three stages of non-linear conversion are required to attain deep-UV wavelengths.[39] The frequency metrology is performed on the output of the continuous-wave (CW) laser, that seeds the oscillator cavity of the pulsed laser system, by referencing against a home-built frequency comb laser.[55,57] As is known from pulsed-dye laser systems, the amplification process can induce frequency excursions during the temporal evolution of the pulse (known as frequency chirp), which may cause a net shift between the center frequency of the pulse and the carrier-frequency seeding the pulsed ampli-

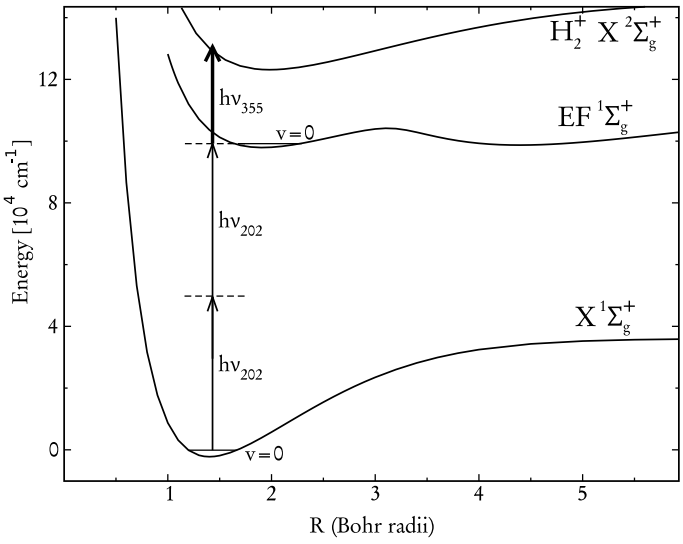

Figure 5.1 – *Potential diagram of molecular hydrogen and the applied 2 + 1-REMPI excitation scheme. The zero energy is identified with the ground state.*

fier.[16,18,20] For the absolute calibration of the Q(0), Q(1), and Q(2) transitions in the hydrogen $EF\,^1\Sigma_g^+ \leftarrow X\,^1\Sigma_g^+(0,0)$-band we have performed extensive measurements on these chirp effects and corrected for them. Although the underlying physics of the chirp process is somewhat different (frequency mode-pulling in a resonator vs. transient gain in a traveling-wave dye-amplifier) the phenomenology of the effect is similar. We followed strategies recently explored by White *et al.*[22,24] for determining chirp phenomena in an injection-seeded and pulsed optical parametric oscillator.

5.2 Experimental setup and procedures

The $EF \leftarrow X$ two-photon resonances are detected using Doppler-free 2 + 1-REMPI. An excitation scheme including potential energy curves is given in Fig 5.1. The essential ingredients of the experimental components and the measurement procedures are described in detail in the following sections: 5.2.1 The geometrical layout of a molecular gas jet perpendicularly crossing a set of counter-propagating laser beams with 2 + 1-REMPI detection. A special interferometric alignment scheme was followed (based on the Sagnac geometry) to ensure exact overlap of the counter-propagating beams; 5.2.2 A novel-design tunable deep-UV laser system operating at 202 nm, involving fourth harmonic generation of the amplified output of an injection-seeded pulsed Ti:sapphire oscillator; 5.2.3 The absolute frequency calibration of the near-IR seeding light using a fs-laser frequency comb; 5.2.4 The assessment of the frequency chirp effect; 5.2.5 The assessment of possible shifts due to DC and AC-Stark effects; 5.2.6 Discussion of possible effects of phase distortions introduced

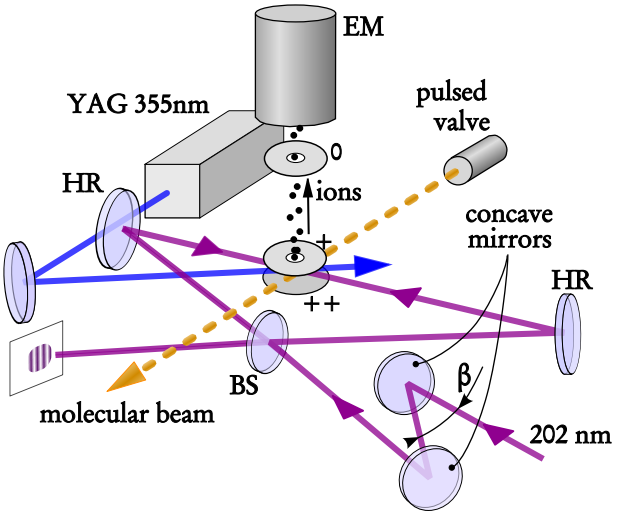

Figure 5.2 – *(color online) Experimental apparatus used for Doppler-free 2 + 1-REMPI detection on a molecular beam. The pulsed valve injects the gas directly to the interaction chamber in a free jet expansion. The laser beam is collimated using a telescope consisting of concave mirrors. A pair of counterpropagating beams is aligned in a Sagnac interferometer using a beamsplitter (BS) and highly reflective mirrors (HR). An auxiliary Nd:YAG laser operating at 355 nm serves to ionize the H_2 molecules excited to the EF state by the first laser.*

by the Kerr effect in the nonlinear upconversion stages; 5.2.7 The integration of the three laser systems (the seed-laser, the pulsed oscillator, and the frequency comb laser) and the on-line chirp detection into a computer-controlled measurement system and the measurement procedures.

5.2.1 Doppler-free 2 + 1-REMPI in a gas jet

A schematic overview of the molecular beam apparatus, including the excitation and time-of-flight (TOF) mass separation and detection zones is shown in Fig. 5.2. Molecular hydrogen is injected into the vacuum using a pulsed valve at a stagnation pressure of 3 bar. The TOF-chamber and the interaction chamber are both differentially pumped to a pressure of 10^{-7} mbar, which rises to about 10^{-6} mbar when the molecular beam is present. Under these conditions, essentially collision-free transition frequencies can be determined.

Although the technique of two-photon spectroscopy employing counter-propagating laser beams is known to be Doppler-free, a slight misalignment from an exact anti-parallel geometry can lead to Doppler shifts. In case of an angular mismatch $\delta \ll 1$, the effective Doppler-shift is:

$$\Delta\nu = \delta \frac{v}{\lambda} \tag{5.1}$$

at the two-photon level, where v is the velocity of the hydrogen molecules and λ the wavelength of the UV light used for two-photon excitation.

In order to minimize calibration uncertainties due to possible Doppler shifts, a collimated laser beam with about 1 mm diameter at the interaction zone was used. Since the UV light output of the laser system is astigmatic, a concave mirror telescope (see Fig. 5.2) is aligned under a certain angle β, making use of the aberration effects on spherical mirrors and thus compensating for the astigmatism. In a first alignment scheme the collimated light was sent to the interaction zone over a distance of 1.5 m, while a plain retro-reflecting mirror placed inside the vacuum on a pivoting mirror mount was aligned such that the counter-propagating beams are overlapped. During the alignment procedure a pinhole of 0.5 mm diameter was placed in the center of the forward directed beam. An overlap accuracy between the counter-propagating beams of about 0.3 mrad is achieved corresponding to a Doppler-shift of about 2.5 MHz at the two-photon energy level. A different, interferometric method has been employed during a later stage of the experiments based on the Sagnac geometry achieving a reproducible angular overlap of better than 0.1 mrad — or 0.8 MHz calibration uncertainty.[28] The stated uncertainty margins for the angular mismatch of the counterpropagating beams contain also an estimated contribution for the fact that the laser beam does not exhibit a perfectly Gaussian beam profile and features possible wavefront distortions.

The REMPI signals were induced either in a single-color (202 nm) excitation, or in a two-color-scheme. In the latter case a strong UV-laser pulse (at 355 nm, the third harmonic of an auxiliary pulsed Nd:YAG laser) serves to ionize the resonantly excited population in the EF-state. In particular for low-energy pulses ($< 10\mu$J) of the resonant laser, the ion signal significantly increases in the two-color scheme. The UV-ionization pulse was delayed by ≈ 50 ns with respect to the excitation laser in order to avoid inducing AC-Stark and population depletion effects.

5.2.2 The deep-UV laser source

For the production of laser light at 202 nm a tunable pulsed laser system at 10 Hz repetition rate is used. A schematic overview is given in Fig. 5.3. A gain-switched (passive) titanium:sapphire (Ti:sapphire) oscillator cavity is pumped by a Nd:YAG laser (Quanta Ray GCR 3). Upon injection seeding with the output of a CW Ti:sapphire ring laser (Coherent 899) at about 808 nm the pulsed oscillator produces a Fourier-limited linewidth at the seed wavelength with a pulse energy of 0.5 mJ. The pulsed oscillator output can optionally be enhanced in a bowtie Ti:sapphire amplifier up to 30 mJ. In order to produce the fourth harmonic at 202 nm, three consecutive nonlinear upconversion stages — BBO crystals cut at appropriate type-I phase matching angles — are used.[39] The pulse energy at 202 nm is varied from zero to maximum output by rotating the polarization of the third harmonic light in front of the fourth harmonic mixing crystal using a $\lambda/2$-waveplate. The laser system reaches maximum output energies of 0.2 mJ/pulse at 202 nm.

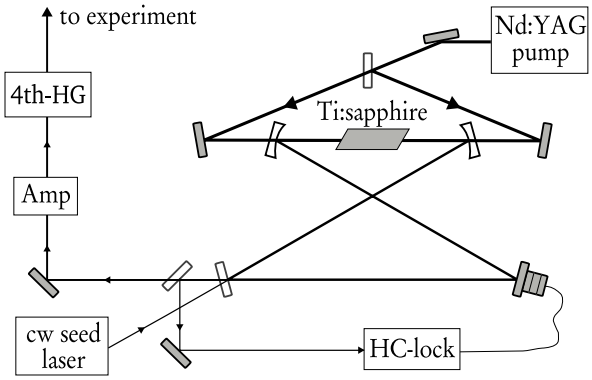

Figure 5.3 – *Schematic layout of the laser system used. The laser resonator contains a Ti:sapphire crystal as single active optical element. The cavity length is locked using Hänsch-Couillaud (HC) scheme.[26] The amplifier system (Amp) is a multi pass Ti:sapphire amplifier in a bow-tie geometry. The 4th harmonic of the near-IR radiation is produced in three consecutive nonlinear crystals. For further details see text and Sneep et al.[39]*

The pulse duration and the bandwidth of the Ti:sapphire pulsed oscillator are found to depend strongly on the pulse energy of the pump laser. Under conditions of optimum power production (at 6 mJ/pulse pump energy, limited by damage of the reflective optics of the resonator) pulse lengths of 20 ns are readily obtained; under these conditions the bandwidth at deep-UV wavelengths, after frequency quadrupling is about 40 MHz as can be estimated from the linewidth of the obtained two-photon resonances. By limiting the pulse energy the pulse duration can be extended to 40 ns. The bandwidth is then also reduced accordingly by a factor of two. In the stage of the experiment where the final calibrations were performed the Ti:sapphire pulsed oscillator was run in this mode delivering the narrowest linewidths.

5.2.3 Absolute calibration procedures

Absolute calibration is performed on the CW seeding light from the Ti:sapphire ring laser. For an absolute calibration with a frequency comb the CW frequency has to be known within a fraction of the frequency spacing of neighboring modes in the comb, which is equal to the repetition rate of the frequency comb, in this case ≈ 75 MHz.[55] At the time, when these measurements where started, the transition frequencies of the EF $^1\Sigma_g^+ \leftarrow$ X $^1\Sigma_g^+(0,0)$ were known[97] to a 1σ accuracy of $0.003\,\mathrm{cm}^{-1}$, which corresponds to 11 MHz accuracy in the infrared domain. In order to avoid any ambiguity on the specific mode, initial calibration experiments were performed with respect to the I_2 saturation standard in the near-infrared. An example of a recording of the Q(0) line in H_2 is shown in Fig. 5.4. The absolute frequency of the Q(0) is found at $99\,164.787(1)\,\mathrm{cm}^{-1}$ — an accuracy of 4 MHz in the infrared — by referencing it to the "t"-hyperfine component of the P(194) line in

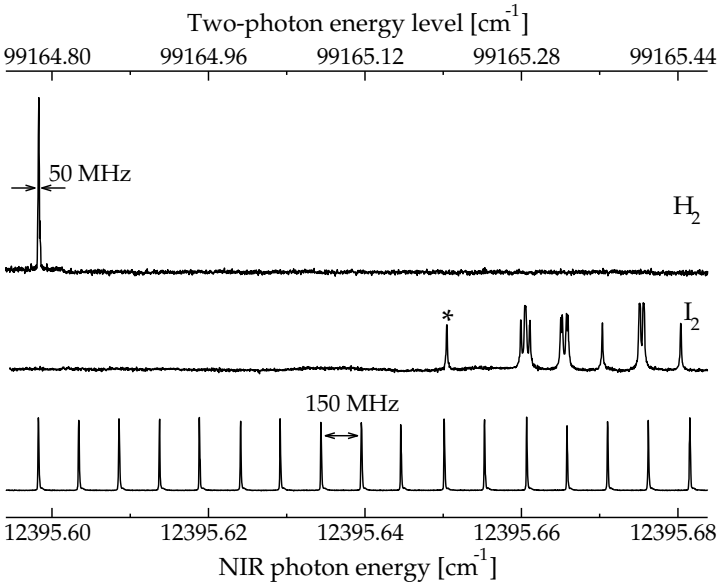

Figure 5.4 – *Simultaneous spectral recording of the $EF\,^1\Sigma_g^+ \leftarrow X\,^1\Sigma_g^+$ (0,0) Q(0) line of H_2 (via the one-color 2 + 1-REMPI scheme), and a saturated I_2 spectrum as well as etalon markers produced at the fundamental wavelength. The line marked with an asterisk is the "t"-hyperfine component of the P(194) line in the $B\,^3\Pi_u^+ - X\,^1\Sigma_g^+$ (0,15) band of I_2 at 12395.65048 cm^{-1}, used as an absolute reference. The indicated linewidth on the H_2 resonance depends on the specific settings on the Ti:sapphire pulsed oscillator (pulse duration and bandwidth) and is given for the two-photon level frequency.*

the $B\,^3\Pi_u^+ - X\,^1\Sigma_g^+$ (0,15) band of I_2 at 12 395.65082 cm^{-1},[101] with inclusion of chirp corrections. According to the discussion of the AC-Stark shift in section 5.2.5, its effect can be estimated to be about 2 MHz at the applied UV power levels for the precalibration. Hence, it can be neglected for the purpose of mode identification.

For the final calibration measurements, part of the CW seed light is coupled through a 100 m single-mode optical fiber for transportation to another laboratory, where a phase and carrier-envelope stabilized femto-second frequency comb laser is installed.[55,57] The CW-light is heterodyned with the output of this frequency comb in a setup as depicted in Fig. 5.5, and the radio-frequency beatnote ν_{bn} is detected on an avalanche photodiode (PD). To increase the signal-to-noise ratio (s/n) on the photo-detector, a grating and lens are used to disperse the spectrum of the frequency-comb in a $4f$-configuration, so that a reduced number of modes is focused together with the CW mode on the PD. Typically, the beatnote detection reached a s/n of 45 db. The two main parameters of the frequency comb are its carrier-envelope phase offset frequency ν_{ceo} and its repetition rate ν_{rep}. Both are locked against a Rubidium-clock standard, which is further referenced to the global positioning system (GPS). From the locking characteristics, the stability of each single frequency

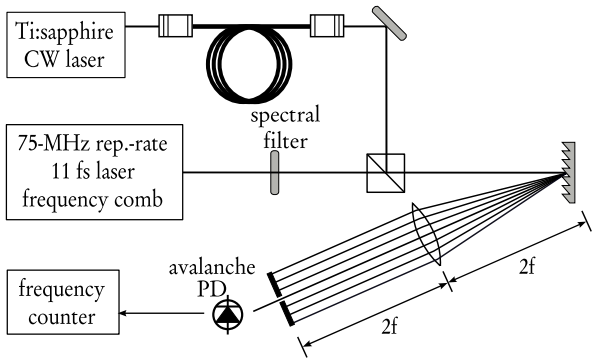

Figure 5.5 – *Schematic view of the setup for the detection of the beatnote with the fs-laser frequency comb.*

of the comb around 808 nm is estimated to be better than 100 kHz for the typical averaging times of 1 s.

The transition frequency ν_Q is measured by determining all radio frequencies involved, via:

$$\nu_Q = \pm\nu_{bn} + \nu_{ceo} + n \times \nu_{rep} \tag{5.2}$$

where the mode number n follows from the initial calibration using the I_2 saturated spectroscopy. The $\pm$ sign of the beatnote frequency ν_{bn} is determined by scanning the cw-laser while monitoring the beatnote between frequency comb and cw-laser. When the cw-laser is scanned to shorter wavelengths and the beatnote increases accordingly the sign is $+$, and when the beatnote decreases the sign is $-$.

The beatnote between the frequency comb and the CW laser is kept at ≈ 22 MHz over the entire scan for convenient electronic filtering. To achieve that, the repetition rate of the frequency comb is correspondingly scanned as the CW laser is tuned over the molecular resonance. The wavelength tuning was sufficiently slow to ensure that the comb mode is correctly identified. In effect, an absolute calibration is performed for every scan step. In Fig. 5.6 the counted beatnotes between seeding light and frequency comb during a typical scan are shown. As pointed out before, the beatnote remains constant at approximately 22 MHz over the entire scan. In order to obtain a result with reasonable statistics, at each scan step the beatnote is counted 10 times. Each single count is acquired within a time gate of 0.1 s, so that the beatnote counting takes 1 s per scan step. The given error bars depicted in the zoomed inlay are taken from the standard deviation of the 10 beatnote frequency countings. Typical standard deviations are 0.5 MHz which is about a factor 5 larger than the stability of the frequency comb (< 100 kHz). The source of the fluctuations of the beatnote is predominantly due to frequency jitter of the seed laser.

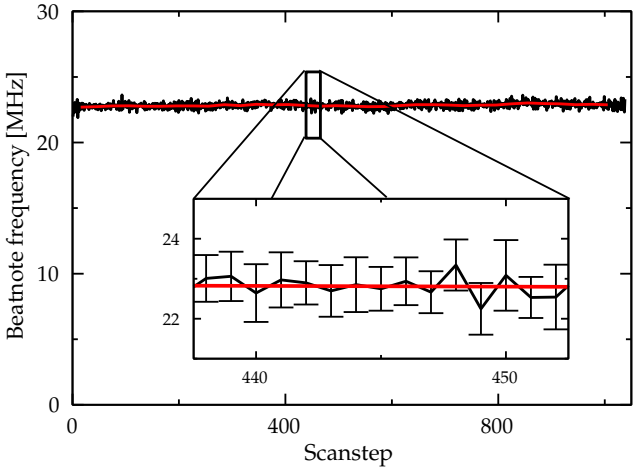

Figure 5.6 – *(color online) Frequency measurements via counting of ν_{bn} for a scan of a thousand frequency steps.*

5.2.4 Frequency-chirp induced offset

Since the spectroscopic experiment on the EF $^1\Sigma_g^+ \leftarrow$ X $^1\Sigma_g^+$ (0,0) transitions is performed with the quadrupled output of the pulsed oscillator, while the frequency calibration procedures are performed on the CW seed-frequency, possible deviations between the two must be considered. Such offsets are common, investigated in detail for traveling-wave dye-amplifiers,[16,18,20] and recently also for optical parametric oscillators.[22,24] In the present case of a pulsed laser oscillator, containing only a Ti:sapphire crystal as an active optical element inside its resonator (see Fig. 5.3), the optical path length will depend on the rate of pumping by the Nd:YAG pump laser; a mode-pulling effect will result from the change in refractive index in the Ti:sapphire crystal during the time interval of population inversion.

This phenomenon is assessed experimentally in two steps. First, a possible net average offset between CW and pulsed output is measured using a confocal etalon in an experimental configuration as shown in Fig. 5.7. Both pulsed and CW beams are overlapped and propagated through a single mode fiber to ensure that they excite a common spatial mode in the etalon. Photodiodes detect fringe traces as in Fig. 5.7 for both the orthogonally polarized signals, when scanning the CW seed-frequency and keeping the etalon at fixed FSR. This procedure results in a quantitative value for the average frequency of the pulsed oscillator: its output is red-shifted by an amount of ≈ 20 MHz with respect to the CW carrier frequency. We note that this method of chirp detection does not allow for a single pulse assessment of this phenomenon, nor does it produce insight into the frequency excursions during the laser pulse. Rather it yields an averaged chirp-induced net shift between CW and pulsed outputs of the laser system.

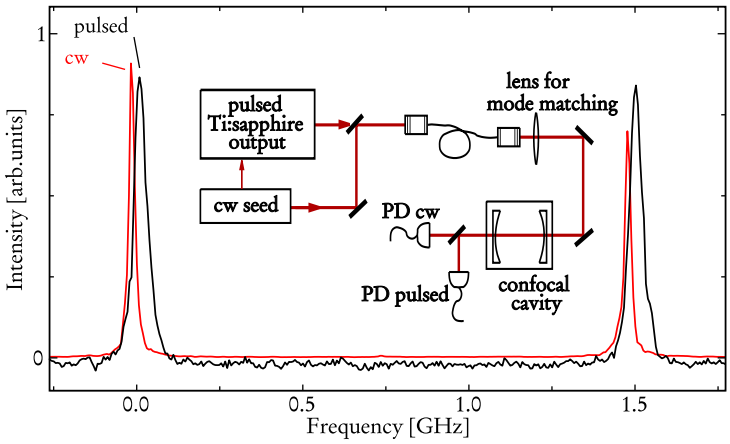

Figure 5.7 – *(color online) Measurement of the net frequency shift between the output of the CW seed laser and that of the pulsed oscillator (for one specific setting of the Hänsch-Couillaud lock on the cavity). As the seed light is tuned the etalon fringes (FSR = 750 MHz) of the pulsed output are red-shifted from the CW-fringes by 20 MHz. The experimental setup is given as an inlay. Both the pulsed and the cw-light are superimposed and mode-matched by transmitting them through a single-mode fiber.*

Secondly, the instantaneous frequency during the temporal evolution of the laser pulse is obtained by heterodyning methods previously described.[18,20,22,24] With the use of an acousto-optical modulator (AOM) a CW-light field shifted in frequency by 250 MHz is generated from the seed light. This frequency shifted light is heterodyned with the pulsed light, and the beatnote is detected on a fast photodiode detector (New Focus DC-1). For maximum beatnote contrast the two light fields must be well overlapped, which is achieved by coupling through a single-mode fiber.

The chirp beatnote is acquired on a fast oscilloscope (Tektronics TDS 7404; bandwidth: 4 GHz, sampling rate: 20 GSample/s) — from now on to be referenced as the "chirp scope" — and used to obtain the temporal evolution of the phase $\Phi(t)$, from which the instantaneous frequency is calculated by:

$$\nu_{\text{chirp}}(t) = \frac{1}{2\pi}\frac{d}{dt}\Phi(t) \tag{5.3}$$

In Fig. 5.8 typical pictures of the various steps in the chirp analysis of an acquired beatnote are shown.

First the beatnote transient $I(t)$ is Fourier-transformed to $\widetilde{I}(\nu)$. In this case the power spectrum (Fig. 5.8c) contains two well separated peaks. The lower frequency peak is a result of the envelope of the beatnote signal, and the higher frequency peak at approximately 250 MHz contains the phase information, which allows for calculating a time dependent change of the instantaneous frequency of the pulse. For extracting the phase information from the beatnote frequency spectrum, the cor-

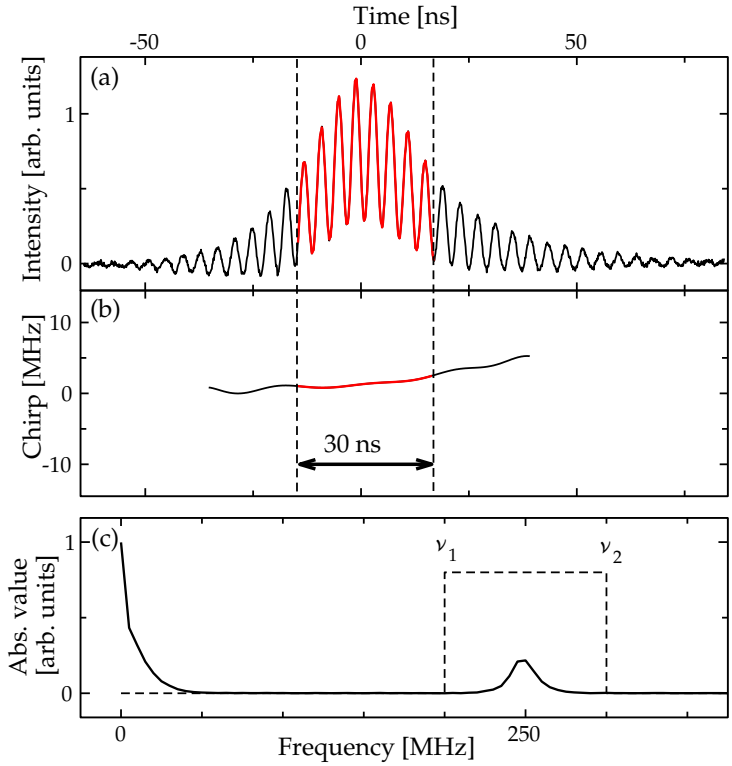

Figure 5.8 – *(color online) From the beatnote (a) a FFT is performed — the lowest graph (c) shows the corresponding power spectrum. Then the result is filtered and inverse Fourier-transformed. From the obtained temporal phase evolution the instantaneous frequency offset is calculated (b).*

responding peak is filtered out by a gate-filter $F(\nu) = \Theta(\nu - \nu_1)\Theta(\nu_2 - \nu)$ — where $\Theta(x)$ is the Heaviside step function — shown in Fig. 5.8c. The imaginary part of the inverse Fourier-transformed filtered spectrum $\widetilde{I}(\nu)F(\nu)$ gives a time dependent phase $\Phi(t)$, from which the phase evolution due to the AOM frequency has to be subtracted. Finally, the instantaneous frequency differences between the CW carrier and the pulsed output are reconstructed using Eq. (5.3). The evolution of the instantaneous frequency of the pulsed light can be described as $\Delta_f(t) = \overline{\Delta}_{f_0} + \Delta_{f_0}(t)$, where $\overline{\Delta}_{f_0} = \overline{f}_{\text{out}} - f_{\text{cw}}$ is called the net pulsed – CW frequency offset and $\Delta_{f_0}(t)$ a time dependent deviation from $\overline{\Delta}_{f_0}$. In Fig. 5.8 — which shows a typical result of the chirp analysis — one can see a shallow slope in $\Delta_f(t)$. The detection and analysis procedures of this dynamic chirp assessment are sufficiently fast to be able to run them online for each individual data point, while performing the hydrogen spectroscopic measurements.

An important finding is that the slope of $\Delta_f(t)$ (*cf.* Fig. 5.8b) can be reduced by lowering the pulse energies to pump the oscillator. Additionally, at low pump en-

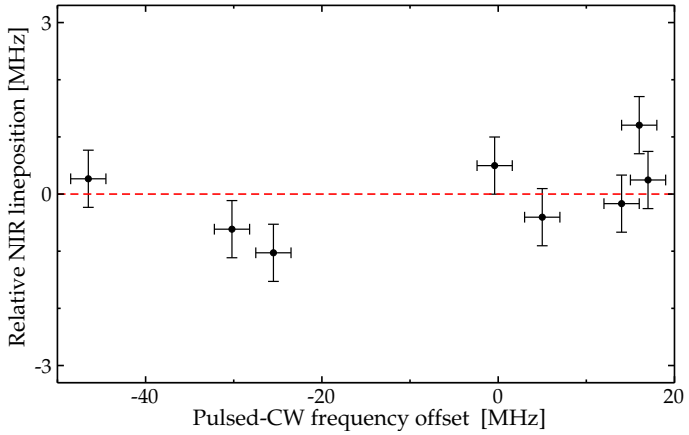

Figure 5.9 – *(color online) Sequence of spectroscopic scans performed on the EF ← X (0,0) Q(1) line in H_2 using different chirp frequency offsets ranging from -50 MHz to 20 MHz. The mean value of all acquired positions for the Q(1) line is 99109.7315 cm^{-1}. The y-axis shows the deviations of the line positions of the single scans from that mean value on the infrared frequency scale (centered at 12388.7165 cm^{-1}). The standard deviation is 0.7 MHz (cf. discussion in section 5.2.4).*

ergy conditions the produced pulses are of longer duration and have a narrower line width. The narrow linewidth and the flat frequency chirp — typically 0 – 2 MHz on 30 ns — are particularly important for producing nearly Fourier-limited harmonics with a well defined frequency and will directly reduce the uncertainty budget on the absolute calibration. The lower pump energy of the pulsed oscillator can be compensated by additional amplification in the multi-pass amplifier system, when working in the saturated regime. It is verified that at the wavelengths used here, the amplifier changes the temporal evolution of the instantaneous frequency of the output pulses only slightly, which means it shifts the net frequency offset by about 2 – 4 MHz. Therefore the chirp analysis is performed on the output of the total infrared laser system so that the effect of the amplifier is always taken into account.

In contrast to changes in the pump power, the settings of the Hänsch-Couillaud feedback loop have only little influence on the chirp slope, but strongly affect the frequency offset $\overline{\Delta}_{f_0}$, which in fact can be tuned to any value in a range from -50 MHz to 20 MHz. This effect is due to cavity mode pulling: the Hänsch-Coulliaud setting changes the cavity length and hence the longitudinal mode structure of the cavity. As a result the pulsed output is pulled from the seeding frequency towards the closest cavity resonance. In order to check, whether the chirp analysis performs consistently, the EF ← X Q(1) line in H_2 was measured at different chirp offset frequency settings. If the chirp analysis is properly behaved, the transition frequency of the Q(1)-line should be independent of the chirp offset. In Fig. 5.9 the result of a series of scans over the resonance is shown. Each scan obtained at different Hänsch-Couillaud settings. For the resulting different frequency offsets, the

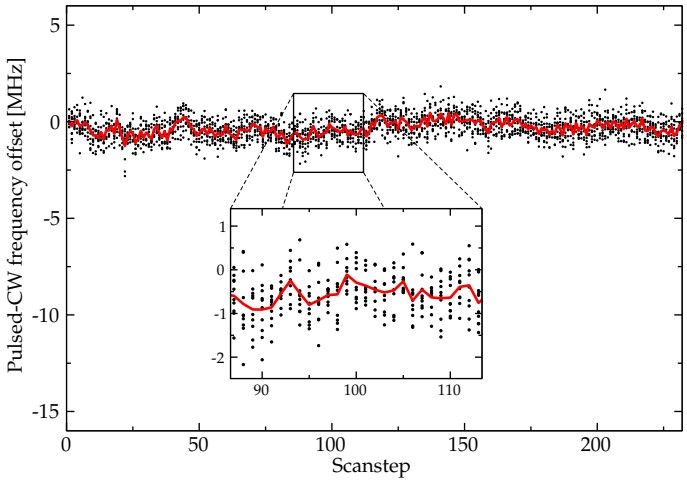

Figure 5.10 – *(color online) Online chirp analysis for a scan covering ≈ 260 seconds at 10 Hz of data for a specific setting of the pump energy for the Ti:sapphire oscillator. The locking point of the Hänsch-Couillaud feedback system was set such that the net shift $\overline{\Delta}_{f_0}$ equals zero.*

fitted transition frequencies are spread around 99109.7315 cm^{-1} with a standard deviation of 5.6 MHz. Correspondingly, the actual Ti:sapphire frequencies vary around 12388.7165 cm^{-1} with a standard deviation of 0.7 MHz. It should be noted, that both the spread and the mean line position for Fig. 5.9 are acquired using earlier, preliminary alignment and ionization methods, which where replaced by more accurate procedures afterwards — a Sagnac interferometer replaced a simple retroreflection on a plain mirror and a two-color REMPI replaced a one color scheme. Correspondingly, the spread in Fig. 5.9 is a combination of several statistical errors being larger than listed in Table 5.2. It includes larger Doppler uncertainties, larger AC-Stark influences, and more pronounced chirp influences than the ones achieved using the newer methods.

Though the check in Fig. 5.9 shows, that the actual frequency offset between pulsed and seed light does not affect the final result, the settings were selected such that the offset frequency remains about zero during a scan. In a forthcoming publication the characteristics of the pulsed laser are investigated in greater detail. It appears, that the zero-offset setting is also the most efficient for the energy conversion from the cavity pump to the Ti:sapphire near infrared output. That in turn allows for a further reduction of the pump energy, and consequently a reduction of the chirp. In Fig. 5.10 the obtained chirp-induced frequency offsets during one spectroscopic scan are displayed for a specific setting of the pump energy for the pulsed oscillator and the Hänsch-Couillaud locking point. The frequency offset is acquired for 10 pulses per scan step. From those 10 values per scanstep the mean values are calculated and shown as a solid line in the figure.

For the measurements displayed in Fig. 5.10 the Hänsch-Couillaud locking was set such that a net shift of $\overline{\Delta}_{f_0}$ is zero. This is a different setting than used for the data displayed in Fig. 5.7. It was verified however that the obtained mean values of about -15 MHz to -20 MHz obtained with the etalon method are consistent with the dynamic chirp measurements. The negative sign indicates, that the pulsed output has a smaller frequency than the seeding light. The chirp analysis gives information on the relative frequency jitter between seeding light and pulsed output of the Ti:sapphire oscillator.

5.2.5 DC and AC-Stark effects

In order to prevent DC-Stark effects shifting the transition frequency, laser excitation is performed under field-free conditions, while a pulsed extraction voltage ramp (1000 V) is switched 0.3 μs after the excitation to collect the ions produced via 2 + 1-REMPI. For the $n = 2$ EF state in hydrogen possible stray electric fields at the level below 0.1 V do not affect the transition frequency at the present level of accuracy.

In order to assess the influence of the AC-Stark shift, the output energy of the laser was varied. Finally, the result on each transition frequency is retrieved from an extrapolation to zero pulse energy as shown in Fig. 5.11. Note that the AC-Stark effect parameter exhibits a different value for each transition. The absolute value for the AC-Stark shift parameter, being 7 MHz/(MW/cm^2) for the Q(0) line in HD, can be determined to within an accuracy of not better than 50 % in view of the uncertainties in the measurement of UV pulse energy and the size of the laser beam. The obtained values for the AC-Stark shift parameters are listed in Table 5.1. The present value for the AC-Stark parameter pertaining to the Q(1) line of H_2 is in reasonable agreement with that of Vrakking *et al.*,[102] who found 15 MHz/(MW/cm^2).

For the determination of AC-Stark free transition frequencies the extrapolations to zero intensities are relevant, irrespective of the absolute pulse intensity scale. In a first round of experiments the absolute transition frequencies of most of the lines were determined from such extrapolations of the measured frequencies in the one-color 2 + 1-REMPI scheme. A general result from the entire set of measurements on the assessment of the AC-Stark effect is that at the lowest laser intensities, corresponding to pulse energies ($< 4\mu$J the AC-Stark shifts are lower than 1 MHz. Hence a second round of measurements was performed on all lines in H_2, HD and D_2 in which the excitation laser was kept below 4μJ/pulse, and where the ionization was accomplished by a second intense UV-laser pulse (at 355 nm) that was temporally delayed by ≈ 50 ns. In this two-color REMPI scheme AC-Stark free measurements were performed resulting in the most accurate values for the transition frequencies. It was verified that the data of the extrapolated one-color experiments are consistent with those of the two-color pulse-delayed scheme.

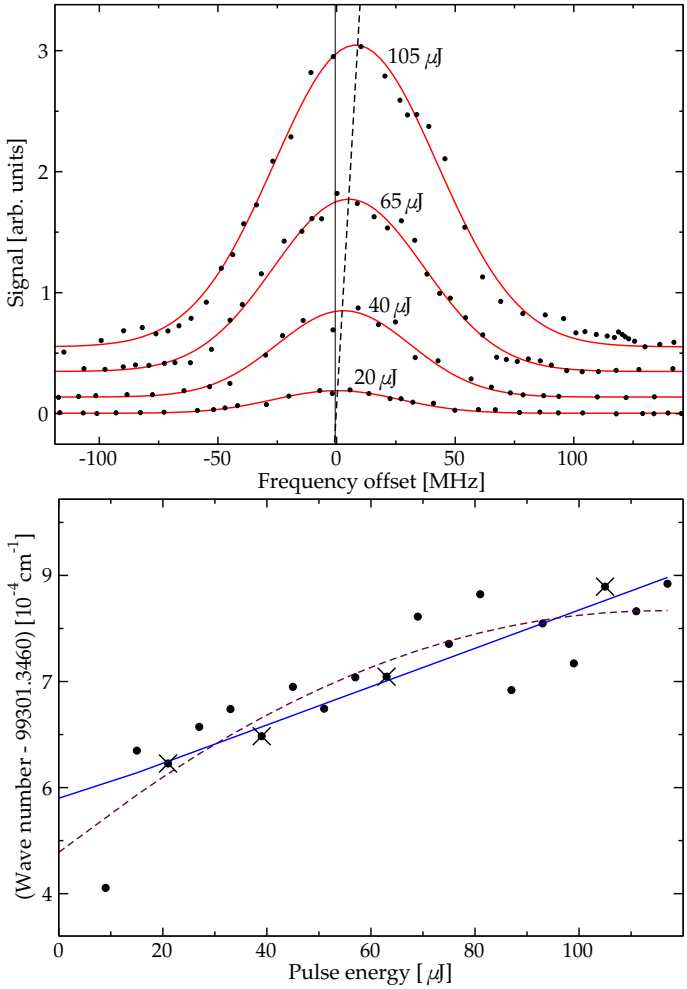

Figure 5.11 – *(color online) Assessment of the AC-Stark effect on the EF* $^1\Sigma_g^+ \leftarrow X\,^1\Sigma_g^+$ *(0,0) Q(0) line in HD by measurement of the transition frequency as a function of laser pulse energy with parameters: pulse length 12 ns (at 202 nm) and collimated beam diameter 0.04 cm. The upper graph shows data obtained at four different pulse energies for the deep-UV excitation laser, here used in the 2+1 one-color REMPI scheme. The line positions found for different data traces in the upper graph are marked with an X in the lower graph. Extrapolation by linear regression to the intercept yields a value of 99 301.34654(6) cm*$^{-1}$ *for this specific measurements series and a value for the AC-Stark shift of 7 MHz/(MW/cm*^{2}*). A quadratic regression (dashed line) leads to an intercept of 99 301.34646(6) cm*$^{-1}$*.*

Table 5.1 – *Measured AC-Stark shifts on various EF $^1\Sigma_g^+ \leftarrow X\,^1\Sigma_g^+$ (0,0)-transitions in H_2 and HD given in MHz/(MW/cm^2).*

molecule	line	AC-Stark shift
H_2	Q(0)	13(7)
	Q(1)	6(4)
HD	Q(0)	5(3)
	Q(1)	6(3)

5.2.6 Phase distortions in non-linear mixing

Additional effects of frequency chirp can be induced as a result of optical phase distortions in the processes of nonlinear mixing for the generation of harmonics. These issues and the consequences for frequency metrology on the basis of pulsed laser sources were discussed in detail by Gangopadhyay *et al.*[17] Firstly, the optical Kerr effect, modulating the index of refraction $n(t)$ with the laser intensity $I(t)$ during the pulse evolution via : $n(t) = n_0 + n_{\mathrm{Kerr}} I(t)$, may give rise to phase distortions of the size[17,103]:

$$\Phi(t) = -\frac{2\pi L\, n_{\mathrm{Kerr}}\, I(t)}{\lambda}, \tag{5.4}$$

where L is the length of the non-linear crystal, λ the wavelength, and n_{Kerr} the wavelength-dependent Kerr index for the used crystal.

The resulting chirp may be evaluated via Eq. (5.3). The Kerr index of BBO has been measured by Li *et al.*[104] at 1064 nm and 532 nm at different crystal axes. The obtained values vary between $4 \cdot 10^{-16}$ cm^2/W and $5 \cdot 10^{-16}$ cm^2/W and are given with a 20 % error margin. For the moment, the analysis is restricted to the Kerr effects induced in the stage of the second harmonic generation (SHG). In Fig. 5.12 an example for typically used infrared pulse intensities of 0.2 GW/cm^2 in the SHG crystal is calculated. For obtaining the temporal intensity profile $I(t)$, shown in Fig. 5.12(b), the normalized signal of a fast photodiode (Thorlabs DET 210) with a response time of 1 ns was used. Using the chirp analysis system the corresponding instantaneous frequency evolution $\nu_{\mathrm{offs}}(t)$ in the SHG crystal was acquired — displayed in Fig. 5.12(a). From the calculation using Eq. (5.4) inserted into Eq. (5.3) it is apparent that the Kerr effect modulates the instantaneous frequency ν_{result} in an antisymmetric way around the maximum of $I(t)$. At the rising side the instantaneous pulse frequency is shifted to higher frequencies and the at the falling side to negative frequencies. Possible deviations from a perfect antisymmetric behaviour resulting from an asymmetric temporal pulse profile $I(t)$ could produce net frequency shifts affecting the absolute calibration. Based on a simulation the net frequency shift $\overline{\Delta}_{f_0}$ was calculated both with and without the Kerr effect. As a result of the nearly antisymmetric evolution of $\nu_{\mathrm{Kerr}}(t)$, the difference between the two net shifts proved to be insignificant, as

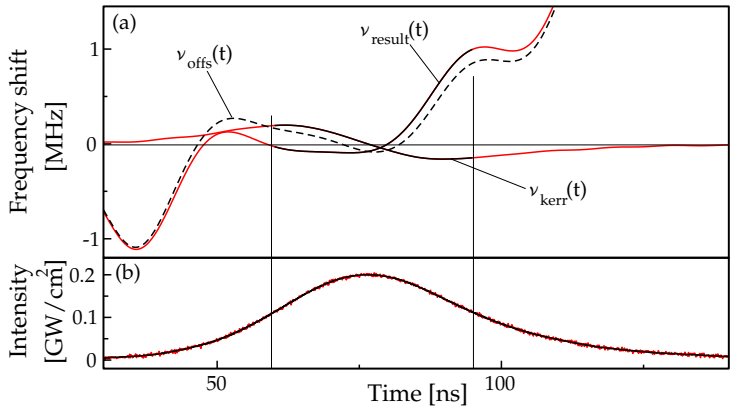

Figure 5.12 – *(color online) The influence of the Kerr effect on the instantaneous frequency evolution in the SHG crystal calculated for a typical infrared pulse of 0.2 GW/cm² peak intensity and 35 ns duration.* ν_{offs} *: pulsed – CW frequency offset measured in front of the SHG crystal,* ν_{kerr} *: instantaneous frequency shift caused by the Kerr effect,* ν_{result} *: the sum of* ν_{offs} *and* ν_{kerr}*.*

the net Kerr shift is several orders of magnitude below the uncertainties of the chirp analysis of section 5.2.4.

Since the instantaneous effect of Kerr induced phase distortions is quasi-antisymmetric over the temporal profile of the pulse — also for the subsequent stages of third and fourth harmonic generation — their net effect on the frequency calibration is far below other sources of calibration uncertainties. In principle, at the following sum frequency mixing stages, the Kerr effect could indeed cause frequency shifts, when a time delay between the two contributing input beams was introduced. However with typical pulse lengths of 20 ns as used here, careful alignment of the lengths of the beam branches in the upconversion stages prevents such problems efficiently.

A second phenomenon resulting in chirp from phase distortions in non-linear mixing is associated with a deviation from optimum phase-matching.[17,105] We decided to assess the effects of non-perfect phase-matching via an experimental approach. The entire optical layout, in particular involving the alignment of the beam propagation and the adjustment of the phase-matching angles, was set up from scratch in a number of separated measurement days focusing on a few transitions. After the complete daily realignment procedure both the phase-matching angles of the upconversion crystals and the dark fringe at the exit port of the Sagnac interferometer were readjusted for each single scan. During those procedures indeed statistical day-to-day excursions in the determined transition frequencies were obtained with a standard deviation of about 2.5 – 6 MHz depending on the isotopic species and particular line; these excursions are somewhat larger than the 1σ spread of results obtained during a measurement series of one day, which was limited to 2 – 3 MHz. These excursions are attributed to the combined effect of Doppler shifts, phase distortions in non-linear mixing, day-to-day beamprofile variations, and vary-

ing wavefront distortions. Particular the latter two effects are more dependent on the daily full realignment of the optical layout.

5.2.7 Integrated setup and measurement procedures

The three different laser systems, the CW Ti:sapphire seed laser and the Ti:sapphire pulsed oscillator-amplifier system in one laboratory, and the frequency comb lasers in another laboratory separated by 100 m, and the vacuum and detection equipment are assembled into one experiment of which a schematic overview is shown in Fig. 5.13. In laser-lab-I, where the spectroscopic data are recorded, master computer PC1 takes control of all tasks during the experiment. The frequency of the seed laser is driven, via its external voltage scan port, by an arbitrary waveform generator (Agilent AWG 33250A) connected via GPIB to PC1. The "chirp scope" is triggered by a photodiode detecting the 202 nm light. The sample beatnote waveforms (as in Fig. 5.8) are transferred via GPIB to PC1, where the chirp analysis is carried out. Finally, the REMPI-TOF signal is registered on an electron multiplier tube and digitally integrated using a LeCroy WaveRunner oscilloscope (the "TOF scope"). The "TOF scope" is triggered by the external trigger interface of the "chirp scope". This combined trigger acquisition ensures that all possible data is acquired from each pulse following the 10 Hz repetition rate of the laser: the chirp parameters, the relative UV power and the REMPI signal. This pulse-correlated acquisition allows for using binning and filtering techniques for data analysis, of which some are performed off-line. By this means correlations between power fluctuations of the pump laser, the chirp/frequency-pulling characteristics, and the UV output power can be investigated. Also, the AC-Stark induced frequency shifts resulting from UV-power fluctuations can be used to derive the AC-Stark parameter.

In the femto-lab (*cf.* Fig. 5.13), where the frequency comb is operated, PC2 is responsible for the frequency comb laser control and data acquisition. The beatnote signal detected on the avalanche photodiode (Fig. 5.5) is filtered via an RF-band pass filter to remove signal from higher order beatnotes, amplified, processed via a discriminator and counted on a frequency counter (Agilent 53132A Universal Counter) connected to PC2 via GPIB. The repetition rate of the frequency comb — actually its 140th harmonic — is locked to a frequency of about 10 GHz. This frequency is generated by a radio frequency synthesizer (Agilent PSG-L F8241A), which is locked to a Rubidium clock standard. The set frequency of the synthesizer is controlled by PC2 via GPIB bus. In order to maintain synchronous operation in the two labs PC2 stays in connection with PC1 via a server-client protocol running on top of the ethernet. PC2 initiates beatnote counting on PC1's request. Furthermore PC2, depending on the actual beatnote readout, adjusts the repetition rate of the frequency comb in order to maintain the beatnote within a frequency window of 21 MHz – 24 MHz which is the working range of the final low-pass filter in front of the frequency counter.

The wavelength of the seed light is continuously monitored by an ATOS LM 007 wavemeter and sent to PC1 through a RS 232 serial connection. Although its long-

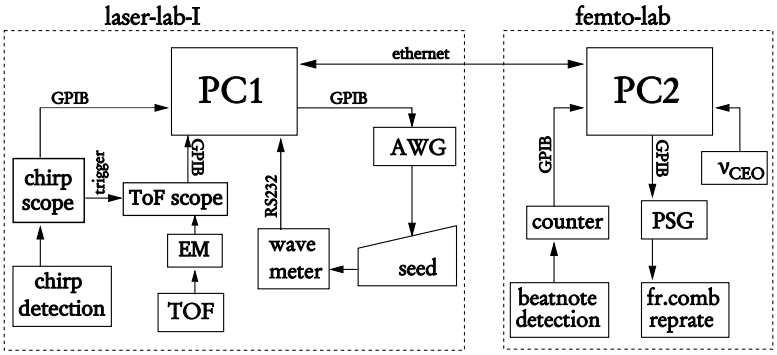

Figure 5.13 – *Flow control scheme and overview of the experimental components. PC1 is the master system, taking control of the laser scan and requesting data from frequency comb server PC2 in the femto-lab. PC2 initiates the beatnote counts, but also maintains the beatnote within a frequency window by controlling the repetition rate of the comb. AWG: arbitrary waveform generator. DAC: GPIB signal acquisition interface. PSG: signal generator.* ν_{ceo}*: the carrier envelope offset frequency is read via GPIB from the wave form generator that provides the reference signal for the corresponding feedback loop.*

term stability is about 30 MHz in the near infrared, during the time-span of an experiment it remains reproducible to within 3 MHz. This auxiliary instrument is used for pre-calibration, for detection of possible mode-hops of the CW seed laser, and for establishing the sign of the beatnote frequency between frequency comb and seed light.

The experimental procedure is as follows: After the precalibration is finished using iodine saturation spectroscopy (*cf.* Fig. 5.4) the actual frequency comb measurement is performed. First the seed laser is tuned to the start frequency which is chosen roughly 30 MHz next to the two-photon resonance. Then the repetition rate of the frequency comb is set such that the beat note frequency between seed and frequency comb is 22 ± 2 MHz (within the accepted range of the band pass filter in use). Furthermore the sign of the beatnote frequency must be established. Then the scan is started: using the AWG connected to PC1 the laser is scanned with a fixed voltage step per scan step. On each scan step the beatnote frequency between seed and frequency comb is counted. If the frequency comb would run at fixed settings and no band pass filter was used — depending on the sign of the beatnote frequency — the beatnote frequency would increase until reaching half the repetition rate ν_{rep} and decrease again, or it would decrease until a zero beatnote is reached and then increase again. In order to avoid inevitable assignment problems at beat note frequencies close to zero or $\nu_{\mathrm{rep}}/2$, the beatnote is quasi-locked around the start value. This is achieved by steadily adjusting ν_{rep} at each scan step after finishing the beatnote frequency counting.

Each scan covers a range of about 70 MHz (in the near infrared) and consists of

Table 5.2 – *(A) Estimated systematical error budget for the frequency calibrations of the EF $^1\Sigma_g^+$ ← X $^1\Sigma_g^+$ (0,0)-transitions in hydrogen. (B) The experimentally obtained statistical spread listed for each line.*

(A)	Systematics	Detail		Value (MHz)
(*i*)	Doppler	H_2		0.75
		HD		0.6
		D_2		0.5
(*ii*)	Calibration	Frequency comb		< 0.1
(*iii*)	Chirp	In Ti:sapphire oscillator		2
(*iv*)	Chirp	In nonlinear mixing		< 0.01
(*v*)	AC Stark	In two-color scheme		< 1.0
Estimated systematical error budget[a]				3.2
(B)	Statistics[b]	H_2	Q(0),Q(2)	3.3
		H_2	Q(1)	5.4
		HD	Q(0),Q(1)	6.0
		D_2	Q(0),Q(1)	2.4
		D_2	Q(2)	2.1

[a] Quadrature summation of errors (*i*-*iv*) and adding (*v*) linearly to the result.
[b] (1σ) standard deviation of all results (10 to 15 scans per line) obtained over several days.

about 300 equidistant voltage steps. On each step PC1 first requests PC2 to start the beatnote frequency counting in the femto-lab. Then the "chirp scope" and "TOF scope" are triggered ten times so that the data of ten pulses are obtained. After that PC1 requests PC2 to send all relevant data from the frequency comb, ν_{rep}, ν_{ceo} and ν_{bn}. The software written on both computers is based on the Python programming language. The mathematically more involved part of the chirp analysis is written using the SciPy [106] package.

5.2.8 Uncertainty budget for the transition frequencies

In this section, the final contributions to the uncertainty budget for the present calibration study on EF $^1\Sigma_g^+$ ← X $^1\Sigma_g^+$ (0,0) lines are compiled. The estimated values, discussed extensively in the previous subsections are listed in Table 5.2. The major contributions are associated with the chirp characteristics of the pulsed oscillator — documented in section 5.2.4 — and with the non-perfect overlap of the two counter-propagating laser beams pumping the two-photon resonance. In the present experiment an almost negligible uncertainty is associated with the absolute frequency scale by using a frequency comb laser. The estimate on the AC-Stark effect pertains to the two-color 2 + 1-REMPI scheme, in which pulse energies of less than 4 μJ are used for

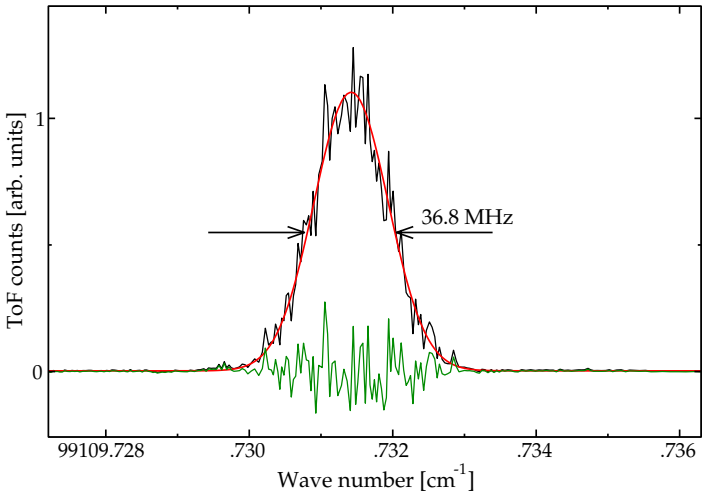

Figure 5.14 – *(color online) Scan on the EF* $^1\Sigma_g^+ \leftarrow X\,^1\Sigma_g^+$ *(0,0) Q(1) line in* H_2*. This spectrum was recorded under low pulse energy pumping conditions for the Ti:sapphire pulsed oscillator delivering the narrowest bandwidth output. Each data point represents an average over 10 shots. The line width obtained in this spectrum is 36.8 MHz. The smooth line corresponds to a Gaussian function fitted to the observed spectral data; residuals are shown as well.*

the two-photon excitation. The resulting final estimate for the uncertainty of a transition frequency, including all systematics is evaluated at 3.2 MHz. The statistical spread (1σ) in the data for measurements recorded under identical conditions on the same day is limited to 2 MHz for H_2 and D_2 and to 3 MHz for HD — for the latter lower beam densities were applied yielding lower s/n ratios. These uncertainties are consistent with the final systematic estimate as listed in Table 5.2 A. However, the spread (1σ) over varying conditions of several days measurements can be as large as 5.4 MHz for H_2 Q(1) and 6 MHz for HD (*cf.* Table 5.2 B), but is smaller in other cases. We do not know the exact origin of these somewhat larger variations. Since the known sources of systematic uncertainties lead to a smaller value, the day-to-day variations are treated as statistical uncertainties. In the final listing of the transition frequencies in Table 5.3, the estimated systematical error budget of 3.2 MHz or 0.00011 cm^{-1} (Table 5.2 A) is considered as lower uncertainty limit.

One possible contribution to statistical variation not discussed so far is the nonlinear curve fitting for obtaining the line positions. In the present study, we have not elaborated on line shape models, because all spectral lines, recorded at low intensity, could be fitted to purely Gaussian line profiles. A typical example of a recorded line is shown in Fig. 5.14. Each scan consists of about 2000 to 3000 data points and spans about 300 MHz at the two photon level. The obtained fitting uncertainties for the line center positions are about 0.4 MHz for each single scan and all measured lines, which is to small to explain the discrepancy between estimated error budget and

experimentally observed spread.

5.3 Results and conclusions

The present study involves a highly accurate frequency measurement of eight spectral lines in the $EF\,^1\Sigma_g^+ \leftarrow X\,^1\Sigma_g^+(0,0)$ band of H_2, HD, and D_2 by Doppler-free two-photon excitation in the collision-free conditions of a molecular beam. As a typical example, in Fig. 5.14 a scan over the Q(1) line in H_2 under conditions of a narrowband excitation pulse in the two-color 2 + 1-REMPI scheme is shown. Resulting values for the transition frequencies are listed in Table 5.3. Values for the AC-Stark shift were derived and are given in Table 5.1. In the two-color REMPI scheme the AC-Stark effect was reduced to a sub-MHz level. An absolute accuracy of 2×10^{-9} on the transition frequencies is achieved, thanks to the implementation of several new technologies. A pulsed Ti:sapphire oscillator laser was designed to produce Fourier-transform limited narrowband pulses of which the chirp was measured on-line at high precision. For the first time a frequency comb, referenced to a Rb-atomic clock and to the GPS, was implemented in a spectroscopic measurement chain for calibrating chirp-controlled nanosecond pulses.

Table 5.3 – *The two-photon energy values in various hydrogen isotopomers for $EF\,^1\Sigma_g^+ \leftarrow X\,^1\Sigma_g^+$ (0,0)-transitions and a comparison with results by Yiannopoulou et al.[100] Δ represents the deviation between presently obtained values and those of Yiannopoulou et al.[100] The numbers given in parentheses in column "this work" are the final estimates of the uncertainty as discussed in section 5.2.8. All values in cm^{-1}.*

species	line	this work	Ref. [100]	Δ
H_2	Q(0)	99164.78691(11)	99164.7871(8)	−0.0002
	Q(1)	99109.73139(18)	99109.7316(8)	−0.0002
	Q(2)	99000.18301(11)		
HD	Q(0)	99301.34662(20)	99301.3461(8)	+0.0005
	Q(1)	99259.91793(20)	99259.9184(8)	−0.0005
D_2	Q(0)	99461.44908(11)	99461.4490(8)	+0.0001
	Q(1)	99433.71638(11)	99433.7166(8)	−0.0002
	Q(2)	99378.39352(11)	99378.3937(8)	−0.0002

The present results are in excellent agreement with a previous set of measurements on the same lines, performed at the 8×10^{-9} accuracy level. It is important to note that the study of Yiannopoulou *et al.*[100] involves an entirely different setup and measurement procedures. Hence it is more than comforting that the deviations between the two experiments are much less than expected based on the quoted uncertainties. The combined results of the present study and those of Yiannopoulou

et al.[100] form an essential ingredient for a future determination of a value of the ionization potential in H_2 and the other hydrogen isotopomers at an accuracy of $0.001\,cm^{-1}$.

Acknowledgment

We thank Dr. Knöckel (Hannover) for lending us a cell to perform I_2 saturation spectroscopy in the near-infrared region, and Dr. E. E. Eyler (Connecticut) for discussing results obtained by his group prior to publication. The Netherlands Foundation for Fundamental Research on Matter (FOM) is gratefully acknowledged for financial support.

Chapter 6

Noncollinear resonance enhanced four wave mixing

Fourier-transform (FT) limited extreme ultraviolet radiation (XUV) (bandwidth $\lessapprox 300\,MHz$) tunable around 91 nm is produced using two-photon resonance enhanced four-wave mixing on the Kr resonance at 94093 cm^{-1}. Non-collinear phase-matching ensures the generation of a XUV sum frequency $2\omega_1 + \omega_2$ that can be filtered from auxiliary laser beams and harmonics by an adjustable slit. Application of the generated XUV light is demonstrated in spectroscopic investigations of highly excited states in H_2 and N_2.

This chapter is published in Optics Letters **30**, 1494-1496 (2005).

6.1 Introduction

Nonlinear optical schemes for the production of narrowband and tunable extreme ultraviolet (XUV) radiation, either through third-order harmonic conversion, or through resonant sum and difference frequency mixing, date back to the 1970s and 1980s. A description of phase-matching and properties of the $\chi^{(3)}$ nonlinear susceptibility tensor was given by Bjorklund.[107] While Wallenstein and coworkers performed pioneering studies of the resonance enhancement effect by two-photon transitions in noble gases,[108] later it was found that the $4p^6 \rightarrow 4p^5 5p[1/2]_0$ transition in Kr gas is most effective in enhancing the XUV yield.[109,110] The replacement of grating-based pulsed lasers by Fourier-transform limited lasers, generally in the form of pulsed-dye amplifiers (PDAs) opened the possibility of generating ultranarrowband XUV radiation [111,112] even at wavelengths as short as 58 nm.[20] In applications where the generated XUV beam needs to be separated from the incident laser beams, as well as from the auxiliary harmonic and mixed frequencies, usually a grating is employed, with the drawback of intensity loss by an order of magnitude or more. Here we demonstrate that phase-matching in a non-collinear beam configuration can combine the advantage of resonance enhancement with the production of a separated XUV beam, filtered geometrically by inserting an adjustable slit. The

scheme is somewhat similar to that of "BOXCARS", applied for geometrical filtering a generated beam in coherent anti-Stokes Raman spectroscopy.[113]

6.2 Experimental Setup

All measurements are performed in a three-chamber differentially pumped vacuum setup which has been described in connection to third harmonic generation[114] and fifth harmonic generation.[20] Here, tunable XUV light is produced by mixing the output of two different lasers in a pulsed jet of krypton. One provides the resonant light ω_1 for the Kr $4p^6 \rightarrow 4p^5 5p[1/2]_0$ two-photon transition at 94093 cm^{-1}, the other supplies the tunable component ω_2 in a resonance enhanced four-wave mixing scheme. For all results presented, the sum-frequency $2\omega_1 + \omega_2$ is used, while the repetition rate is 10 Hz. In order to filter out undesired wavelengths a simple geometric scheme is applied as depicted in Fig. 6.1. By aligning the resonant light

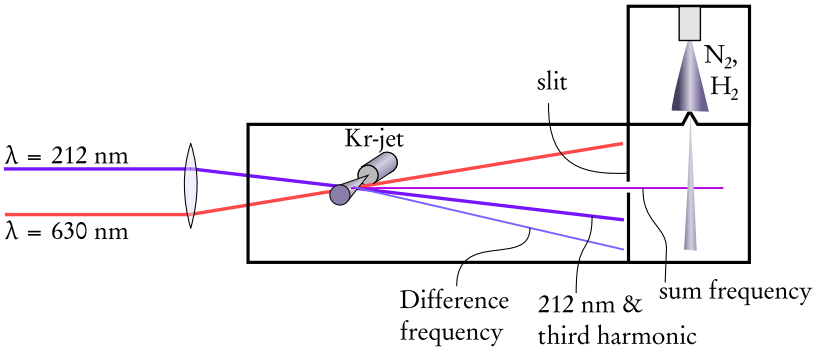

Figure 6.1 – *(color online) Schematic view on the beam alignment and the resulting directions for the different VUV wavelengths. ω_1: resonant light at 212 nm, ω_2: tunable light from PDA. In the Kr gas jet the sum frequency $2\omega_1+\omega_2$, difference frequency $2\omega_1-\omega_2$ and the third harmonic $3\omega_1$ are produced. The slit, adjustable in position and width, filters the XUV beam at frequency $2\omega_1+\omega_2$.*

ω_1 at 212 nm and the tunable output ω_2 of the second laser to overlap in the Kr-jet at an angle of about 80 mrad, phase-matching conditions for the sum-frequency $2\omega_1 + \omega_2$, the difference-frequency $2\omega_1 - \omega_2$, and the third harmonic $3\omega_1$ are fulfilled at angles as displayed in Fig. 6.1. This geometry allows for blocking all unwanted wavelengths by a slit, which is adjustable in width and position and located between the frequency mixing chamber and the downstream application zone.

For the production of the resonant light at 212 nm a novel narrow-band laser system, as schematically shown in Fig. 6.2, is used. A gain-switched injection seeded titanium:sapphire (Ti:sapphire) oscillator, pumped by the second harmonic output of a Q-switched Nd:YAG laser (Spectra Physics Quanta Ray GCR-3), produces nearly FT-limited pulses at wavelength $\lambda = 850.222$ nm with a typical duration of 15 ns and bandwidth 40 MHz. The output of the pulsed oscillator is subsequently enhanced to

15 mJ in a bow-tie Ti:sapphire amplifier and nonlinearly upconverted by two consecutive type-I second harmonic generation stages, made from β-barium borate (BBO) crystals cut at appropriate phase-matching angles. The final output at 212 nm is typically 0.5 mJ with a bandwidth of 80 MHz. The injection seeding light is provided

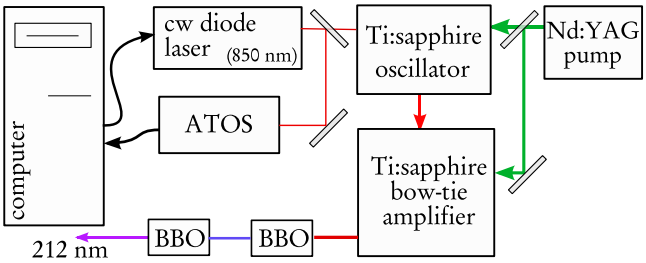

Figure 6.2 – *(color online) The laser setup for the resonant light at 212 nm. In a computer controlled feedback loop the diode injection seed is locked to a preset value of an ATOS λ-meter.*

by an external grating diode laser system (Toptica DL 100). The output frequency of the diode laser is locked using a computer controlled feedback loop. The computer continuously acquires the wavelength of the seed light from an ATOS λ-meter and controls the output wavelength of the diode laser by adjusting the angle of the feedback grating using a piezo actuator. The accuracy of this locking scheme is limited by the accuracy of the λ-meter, which is 0.002 cm^{-1} in the near-infrared. Since the fourth harmonic ω_1 is used to drive the two-photon transition in Kr, the error multiplies by 8 to 0.016 cm^{-1} in the XUV. It should be noted that under conditions of $f = 25$ cm focusing of the ω_1 beam the two-photon resonance in Kr broadens to about 1 cm^{-1}. In view of the small bandwidth of the ω_1 laser (≈ 0.003 cm^{-1} at 212 nm), the resulting XUV frequency and bandwidth are determined by the frequency and bandwidth of the laser, and not by the resonance.

The tunable frequency ω_2 in the wavelength range 630 nm to 650 nm is provided by a PDA consisting of three amplification stages pumped by the second harmonic output of a Q-switched Nd:YAG laser (Spectra Physics GCR-4), and delivering ≈ 20 mJ/pulse. The cw seeding light is generated by a ring-dye laser (Spectra Physics 380) running on DCM, and pumped by the second harmonic of a diode pumped Nd:YVO_4 laser (Spectra Physics Millenia X). Absolute frequency calibration of the PDA (bandwidth ≈ 100 MHz) is realized via iodine saturation spectroscopy and a stabilized etalon yielding an accuracy in ω_2 (including frequency chirp effects in the PDA) better than 0.001 cm^{-1}. The intensity of the XUV output was not measured directly. From measurements of signal strengths in photoionization studies (see below) and comparison with previous detection schemes using third harmonic generation (THG),[114–116] photon densities in excess of 10^9 photons per pulse are estimated.

To demonstrate the capabilities of the source the tunable narrowband XUV radiation is applied in crossed-molecular and laser-beam spectroscopic experiments on

highly excited states in H_2 and N_2. Spectral lines are recorded by tuning the XUV source into resonance with an excited state of the molecule, which is then subsequently ionized (a $1+1'$ photoionization scheme) by an auxiliary laser beam — here the residual second harmonic of the Ti:sapphire laser at 425 nm is applied — incident from the rear side of the interaction chamber. The signal is monitored by detection of ions on an electron multiplier, after pulsed-field extraction, time-of-flight mass separation, and time-gating of the ions produced in photoionization. Doppler effects (broadening and shifts) are reduced by producing a collimated molecular beam by means of a skimmer and aligning it perpendicularly to the resulting $(2\omega_1 + \omega_2)$ XUV beam. The latter is accomplished by adjusting the angles between incident laser beams and by addressing shifts between spectral lines in pure H_2 beams and seeded H_2/Ar beams.

6.3 Results

Table 6.1 – *Observed transition frequencies for P and R branch lines in the H_2 $B\,^1\Sigma_u^+$–$X\,^1\Sigma_g^+$ (19,0) Lyman band. The Δ_i represent deviations from previous investigations (present minus previous). All values given in cm^{-1}.*

J	P(J)	Δ_1 [a]	Δ_2 [b]	Δ_3 [c]	Δ_4 [d]
1	109653.067(20)	−0.17	0.10	−0.01	−0.05
2	109436.712(20)	−0.23	−0.34	−0.17	−0.07
3	109124.687(40)	−0.16	−0.25	0.22	−0.12
J	R(J)	Δ_1	Δ_2	Δ_3	Δ_4
0	109791.089(20)	−0.08	−0.09	−0.14	−0.07
1	109711.738(20)	−0.14	0.18	−0.10	−0.10
2	109534.895(20)		0.30	−0.10	0.02
3	109264.271(20)	−0.13	0.21	0.02	−0.03

[a] Difference to the results of Hinnen *et al.*[115]
[b] Difference to results of Namioka[117]
[c] Difference to results of Abgrall *et al.*[118]
[d] Difference to the calculated line positions resulting from the term levels of Abgrall *et al.*[119] and the ground state level energies from Jennings *et al.*[120]

For H_2 measurements are performed on the $B^1\Sigma_u^+ - X^1\Sigma_g^+$ (19,0) Lyman band; results for the line positions after averaging over various recordings and assessment of the uncertainty budget (dominated by the uncertainty in ω_1) are listed in Table 6.1. An error of $0.020\,cm^{-1}$ is estimated, except for the P(3) line for which no saturated I_2 line was available in the calibration procedure for ω_2; here the calibration relied on a wavelength meter. For all H_2-lines observed in this work a linewidth of $\approx 600 - 700$ MHz has been observed. This is the same width as obtained in studies

investigating H_2 spectral lines with narrowband XUV, produced via direct THG. From a comparison with results from Ubachs *et al.*[116] we estimate that the bandwidth of the $2\omega_2 + \omega_1$ XUV-beam is ≈ 300 MHz. The additional broadening is due to residual Doppler broadening in the slightly divergent high-velocity pulsed molecular beam. In Table 6.1 the observed transition frequencies are compared with previous results from XUV-laser spectroscopy, however at larger bandwidths,[115] from old classical spectroscopic studies,[117] and from a recent highly accurate classical study from the Meudon group.[118,119] Very accurate data result from Meudon excited state level energies,[119] combined with ground state level energies from far-infrared spectra;[120] these data are off by only $-0.06\,\mathrm{cm}^{-1}$ from the present data, which represent the highest accuracy frequencies on the (19,0) Lyman band. These lines could be included in analyses of quasar data aiming at uncovering a possible variation of the proton-to-electron mass ratio over cosmological time.[116]

Table 6.2 – *Observed transition frequencies and linewidths Γ_{obs} for lines in the $b\,^1\Pi_u - X\,^1\Sigma_g^+$ (12,0) band and the $b'\,^1\Sigma_u^+ - X\,^1\Sigma_g^+$ (8,0) band in N_2. The Δ represent deviations from results of previous investigations (present minus previous). All values given in cm^{-1}.*

	Line		Position	Δ		Γ_{obs}
b–X	(12,0)	Q(1)	109829.483(30)	-0.10^a		0.058(5)
b′–X	(8,0)	R(1)	109546.800(20)	-0.23^b	-0.37^c	0.023(3)
b′–X	(8,0)	R(0)	109546.211(20)	-0.19^b	0.00^c	0.026(3)
b′–X	(8,0)	R(2)	109545.712(20)	-0.26^b	-0.10^c	0.025(3)

[a] Ubachs *et al.*[121]
[b] Carroll *et al.*[122]
[c] Roncin *et al.*[123]

XUV-spectroscopic investigations in N_2 were performed as well. A single rotationally resolved Q(1) line in the $b^1\Pi_u - X^1\Sigma_g^+(12,0)$ band was recorded, for which a line width of $\Gamma_{\mathrm{obs}} = 1.74(15)$GHz is observed. After deconvolution of contributions from Doppler and laser source broadening a value results for the natural width, associated with the predissociation rate of the excited state; an excited lifetime of 105(25) ps is estimated.

In previous laser-based studies with larger bandwidths [121] a natural lifetime broadening effect could not be discerned. In addition the $b'^1\Sigma_u^+ - X^1\Sigma_g^+(8,0)$ band was recorded, for the first time resolving the band head section, as shown in Fig. 6.3. The obtained widths of 750 MHz are somewhat broader than the expected instrument width, and hence indicate predissociation of the $b'^1\Sigma_u^+$, $v = 8$ upper state, but at a lower rate than for $b^1\Pi_u$, $v = 12$. In Table 6.2 results on calibrated frequencies and observed widths are listed. For the measured transition frequencies a comparison is made with values obtained from previous studies.[122,123]

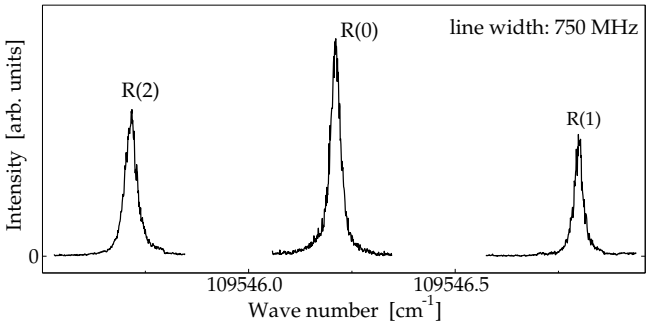

Figure 6.3 – *1+1′ photoionization recording of the R(0-2) lines of the* $b'\,^1\Sigma_u^+ - X\,^1\Sigma_g^+$ *(8,0) band in* N_2.

6.4 Conclusion

Narrow-band XUV generation in a non-collinear phase-matching scheme for resonance enhanced four-wave mixing is demonstrated and applied in spectroscopic measurements on highly excited states of H_2 and N_2. The accuracy of the obtained results is dominantly limited by the calibration of the ω_1 frequency laser and could be improved considerably when a better calibration procedure becomes available.

The authors thank J. P. Sprengers and E. Reinhold (LCVU), as well as F. Merkt (ETH Zürich) for helpful discussions. We gratefully acknowledge the Netherlands Foundation for Fundamental Research of Matter (FOM) for financial support.

Chapter 7

Deep-UV cavity ring-down spectroscopy

The sensitive optical detection technique of cavity ring-down spectroscopy is extended to the wavelength range 197–204 nm. A novel design narrow-band Fourier transform limited laser is used and the technique is applied for gas phase extinction measurements in CO_2 and SF_6. Further demonstration of the system capabilities is given in recordings of the Schumann–Runge (0,0), (1,0) and (2,0) bands in O_2 at unprecedented resolution.

This chapter is published in Optics Letters **29**, 1378-1380 (2004).

7.1 Introduction

After the discovery of cavity ring-down (CRD) spectroscopy,[124] this sensitive optical technique has been applied for direct absorption monitoring in a wide wavelength range, spanning from the infrared range at $10\,\mu$m,[125] via the entire visible domain to the ultraviolet. This broadness of wavelength range makes the technique applicable for gas phase studies in cells, molecular beam jets, etching plasma reactors, laser photolysis, flames, furnaces and heat pipe ovens, hollow cathode discharges, slit nozzle discharges, and diamond depositing flames. For an overview of such applications we refer to Berden *et al.*[126] At the UV end of the spectrum CRD was applied to detect the methyl radical in a hot filament reactor at $\lambda = 216\,$nm,[127] while detection of ammonia molecules via an absorption feature at $\lambda = 205\,$nm [128] marks the cutting edge of CRD at short wavelengths. The sensitivity in CRD is known to scale with $(1-\mathscr{R})$, with $\mathscr{R}$ the reflectivity of the mirrors forming the cavity; lower reflectivities decrease the number of round trips and therewith the time-span over which an optical decay transient can be recorded. Production of highly reflective mirrors deeper into the UV becomes gradually more difficult. Currently state-of-the art reflectivities measure $\mathscr{R} \approx 96-98\,\%$ at deep-UV wavelengths. Here we report on extending the domain of CRD beyond the 200 nm threshold into the deep-ultraviolet, with applications to extinction, Rayleigh scattering, resonant absorption and predissociative decay of small gas phase molecules.

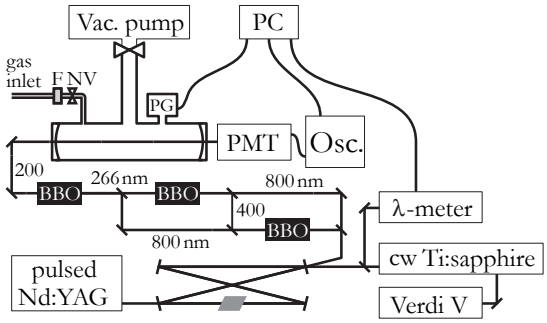

Figure 7.1 – *Layout of the laser system delivering tunable wavelength FT-limited pulses in the range 197 – 204 nm and the CRD-setup. Osc.: digital storage oscilloscope; PMT: photomultiplier tube; PG: pressure gauge; NV: needle valve; F: aerosol filter.*

7.2 Experimental setup

Wavelength tunable laser pulses in the range 197 – 204 nm are produced via a titanium:sapphire (Ti:sapphire) oscillator cavity, which is pumped by the green output of a seeded Nd:YAG Q-switched laser and injection-seeded by the continuous wave output of a Ti:sapphire laser. The oscillator cavity contains no other elements than the Ti:sapphire crystal; its cavity length is stabilized to the mode of the CW laser via the Hänsch–Couillaud locking scheme. Upon pumping at ~ 10 mJ/pulse it delivers near-infrared pulses at 1 mJ/pulse, at a duration of 15 – 24 ns, a 10 Hz repetition rate and in a bandwidth of about 50 MHz. The pulse duration is physically determined by the rate of stimulated mission in Ti:sapphire and is a function of pump power and of the reflectivity of the output coupler, which for these measurements was taken at ~ 90 %. Although we demonstrated that it is possible to amplify the output pulses to a level of 30 mJ/pulse in a bow-tie amplifier, for the present application this option is not employed. The effective 4^{th} harmonic of these pulses are produced via consecutive frequency-mixing processes in three β-barium-borate (BBO) crystals cut at the appropriate angles for type-I phase matching. Finally tunable narrow-band deep-UV pulses of $\sim 0.1 - 30\,\mu$J of 8 ns duration and a bandwidth of 100 MHz are produced, which are implemented in the CRD setup. The bandwidth in the UV was calibrated by resonantly probing Yb-atoms in a highly collimated beam by laser induced fluorescence.

The CRD configuration is composed of two highly reflective mirrors (Rocky Mountain Instruments; radius of curvature = 1 m) forming a sealed-off cavity of length 86 cm. The measured ring-down time in an evacuated cavity is 90 – 100 ns, corresponding to a reflectivity of 97 %. The cell can be evacuated by a turbomolecular pump and gas can be inserted via a needle valve, allowing for controlled pressure ramp scans as in previous CRD measurements in the visible domain.[129] The experimental configuration, including the laser setup and the ring-down geometry, is schematically depicted in Fig. 7.1.

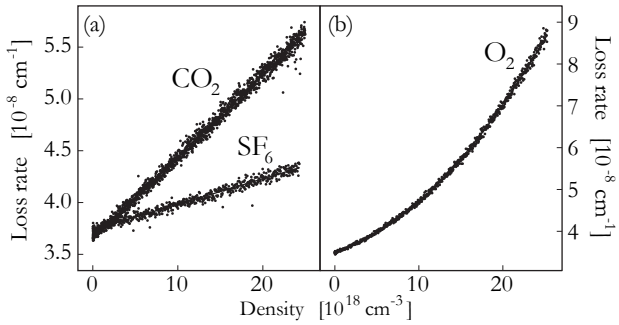

Figure 7.2 – *Extinction measurements as a function of density. (a) CO_2 and SF_6 exhibit a linear density dependence at 197.99 nm. (b) O_2 shows a quadratic pressure dependence, at 197.039 nm (50 751.4 cm^{-1}).*

Using a digital oscilloscope (LeCroy WaveRunner LT342, with a sampling speed of 500 MSample/s) CRD decay transients are recorded and transferred to a computer for further analysis. The decay time (1/e) of an empty cell is about 100 ns, while in extinction measurements transients as short as 40 ns are allowed by the analysis software. The laser pulse duration of 8 ns might produce a systematic deviation on the estimated decay rate, but calculation of the convolution integral shows that the resulting deviation is less than 1 % if decay transients of 4.5 τ_{cav} are used, as long as the fitting starts after the end of the pulse. The narrow bandwidth of the laser has the advantage that "slit function" effects causing underestimation of the absolute extinction cross section in CRD[128,130] do not play a role in the present investigation, not even when narrow lines are recorded; the linewidth of 100 MHz is much lower than the Doppler broadening of 3.3 GHz for O_2 at these short wavelengths. For an interpretation of ring-down transients in terms of a Beer's law exponential extinction it must be ensured that the measured transients follow a mono-exponential decay function. For this reason an alignment procedure was applied that optimizes the cavity for minimum deviation from a single exponential decay.[130]

7.3 Extinction rates in CO_2 and SF_6

Using a pressure-ramp method,[129] extinction cross sections of various gases can be determined. To avoid turbulence, the cell is slowly filled up to 1 bar over a time span of about 15 min and during this time the cavity decay rate is continuously monitored. Three of these pressure scans are displayed in Fig. 7.2 for various gases. Each data point corresponds to the decay rate of an average over five measured decay transients. Since the loss rate corresponds to $\beta_0 + N\sigma_{\bar{\nu}}$, with β_0 the empty cavity loss rate; the slope in the pressure curves is proportional to the extinction cross section $\sigma_{\bar{\nu}}$ of the gas. Small differences in the intercepts in Fig. 7.2 may occur, representing small differences in the mirror reflectivity as a result of cleaning of the mirrors and

Table 7.1 – *The extinction cross sections for SF_6 and CO_2 at 197.99 nm (50 507.96 cm^{-1}). The results are an average over several pressure scans.*

Gas	Measured cross section $[10^{-25}\,cm^2\,molecule^{-1}]$	Literature value $[10^{-25}\,cm^2\,molecule^{-1}]$
CO_2	86 ± 10	70[a]
SF_6	26 ± 4	23.6[b]

[a] From an interpolation between values given in Ogawa *et al.*[131]

[b] Refractive index extrapolated from two points;[132] King factor assumed to be unity.[133]

the time-interval over which the cell has been evacuated. From fits to this slope the extinction cross sections are derived, results of which are listed in Table 7.1 for CO_2 and SF_6. All measurements are performed at room temperature and the ideal gas law was applied to convert pressure into density N. The indicated errors follow from a weighted average over several pressure scans, with the weights derived from the fit of the decay transient and a subsequent fit on the pressure-ramp, and are 1σ estimates.

The observed extinction in carbon dioxide is largest. Previously Ogawa[131] investigated the absorption cross section of CO_2 in the region 172 – 216 nm and found a weak but complicated band structure, superimposed on an underlying dissociative continuum. Our measurement of an extinction cross section at one specific wavelength ($\lambda = 197.99$ nm) agrees with the lower resolution value; future work employing the narrow bandwidth and the tunability of the deep-UV laser system may help to unravel the onset of band structures in CO_2 at 198 nm.[131]

For SF_6 the extinction is expected to be determined by Rayleigh scattering. In SF_6 only two measurements of a refractive index exist in the visible and near infrared range.[132] Conversion into a cross section via

$$\sigma_\lambda^{\mathrm{R}} = 8\pi^3 (n_\lambda^2 - 1)^2 F_{\mathrm{k}}(\lambda)/(3N^2\lambda^4), \tag{7.1}$$

and assuming King factors $F_{\mathrm{k}}(\lambda)$ of this spherical molecule to equal unity, gives good agreement even in extrapolation to the deep-UV.

7.4 Results on oxygen

The continuous tunability of the novel deep-UV laser system was employed in the recording of spectra of three Schumann–Runge (SR) bands in O_2, parts of which are displayed in Fig. 7.3. It is for the first time that the triplet-spin structure in the weakest (0,0) band is resolved. These measurements allow for an accurate determination of the spin-state dependent effects in the spectra and in the predissociation rates in the $B\,^3\Sigma_u^-$, $v' = 0$ state, as well as an assessment of the competition between fluorescent decay and predissociation. The combination of the narrow bandwidth laser

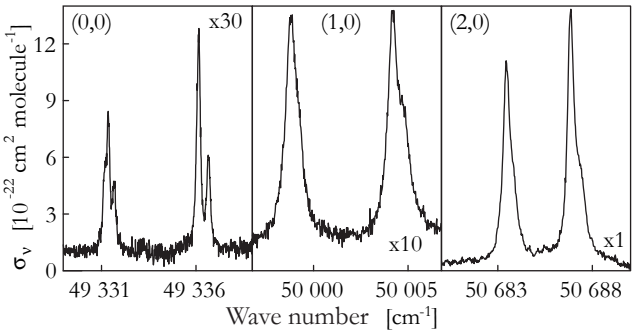

Figure 7.3 – *Spectral recording of part of the $B^3\Sigma_u^- \leftarrow X^3\Sigma_g^-$ (v′,0) band in molecular oxygen. As the (0,0) and (1,0) bands are the weakest, those signals were multiplied with the indicated factor. All sections of the spectrum span 10 cm^{-1}. The (0,0), (0,1) and (0,2) bands were measured at 290 mbar, 27.4 mbar and 4.3 mbar respectively.*

and the generation of exact fourth harmonics yields a highly accurate determination of deep-UV resonance frequencies;

frequencies of the seed-light were measured with an ATOS LM007 wavelength meter with an accuracy of $0.002\,\mathrm{cm}^{-1}$, which was verified during the measurement campaign by calibration on I_2 hyperfine lines measured in saturation. Line positions of single resolved lines in the $(0,0)$ SR band could be determined within $0.02\,\mathrm{cm}^{-1}$. From a fit to the rotational structure involving 64 lines accurate values of the fine structure constants were determined. The spin–spin interaction constant λ is determined to be $(1.642 \pm 0.007)\,\mathrm{cm}^{-1}$, the centrifugal distortion of this constant λ_D is $(-4.0 \pm 1.1) \times 10^{-4}\,\mathrm{cm}^{-1}$ and the spin–rotation constant γ is $(-3.11 \pm 0.03) \times 10^{-2}\,\mathrm{cm}^{-1}$. Besides the three bands originating in the $X^3\Sigma_g^-$, $v'' = 0$ ground state also the $(2,1)$ band probing vibrationally excited population was observed at room temperature overlapping the $(0,0)$ band. Phenomena of predissociation are associated with the linewidths, which can be seen to vary in Fig. 7.3 for the various v' levels. In future publications more details on the spectroscopy and on vibrational and spin-dependent predissociation rates (*cf.* a comparison with calculations of Lewis *et al.*[134]) will presented.

In addition to absorption measurements on the Schumann–Runge resonance features, pressure dependent extinction features were investigated in the Herzberg continuum of oxygen around 198 nm. The absorption in the Herzberg continuum in O_2 at wavelengths shorter than 240 nm is strongly modified by collisions, connected to a change in the dipole moment of the molecule, which breaks the symmetry rule that otherwise disallows the transition.[135,136] This leads to an intensity of the continuum with a quadratic density dependence. The wavelength range 200 – 240 nm is important in atmospheric physics, as this falls between the absorption by ozone and the strong absorption of the SR bands. One CRD-monitored pressure scan in O_2 is shown in Fig. 7.2 (b) for a measurement at 197.039 nm. A fit to the pressure-dependent loss rate gives both the linear and a quadratic contribution to the extinc-

Table 7.2 – *The extinction cross sections for* O_2 *in the Herzberg continuum.*

Wavelength [nm]	Linear contribution $[10^{-24}\,\mathrm{cm^2\,molecule^{-1}}]$	Quadratic contribution $[10^{-45}\,\mathrm{cm^5\,molecule^{-2}}]$
197.039	6.6 ± 0.8	549 ± 15
197.518	8.4 ± 0.8	580 ± 15
199.743	7.0 ± 0.8	471 ± 15
Results from Coquart *et al.*[135]		
197.04	8.10 ± 0.14	521 ± 6
197.52[a]	8.0 ± 0.4	534 ± 20
197.76	8.04 ± 0.27	514 ± 16

[a]Interpolated value

tion. The results for oxygen are listed in Table 7.2. Comparison with earlier measurements by Coquart *et al.*,[135] shows a reasonable agreement; Coquart *et al.* have a far lower resolution ($\sim 16\,\mathrm{cm^{-1}}$) and need to subtract the Schumann–Runge bands, whereas our resolution is much higher and resonances could be avoided. Future measurements will explore the cross section of this continuum in more detail.

7.5 Conclusion

In conclusion the technique of cavity ring-down spectroscopy has been extended below 200 nm in the deep-UV range. The sensitivity is currently limited by the low reflectivity of available mirrors, and could be improved once better mirrors can be produced. The CRD-technique is demonstrated in measurements on extinction of various gas phase molecules using a novel design deep-UV pulsed laser source with narrow bandwidth.

The Space Research Organisation Netherlands (SRON) and the Netherlands Foundation for Fundamental Research of Matter (FOM) are gratefully acknowledged for financial support.

Chapter 8

Deep-UV high resolution cavity ring-down spectroscopy of the Schumann-Runge bands in $^{16}O_2$ and $^{18}O_2$ at wavelengths 197 – 203 nm

With the use of a novel titanium:sapphire laser source delivering, upon fourth harmonic generation, narrowband and tunable radiation in the deep-UV, spectroscopic studies were performed on weak Schumann-Runge bands of oxygen. Improved values for rotational and fine structure molecular parameters for the $B\,^3\Sigma_u^-$, $v = 0 - 2$ states of $^{16}O_2$ were determined, as well as values for the $v = 0 - 1$ states in $^{18}O_2$. Signal detection was accomplished via cavity ring-down spectroscopy.

This chapter is published in the Journal of Molecular Spectroscopy **232**, 151-156 (2005).

8.1 Introduction

Spectroscopic investigation on the Schumann-Runge (SR) bands, corresponding to the $B\,^3\Sigma_u^- \leftarrow X\,^3\Sigma_g^-$ system in molecular oxygen, has a long history. Brix and Herzberg were first to unravel triplet fine-structure characteristics for the oxygen $^3\Sigma \leftarrow {}^3\Sigma$ system.[137] Thereafter many investigations have been carried out yielding accurate information on molecular constants and dynamics of the excited rovibrational levels. The importance of the SR absorption system for the modeling of the Earth's atmosphere and its radiation budget needs no further elucidation.

The SR-system is a strongly allowed system, in fact the first dipole-allowed system in oxygen. Peculiarly, in O_2 all transitions between electronic states pertaining to the assembly of two ground state ^3P atoms are forbidden in the electric dipole approximation. However, excitation to the lowest vibrational levels in the $B\,^3\Sigma_u^-$ excited state is weak, due to the shift toward large internuclear separation of its potential. Particularly the (0,0) band in the SR band system is extremely weak;

it is a textbook example of a transition solely based on wave-function density in the classically forbidden region. It was not before 1970 that this weak (0,0) band was studied,[138] although the fine structure could not be resolved. In a series of investigations Yoshino and co-workers reinvestigated the oxygen SR bands at high resolution establishing a set of molecular constants representing current knowledge on the system.[139–146] For the (0,0) band a band oscillator strength as small as 2.95×10^{-10} was derived. From a determination of an empirical RKR potential Franck-Condon factors were calculated that indeed give a value as low as 3.0×10^{-9} for this band.[147] The same group extended their studies from the main isotopomer $^{16}O_2$ to the less abundant $^{16}O^{18}O$[144] and $^{18}O_2$,[145] thus providing an extensive database on the spectrum of the SR-bands.

In the present study high-resolution spectral recordings are performed on the SR $B\,^3\Sigma_u^- \leftarrow X\,^3\Sigma_g^-$ system at wavelengths near 200 nm, measuring the (0,0), (1,0), (2,0) and (2,1) bands in $^{16}O_2$ using cavity ring-down spectroscopy (CRDS) and a newly designed ultra-narrow bandwidth laser system in the deep-UV. The methodical aspects of the extension of CRDS into the deep-UV wavelength region were documented before;[39] here the focus is on the spectroscopic results. Also in $^{18}O_2$ a hitherto unscanned region of the SR-bands near 200 nm was investigated. The study results in upper state vibrational level molecular constants for $v' = 0-2$ in $^{16}O_2$ and $v' = 0-1$ in $^{18}O_2$.

8.2 Experimental

The well-known CRDS technique is applied for an investigation of some of the Schumann-Runge bands absorbing near 200 nm. A novel-type narrow band laser system is employed that was documented before.[39] A four-mirror ring-configuration gain-switched Ti:sapphire oscillator, which is longitudinally pumped by the output of a Q-switched frequency-doubled Nd:YAG laser (532 nm), is injection-seeded by the output of a continuous wave (CW) ring Ti:sapphire laser. Under optimum conditions this system delivers laser pulses of 15 ns duration and of near-Fourier-transform limited bandwidth at pulse energies of up to 30 mJ after amplification in a bow-tie Ti:sapphire amplifier, that is also pumped by the Q-switched Nd:YAG laser. Tuning range of the system is currently between 790 – 855 nm. Deep-UV radiation at frequency ω_{DUV} is produced by non-linear conversion of the infrared (IR) output (ω_{IR}) in three consecutive steps: $\omega_{blue} = 2 \times \omega_{IR}$, $\omega_{UV} = \omega_{blue} + \omega_{IR}$, and $\omega_{DUV} = \omega_{UV} + \omega_{IR}$ in three nonlinear crystals (BBO) cut at appropriate angles for phase-matching. Continuous tunability of the system is 1 cm^{-1} in the IR range, so for extended spectral coverage overlapping scans have to be made.

CRDS recordings at deep-UV wavelengths were obtained using a cell of length 80 cm and a diameter of 1 cm, similar as in a previous study on one of the weaker visible band systems.[148] The optical cavity, spanning the entire cell length, is formed by two reflective mirrors with $\mathscr{R} \approx 97\,\%$ in the range 197 – 203 nm, radius-of-curvature 1 m, and 25 mm diameter. The recordings were performed at gas pressures in the

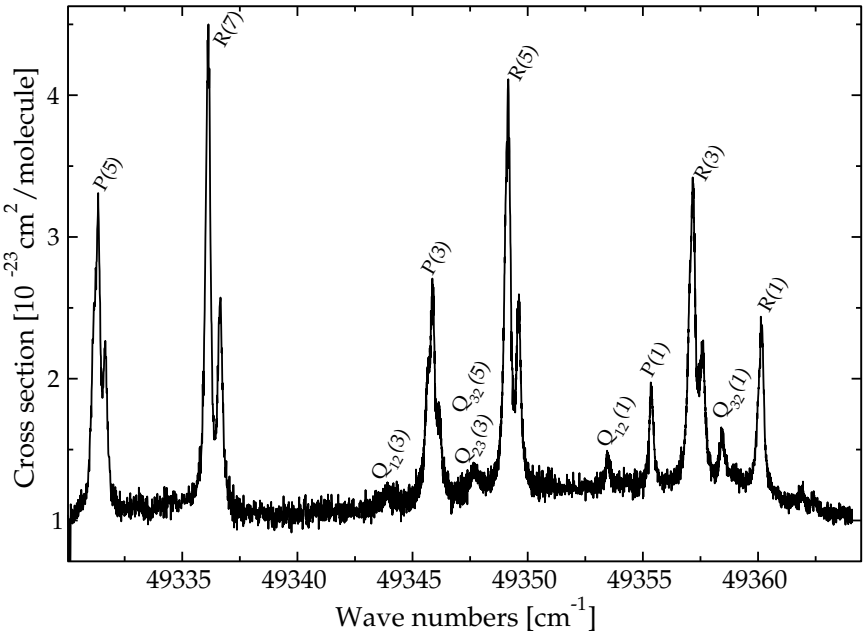

Figure 8.1 – *Recorded spectrum by means of the CRD-method of the band head of the* $B^3\Sigma_u^- \leftarrow X^3\Sigma_g^-$ *(0,0) band in* $^{16}O_2$*. In some of the lines the fine-structure splitting is readily observable.*

range 30 – 300 mbar, where the pressure was on-line monitored on a baratron. The methods for monitoring and evaluating the CRD-transients, and retrieving the absorption spectrum were described previously.[39]

Wavelength calibration was performed by using an ATOS wavelength meter on the near-IR output of the CW Ti:sapphire laser. This commercial instrument consists of four internal etalons providing an accuracy of 50 MHz, which was regularly verified in our laboratory by measuring absolute wavelengths of I_2 saturation lines as described in Velchev *et al.*[149] The calibration procedures lead to an absolute accuracy of the wavelength scale better then 200 MHz or 0.006 cm^{-1} at deep-UV wavelengths.

8.3 Spectroscopic analysis

In Fig. 8.1 a typical CRD-recording of the band-head region of the SR (0,0) band of $^{16}O_2$ is displayed. The horizontal axis is derived from the simultaneous wavelength measurements by the ATOS λ-meter. The values along the vertical axis in principle represent the absolute cross sections at the specified frequencies, although no efforts are undertaken to correct for possible systematic effects, e.g. due to underestimates introduced by the analysis of the decay transients.[130] Voigt line profiles were used to determine line centers of the specific rotational components in the spectrum in

a fitting analysis. The resulting transition frequencies for the six principal branches in the SR (0,0) band are listed in Table 8.2 as well as a few weaker lines pertaining to side-branches. The accuracy of the line positions in the (0,0) band is estimated at $0.02\,\mathrm{cm}^{-1}$ for most of the lines, and somewhat less accurate for some weak lines.

Similarly retrieved line positions on the SR (1,0), (2,0) and (2,1) bands in $^{16}O_2$ are listed in Tables 8.3, 8.4 and 8.5. The accuracies in the determination of line positions is $0.03\,\mathrm{cm}^{-1}$ in the (1,0) band, and $0.04\,\mathrm{cm}^{-1}$ in the bands probing the $v' = 2$ state. The lower accuracy is due to the increased widths in the spectra, an effect of predissociation. For $^{18}O_2$ the retrieved line positions in the (0,0) and (1,0) bands are presented in Tables 8.7 and 8.6.

The observed line positions were used to derive molecular constants for the excited state vibrational levels. The SR system corresponds to an allowed $^3\Sigma_u^- - {}^3\Sigma_g^-$ transition having in total fourteen rotational branches, of which six principal branches, P_1, P_2, P_3, R_1, R_2, R_3, four weaker branches Q_{12}, Q_{21}, Q_{23}, Q_{32}, and four very weak branches P_{13}, P_{31}, R_{13}, and R_{31}. These branches and the fine-structure levels involved, including (+/−) and (e/f) parities are displayed in Fig. 8.2. Both ^{16}O and ^{18}O have $I = 0$ nuclei and therefore the even rotational levels in the $X\,^3\Sigma_g^-$ ground state do not exist in the homonuclear $^{16}O_2$ and $^{18}O_2$ molecules.

For the triplet structure of the excited state we follow the analysis of Cheung *et al.*,[142] who obtained for the F_2 levels an expression:

$$\begin{aligned} E(F_2) &= \nu_0 + Bx - Dx^2 + \frac{2}{3}[\lambda + (1+x)\lambda_D] \\ &\quad - [\gamma + (1+x)\gamma_D] \end{aligned} \tag{8.1}$$

using $x = J(J+1)$. Here ν_0 is the vibronic band origin, B is the rotational constant, D the centrifugal distortion parameter, λ and λ_D the spin-spin interaction parameters, and γ and γ_D the spin-rotation interaction parameters. Energies $E(F_1)$ and $E(F_3)$ levels are obtained from a diagonalization of a matrix:

$$\begin{pmatrix} M_{11} & M_{12} \\ M_{21} & M_{22} \end{pmatrix}$$

with elements:

$$\begin{aligned} M_{11} &= \nu_0 + B(x+2) - D(x^2+8x+4) \\ &\quad -\frac{4}{3}[\lambda + (x+2)\lambda_D] \\ &\quad -2\gamma - 4\gamma_D(x+1) \end{aligned} \tag{8.2}$$

$$\begin{aligned} M_{12} &= -2\sqrt{x}\,[B - 2D(x+1)] \\ &\quad -\sqrt{x}\left[\gamma + \gamma_D(x+4) - \frac{4}{3}\lambda\right] \end{aligned} \tag{8.3}$$

$$\begin{aligned} M_{22} &= \nu_0 + Bx - D(x^2+4x) \\ &\quad +\frac{2}{3}[\lambda + x\lambda_D] - \gamma - 3x\gamma_D \end{aligned} \tag{8.4}$$

$$M_{21} = M_{12} \tag{8.5}$$

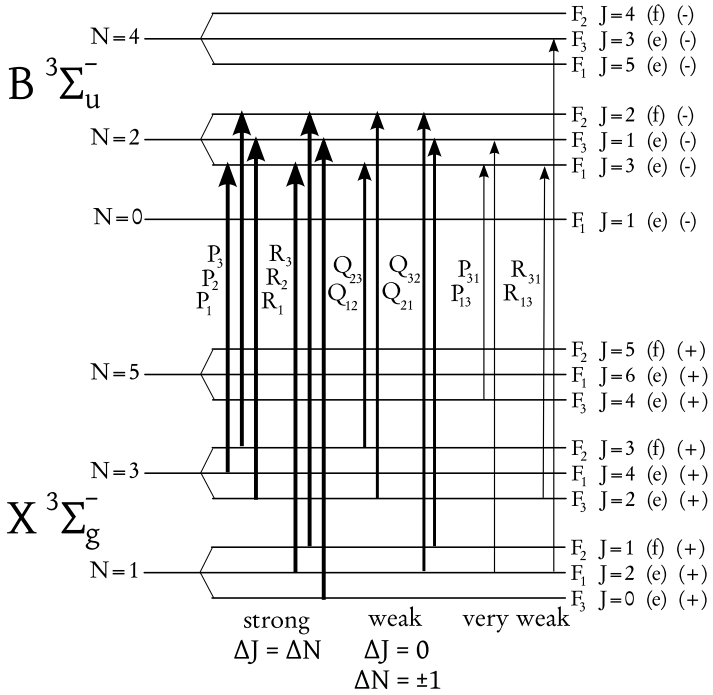

Figure 8.2 – *Rotational branches of all allowed transitions in the $B\,^3\Sigma_u^- \leftarrow X\,^3\Sigma_g^-$ system. Only the levels existing in homo-nuclear spin-0 oxygen isotopomers are shown. For clarity all (+/–) and (e/f) parity assignments are given, as well as the fine-structure labels F_i, the pure rotation quantum numbers N, and the total angular momentum values J.*

For the $X\,^3\Sigma_g^-$ ground state a more detailed Hamiltonian is used, following the treatment of Rouillé *et al.*[150] Included are higher centrifugal distortion parameters than in the simplified treatment of the excited state given above. Previously, this Hamiltonian was used and verified in high-resolution studies in an analysis of a sequence of vibrational bands (0,0) to (3,0) in the $b\,^1\Sigma_g^+ \leftarrow X\,^3\Sigma_g^-$ system.[148,151–153] Accurate constants for the ground state are determined from Raman, far-infrared and laser-magnetic-resonance data and are listed in Rouillé *et al.*[150] for $^{16}O_2$ for both $v = 0$ and $v = 1$ levels. These molecular constants and the ones pertaining to $^{18}O_2$, as obtained from Steinbach and Gordy[154] are listed in Table 8.1. In the fits these highly accurate constants are kept fixed.

For all bands separate weighted least-squares fitting routines were performed, except for the (2,0) and (2,1) bands of $^{16}O_2$. In the latter case the constants pertaining to both ground state vibrational levels $v = 0$ and $v = 1$ were kept fixed, including the separation between ground state vibrational levels ν_{10}, which is more accurate in the Raman investigations[150] than in the present study. Parameters for $B\,^3\Sigma_u^-$, $v' = 2$ were derived from the combined fit to both sets of data. Resulting molecular con-

Table 8.1 – *Molecular constants for the $X^3\Sigma_g^-$ ground state of oxygen for the isotopes investigated in the present study. All values in cm.*

Constant	$^{16}O_2(v=0)$	$^{16}O_2(v=1)$	$^{18}O_2(v=0)$
B	1.437 676 476	1.421 864 54	1.278 008 47
D	$4.842\,56 \times 10^{-6}$	$4.841\,8 \times 10^{-6}$	3.835×10^{-6}
H	2.8×10^{-12}	2.8×10^{-12}	
ν_{10}		1556.389 91	
λ	1.984 751 322	1.989 578 940	1.984 596 22
λ_D	$1.945\,21 \times 10^{-6}$	$2.109\,24 \times 10^{-6}$	1.738×10^{-6}
λ_H	1.103×10^{-11}	1.103×10^{-11}	
γ	$-8.425\,390 \times 10^{-3}$	$-8.445\,771 \times 10^{-3}$	$-7.486\,48 \times 10^{-3}$
γ_D	-8.106×10^{-9}	-8.264×10^{-9}	-11.7×10^{-9}
γ_H	-4.7×10^{-14}		
Ref.	[150]	[150]	[154]

stants are listed in Table 8.8 for $^{16}O_2$ and in Table 8.9 for $^{18}O_2$. The standard deviations in the fits are commensurate with the estimated uncertainties in the transitions frequencies: 0.02 cm^{-1} for $^{16}O_2$ (0,0), 0.03 cm^{-1} for (1,0) and 0.04 cm^{-1} for the fit of the (2,0) and (2,1) bands. The standard deviation in the fit for the $^{18}O_2$ (0,0) band corresponds to 0.02 cm^{-1}, and for the (1,0) band to 0.04 cm^{-1}. The unblended lines agree reasonably well, at the level of the estimated uncertainties, without systematic shifts. At the same time deviations between calculated and observed line positions are found for the blended lines. For example for $J \leq 17$ the unresolved splitting between P_1 and P_2 components (see Table 8.2) causes systematic upward (P_1) and downward (P_2) shifts. Similarly the data and the deviations indicate a crossing of R_1 and R_2 components within the observed and assigned lines in the (1,0) band of $^{16}O_2$ (Table 8.3).

In Table 8.8 the presently derived molecular constants are compared with those of Cheung *et al.*[147] The present values for the rotational and fine-structure constants are more accurate, as a consequence of the improved resolution and frequency calibration. In the fitting procedure there is some ambiguity on the band origin. Cheung *et al.*[147] find a value for ν_0 that is redshifted by 1.4 cm^{-1} for $^{16}O_2$. In our definition we take the trace of the Hamiltonian (the one of Rouillé *et al.*[150]) as the zero level for the ground state energies. The lowest energy level in the $X\,^3\Sigma_g^-$, $v = 0$ state is the $N = 0, J = 1$ level, which does not exist in the homonuclear $^{16}O_2$ molecule; it has a predicted level energy of $-0.450\,cm^{-1}$, so below the trace of the Hamiltonian. In $^{16}O^{18}O$ this level does exist however, at a slightly different energy.[152] In our calculation of ground state energy levels we find a non-existent $N = 0, J = 0$ level at 1.332 cm^{-1} for $^{16}O_2$ and at 1.331 cm^{-1} for $^{18}O_2$. Assuming that Cheung *et al.*[147] have taken this level as the zero for their ground state energies, and correcting for it,

a genuine calibration difference of $0.10\,\mathrm{cm}^{-1}$ between the present result and that of Cheung *et al.* is left. This is reasonable in view of the resolution and the calibration procedures followed in Cheung *et al.*[147] The presently obtained value for the band origin is also in accordance with the old value of Ackerman and Baume[138] yielding $\nu_0 = 49358.15\,\mathrm{cm}^{-1}$.

The previous extensive work on $^{18}O_2$ by Cheung *et al.*[144] did not cover the (0,0) and (1,0) bands, hence no comparison can be made. Isotopic scaling of the rotational constants can be verified by comparing the rotational constants in $B\,^3\Sigma_u^-$, $v = 0$ for the $^{16}O_2$ and $^{18}O_2$ isotopomers, giving $B(^{18}O_2)/B(^{16}O_2) = 0.8879(4)$, which is within 2σ from the reduced mass ratio of $\mu(16)/\mu(18) = 0.8886$.

8.4 Conclusion

A study of the lowest vibrational levels of the $B\,^3\Sigma_u^-$ state in oxygen has been performed at unprecedented resolution, using a novel ultra-narrow band laser source in the deep ultraviolet and cavity ring-down absorption at these short wavelengths. Improved molecular constants have been obtained for the $v' = 0 - 2$ levels in $^{16}O_2$ and $v' = 0 - 1$ in $^{18}O_2$.

Acknowledgments

The authors wish to thank B.R. Lewis (Canberra) for discussions and advise. The Netherlands Foundation for Fundamental Research of Matter (FOM) and the Space Research Organisation Netherlands (SRON) are acknowledged for financial support.

Table 8.2 – *Observed transition frequencies for the main P and R branch lines in the* $B^3\Sigma_u^- \leftarrow X^3\Sigma_g^-$ *(0,0) band in* $^{16}O_2$ *and deviations from a least-squares fit (in parentheses). Blended lines are marked with b. Values in* cm^{-1}.

N	P_1	P_2	P_3	R_1	R_2	R_3
1	49355.368 (5)			49360.172 (-1)	49360.051 (11)	49362.424 (19)
3	49345.872 (3)	49345.653 (-11)	49346.164 (13)	49357.191 (3)	49357.052 (5)	49357.585 (-22)
5	49331.353 (1)	49331.165 (-7)	49331.662 (3)	49349.157 (-17)	49349.020 (-37)	49349.602 (-11)
7	49311.893 (5)	49311.686 (-2)	49312.214 (7)	49336.168 (14)	49336.071 (2)	49336.649 (-6)
9	49287.337 (16)	49287.221 (9)	49287.776 (6)		49318.120 (38)	49318.720 (10)
11	49257.828 (11)	49257.734 (-11)	49258.344 (-4)			
13	49223.311[b] (-14)	49223.311[b] (22)	49223.934 (-7)	49267.048 (-46)	49267.125 (12)	49267.831 (-3)
15	49183.851[b] (4)	49183.851[b] (5)	49184.543 (-4)	49234.057 (-21)	49234.152 (22)	49234.898 (-3)
17	49139.407[b] (23)	49139.407[b] (-11)	49140.175 (6)	49196.064 (0)	49196.160 (12)	49196.963 (-7)
19	49089.954[b] (14)	49089.954[b] (-52)	49090.803 (-6)			
21	49035.576[b] (60)	49035.576[b] (-36)	49036.514 (47)	49105.037 (-8)	49105.193 (5)	49106.119 (6)
23	48976.136[b] (22)	48976.136[b] (-103)	48977.137 (-9)			
	Q_{12}	Q_{21}	Q_{23}	Q_{32}		
1	49353.481 (-5)	49361.868 (-49)		49358.464 (21)		
3	49343.920 (0)		49347.707 (-41)			
5				49347.692 (91)		

Table 8.3 – *Observed transition frequencies for the $B^3\Sigma_u^- \leftarrow X^3\Sigma_g^-$ (1,0) band in $^{16}O_2$ and deviations from a least-squares fit. Values in cm^{-1}.*

N	P_1	P_2	P_3	R_1	R_2	R_3
1	50042.865 (-19)			50047.602[b] (-24)	50047.602[b] (12)	
3				50044.410[b] (-43)	50044.410[b] (0)	50044.865 (-54)
5	50018.615[b] (-2)	50018.615[b] (79)	50019.007 (35)	50036.130[b] (-8)	50036.130[b] (4)	50036.656 (27)
7	49998.791[b] (-6)	49998.791[b] (34)	49999.241 (19)	50022.703[b] (-1)	50022.703[b] (-30)	50023.262 (-5)
9	49973.875[b] (4)	49973.875[b] (-1)	49974.402 (20)	50004.171[b] (17)	50004.171[b] (-58)	50004.772 (-32)
11				49980.546[b] (59)	49980.546[b] (-64)	49981.253 (22)

Table 8.4 – *Observed transition frequencies for the $B^3\Sigma_u^- \leftarrow X^3\Sigma_g^-$ (2,0) band in $^{16}O_2$ and deviations from a least-squares fit. Values in cm^{-1}.*

N	P_1	P_2	P_3	R_1	R_2	R_3
1	50707.944 (-56)			50712.665[b] (-4)	50712.665[b] (-4)	
3	50698.344[b] (-22)	50698.344[b] (51)	50698.776 (46)	50709.306[b] (4)	50709.306[b] (16)	50709.838 (66)
5	50683.451[b] (-15)	50683.451[b] (35)	50683.823 (-1)	50700.689[b] (10)	50700.689[b] (-5)	50701.180 (16)
7	50663.343[b] (4)	50663.343[b] (18)	50663.775 (18)	50686.843[b] (16)	50686.843[b] (-37)	50687.331 (-45)
9	50638.011[b] (17)	50638.011[b] (-12)	50638.497 (6)	50667.788[b] (36)	50667.788[b] (-60)	50668.363 (-19)
11	50607.462[b] (25)	50607.462[b] (-49)	50608.012 (-9)	50643.455 (-2)	50643.655 (57)	50644.203 (28)
13	50571.712[b] (43)	50571.712[b] (-78)	50572.349 (3)	50613.941 (-1)	50614.212 (82)	50614.778 (25)
15	50530.688 (-7)	50530.939 (76)	50531.486 (20)	50579.202 (-8)	50579.507 (62)	50580.123 (8)
17	50484.515 (-2)	450484.781 (48)	50485.451 (67)	50539.245 (-15)	50539.574 (30)	50540.300 (38)
19				50494.056 (-39)	50494.429 (1)	50495.199 (5)
	Q_{21}	Q_{32}				
1	50714.654 (108)	50711.071 (49)				

Table 8.5 – *Observed transition frequencies for the $B^3\Sigma_u^- \leftarrow X^3\Sigma_g^-$ (2,1) band in $^{16}O_2$ and deviations from a least-squares fit. Values in cm^{-1}.*

N	P_1	P_2	P_3	R_1	R_2	R_3
1	49151.558 (-88)					
3				49153.081[b] (-25)	49153.081[b] (-6)	49153.495 (-74)
5	49127.516[b] (-37)	49127.516[b] (19)	49127.894 (-14)	49144.779[b] (12)	49144.779[b] (4)	49145.252 (4)
7	49107.867[b] (30)	49107.867[b] (49)	49108.325 (72)	49131.339[b] (13)	49131.339[b] (-33)	49131.870 (-2)
9	49083.024[b] (-6)	49083.024[b] (-29)	49083.529 (4)	49112.811[b] (23)	49112.811[b] (-67)	49113.411 (-5)
11	49053.165[b] (29)	49053.165[b] (-40)	49053.704 (15)	49089.144[b] (-13)	49089.144[b] (-148)	
13	49018.185[b] (25)	49018.185[b] (-89)	49018.800 (-34)	49060.488[b] (55)	49060.488[b] (-127)	49061.215 (-26)
15	48978.105[b] (2)	48978.105[b] (-160)	48978.706 (-165)	49026.599 (-18)	49026.886 (40)	49027.459 (-62)

Table 8.6 – *Observed transition frequencies for the main P and R branch lines in the $B^3\Sigma_u^- \leftarrow X^3\Sigma_g^-$ (1,0) band in $^{18}O_2$ and deviations from a least-squares fit. Values in cm^{-1}.*

N	P_1	P_2	P_3	R_1	R_2	R_3
1	50029.548 (-26)			50033.813[b] (-22)	50033.813[b] (10)	
3				50030.993[b] (-33)	50030.993[b] (6)	50031.576 (103)
5	50008.039[b] (-18)	50008.039[b] (54)	50008.414 (0)	50023.646[b] (-6)	500 23.646[b] (7)	50024.131 (13)
7	49990.457[b] (-1)	49990.457[b] (38)	49990.909 (43)	50011.723[b] (-12)	50 011.723[b] (-35)	50012.250 (-12)
9	49968.339[b] (15)	49968.339[b] (15)	49968.873 (69)	49995.293[b] (15)	49995 .293[b] (-48)	49995.877 (-5)
11				49974.318[b] (36)	49974 .318[b] (-70)	49974.963 (-7)
13				49948.818[b] (72)	49948.818[b] (-79)	49949.549 (27)

Table 8.7 – *Observed transition frequencies for the main P and R branch lines in the $B^3\Sigma_u^- \leftarrow X^3\Sigma_g^-$ (0,0) band in $^{18}O_2$ and deviations from a least-squares fit. At the bottom of the Table a single side-branch line is given. Values in cm^{-1}.*

N	P_1	P_2	P_3	R_1	R_2	R_3
1	49380.309 (5)			49384.592 (-26)		
3	49371.915 (19)	49371.786 (51)	49372.223 (-3)	49381.990 (24)	49381.864 (-1)	4 9382.360 (-9)
5	49359.010 (13)	49358.838 (-25)	49359.304 (-7)	49374.857 (15)	49374.718 (-61)	49375.255 (-6)
7	49341.665 (17)	49341.574 (15)	49342.022 (13)	49363.245 (-24)		49363.734 (- 7)
9		49319.864 (40)	49320.275 (-8)	49347.235 (-17)		49347.789 (0)
11	49293.604 (28)			49326.795 (2)		49327.398 (-1)
13				49301.909 (13)		49302.564 (-6)
15	49227.896 (12)	49227.883 (-167)	49228.543 (23)			49234.898 (-3)
17	49188.376 (8)		49189.064 (-9)	49238.786 (-4)		49239.617 (21)
19				49200.586 (1)		49201.439 (-14)
	Q_{32}					
1	49382.938 (-18)					

Table 8.8 – *Molecular constants for the $B^3\Sigma_u^-$, $v = 0 \ldots 2$ states of $^{16}O_2$ as obtained from the fits. All values in cm^{-1}. The values for the $v = 2$ state were obtained from a simultaneous fit to the (2,0) and (2,1) bands. The values of Ref. [147] for the ground state zero level are corrected by 1.33 cm^{-1} (see text).*

Constant	$^{16}O_2(v=0)$	Ref. [147]	$^{16}O_2(v=1)$	Ref. [147]	$^{16}O_2(v=2)$	Ref. [147]
B	0.81348 (7)	0.8132 (3)	0.7999 (2)	0.7993 (3)	0.7857 (1)	0.7860 (2)
D×10^6	4.5 (1)	4.5 (6)	6.5 (1.8)	4.2 (5)	4.5 (5)	4.4 (3)
ν_0	49358.242 (6)	49358.14 (3)	50045.821 (15)	50045.70 (3)	50710.978 (9)	50710.86 (2)
λ	1.640 (7)	1.69 (3)	1.71 (2)	1.70 (3)	1.740 (7)	1.69 (2)
$\lambda_D \times 10^4$	-4.1 (1.1)					
$\gamma \times 10^2$	-3.18 (6)	-2.8 (1)	-3.51 (16)	-2.6 (1)	-3.39 (4)	- 2.9 (1)
$\gamma_D \times 10^6$	2.4 (1.8)					

Table 8.9 – *Molecular constants for the $B^3\Sigma_u^-$, $v = 0$ state of $^{18}O_2$. All values in cm^{-1}.*

Constant	$^{18}O_2(v=0)$	$^{18}O_2(v=1)$
B	0.7223 (3)	0.7118 (3)
D×10^6	3.1 (2)	4.5 (1.5)
ν_0	49382.916 (6)	50032.237 (14)
λ	1.668 (14)	1.725 (14)
$\lambda_D \times 10^4$	20 (9)	
$\gamma \times 10^2$	-3.2 (1)	-3.28 (9)
$\gamma_D \times 10^6$	9 (4)	

Chapter 9

Pressure broadening and fine-structure dependent predissociation in oxygen $B\,^3\Sigma_u^-$, $v = 0$.

Both laser-induced fluorescence and cavity ring-down spectral observations were made in the Schumann-Runge band system of oxygen, using a novel type ultranarrow deep-UV pulsed laser source. From measurements on the very weak (0,0) band pressure broadening, pressure shift and predissociation line broadening parameters were determined for the $B\,^3\Sigma_u^-$, $v = 0$, F_i fine structure components for various rotational levels in O_2. The information content from these studies was combined with that of entirely independent measurements probing the much stronger (0,10), (0,19) and (0,20) Schumann-Runge bands involving preparation of vibrationally excited O_2 molecules via photolysis of ozone. The investigations result in a consistent set of predissociation widths for the $B\,^3\Sigma_u^-$, $v = 0$ state of oxygen.

This chapter is published in the Journal of Chemical Physics **123**, 174318 (2005).

9.1 Introduction

The oxygen Schumann-Runge (SR) band system is an extremely important absorption system for the radiation budget and the chemistry of the Earth's atmosphere. Photoabsorption via the SR bands controls the penetration depth of deep-UV radiation into the lower levels of the atmosphere and its interaction with other molecules such as N_2O, H_2O, HNO_3 and fluorocarbons.[155] Near 200 nm, where the SR-bands of O_2 are weak, and the absorption by ozone is weak as well, the $1/e$ value of radiation penetrating into the Earth's atmosphere lies in the stratosphere. Predissociation via the upper $B\,^3\Sigma_u^-$ state in oxygen molecules is the source of ground state atomic oxygen (^3P) in the atmosphere above 60 km. In view of their atmospheric relevance detailed quantitative studies into the finest details of the predissociation phenomena in O_2 ($B\,^3\Sigma_u^-$) are warranted.

On the experimental side Lewis *et al.* have investigated predissociation phenomena for the main isotopomer,[156] for $^{16}O^{18}O$,[157] and for $^{18}O_2$.[158] Cheung *et al.* have also determined predissociation linewidths for bands (1,0) to (12,0) in $^{16}O_2$ [159] as well as for the $^{16}O^{18}O$ and $^{18}O_2$ species.[160] Yang *et al.*[161] investigated predissociation in $v' = 10 - 11$ levels by monitoring laser-induced fluorescence. There have been numerous theoretical studies on the nature of the predissociation mechanism, where most of the work is based on the initial framework developed by Julienne.[162] Cheung and co-workers performed calculations to unravel the rotational, vibrational, isotopic and fine-structure effects on the rates of dissociation.[163–166] Alternative calculations on all details pertaining to the predissociation widths including fine structure dependencies were performed by Lewis *et al.*[134] An extensive and comparative study on the predissociation was performed combining data from laser-induced fluorescence spectroscopy, high-resolution absorption, and VUV-Fourier-transform spectroscopy.[167] Finally, *ab initio* calculations on the predissociation mechanism in O_2 were undertaken by Li *et al.*[168]

In most studies the lowest $B\,^3\Sigma_u^-$, $v' = 0$ level, which is the least subject to predissociation, was not included because the Franck-Condon factor for excitation from the $X\,^3\Sigma_g^-$, $v" = 0$ ground vibrational level, in the weak (0,0) band is very small (at the 10^{-9} level). Cosby *et al.*[169] were able to investigate the $B\,^3\Sigma_u^-$, $v = 0$ state through a scheme, where O_2 in the $v = 9, 10$ and 21 levels of the $X\,^3\Sigma_g^-$ ground state was prepared via laser-photolysis of ozone. This has the advantages that Franck-Condon factors for the bands probing $B\,^3\Sigma_u^-$, $v = 0$ are largely increased and the spin-splittings in the corresponding bands are favorably enlarged.

In the present study new information is obtained on the predissociation properties of the $B\,^3\Sigma_u^-$ upper state, with a special focus on the lowest $v' = 0$ vibrational level. New measurements performed at the Amsterdam Laser Centre are combined with remeasurements at SRI following the experimental scheme of Cosby *et al.*[169] The bandwidth of the deep UV laser excitation source used in Amsterdam (100 MHz or $0.003\,cm^{-1}$) is so narrow, that the true molecular line shape can be determined, resulting from Doppler, predissociation and collisional widths. These linewidth measurements are an extension to a spectroscopic study on the (0,0) and some other bands that have been published separately.[40] From a comparison of relative line intensities obtained in cavity-ring-down (CRD) measurements and laser-induced-fluorescence (LIF) information on fine-structure dependent predissociation rates is obtained. Also from a detailed analysis of the spectral line shape of the singly resolved $P_1(1)$ line in the $B\,^3\Sigma_u^- \leftarrow X\,^3\Sigma_g^-(0,0)$ band a pressure broadening and a pressure shift coefficient could be determined. It is for the first time that these collisional effects are observed in the $B\,^3\Sigma_u^-$, $v = 0$ state; the results are however in good agreement with previous work on higher v' levels.[170,171]

In the SRI experiments, the O_2 is prepared in excited vibrational levels and probed by a narrow band tunable laser. LIF spectra were recorded for the (0,10), (0,19), and (0,20) bands using the fundamental and second harmonics, respectively, of the tunable dye laser. The advantage of probing the $B\,^3\Sigma_u^-$ state from the excited

vibrational levels of the $X\,^3\Sigma_g^-$ ground state are twofold. Firstly, much lower photon energies are required to access the $B\,^3\Sigma_u^-$, $v = 0$ level, with a corresponding decrease in the Doppler broadening of the transitions. Secondly, the $B\,^3\Sigma_u^-$, $v = 0$ level can be probed in more than one band, each with a different spacing of the rotational and fine-structure lines. The present measurements thus yield three independent sets of $B\,^3\Sigma_u^-$, $v = 0$ predissociation widths.

9.2 Experimental

9.2.1 Amsterdam setup and measurements

Two different spectroscopic techniques were applied for the investigation of the (0,0) Schumann-Runge band absorbing in the deep-UV. In both configurations a pulsed Titanium:Sapphire laser system is employed, the output of which is frequency-converted to its 4$^{\text{th}}$ harmonic to reach deep-UV wavelengths. This laser source has a bandwidth of 0.003 cm^{-1} and is tunable in the relevant range near 202 nm. All spectra were recorded at rather moderate laser pulse energies of less than 0.15 mJ/pulse; in the CRD experiments only a minute fraction of this energy is coupled into the cavity. Further details were given in Sneep *et al.*[39]

Cavity ring-down spectroscopy (CRDS) was performed in a cell of length 80 cm and a diameter of 1 cm, similar as in a previous study on one of the weaker visible band systems.[148] The optical cavity, spanning the entire cell length, is formed by two reflective mirrors with R $\approx$ 97 % in the range 197 – 203 nm and radius-of-curvature 1 m. CRD-recordings were performed at gas pressures in the range 30 – 300 mbar, where the pressure was on-line monitored on a baratron. The methods for monitoring and evaluating the CRD-transients, and retrieving the absorption spectrum were described previously.[39]

Laser-induced fluorescence measurements were also performed at pressure conditions of 30 – 300 mbar in a static gas cell. Fluorescence is collected by a mirror-lens system and filtered by a number of colored filters transmitting a broad wavelength band near 300 nm, where fluorescence originating in the $O_2\,B\,^3\Sigma_u^-$, $v' = 0$ state is expected. In view of power fluctuations during a scan the LIF-spectra are normalized to deep-UV-laser intensity probed on a photodiode.

Absolute wavelength calibration, in particular for the collisional shift measurements, was performed by using an ATOS wavelength meter, giving an accuracy of 200 MHz or 0.006 cm^{-1} at deep-UV wavelengths. Relative frequency spacings as well as linewidths were determined by comparing to transmission fringes of an etalon, yielding an even better precision on a relative scale.

9.2.2 SRI setup and measurements

The $B\,^3\Sigma_u^-$, $v = 0$ LIF bands were recorded as a byproduct of previously reported measurements of the higher vibrational levels in the $B\,^3\Sigma_u^-$ state.[167] The experimental details relevant to those measurements are given in Dooley *et al.*[167] and details

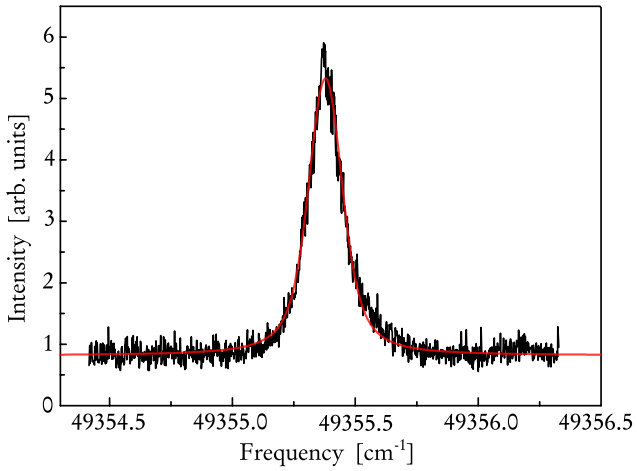

Figure 9.1 – *(color online) Spectral recording of the single rotationally resolved P(1) line of the $B^3\Sigma_u^- \leftarrow X^3\Sigma_g^-$ (0,0) band in $^{16}O_2$ at 38 mbar. Detection by LIF.*

of the general technique and analysis a given in Cosby *et al.*,[169] so only the general features of the experiments are summarized here. Two laser beams are used in the SRI configuration: (1) a strong pump laser (4 mJ at 280 nm) dissociates O_3 in a 2 % mixture of O_3 in He at 40 mbar to produce vibrationally excited O_2 and (2) a co-linear, temporally delayed (10 – 30 μs), weak (0.5 – 5 μJ), tunable probe laser excites the $B\,^3\Sigma_u^- \leftarrow X\,^3\Sigma_g^-$ transition in a single photon absorption from one of the excited vibrational levels. The O_2 $B\,^3\Sigma_u^-$ fluorescence is monitored by a photomultiplier, again after transmission through a filter centered at 350 nm (FWHM = 50 nm). The (0,19) and (0,20) bands were probed using the fundamental of the LPD3000E laser operating with Exalite 428 or Coumarin 440 dye and wavelength calibrated by simultaneously recording the Te_2 absorption spectrum. The (0,10) band was probed using the 2nd harmonic of this laser operating with Rhodamine 6G dye and the fundamental was wavelength calibrated by simultaneously recording the LIF spectrum of I_2 vapor.

9.3 Pressure effects

Both pressure and collisional effects on the one hand and predissociation phenomena on the other give rise to line broadening on individual spectral lines. The analysis of these phenomena is therefore intertwined, and at the same time complicated by the fact that each spectral structure consists of three unresolved spin-components. The $P_1(1)$ transition is a fortunate exception to this rule; it appears as a single resolved fine structure-component probing the $N = 0, J = 1, F_1$ fine-structure level.[40] A systematic study was performed of the line broadening of this single component. An example of a spectral recording, using the LIF technique at a pressure of 38 mbar,

is shown in Fig. 9.1. Similar recordings were performed in the pressure range 0 - 300 mbar.

The line shapes of these recordings were analyzed taking into account that they all undergo Doppler broadening, which for the O_2 molecule at 200 nm amounts to $\Delta_D = 0.107\,cm^{-1}$ (FWHM). A Gaussian function of width Δ_D was convolved with a Lorentzian function of width Γ_L and the deviations from the resulting function were minimized in a fitting routine to extract the Lorentzian contribution to the line broadening. The resulting values from this numerical procedure to derive a value for the total Lorentzian contribution Γ_L are plotted in Fig. 9.2. Physically this Γ_L represents the combined effect of predissociation and collisional broadening. Both phenomena cause homogeneous line broadening and a Lorentzian line shape. A mathematical property of Lorentzian functions is the simple rule of additivity of their widths upon convolution, while the convoluted function is again a Lorentzian.

This makes it possible to disentangle the contributions of both physical phenomena in a simple manner: the slope in Fig. 9.2 represents the collisional broadening effect, assumed to be linear in pressure p, while the intercept at $p = 0$ yields the value for the predissociation broadening Γ_{pred}. A linear fit to the pressure-dependent data, using the function:

$$\Gamma_L = \Gamma_{pred} + \Gamma_{col}\, p \tag{9.1}$$

yields a value for the predissociation broadening:

$$\Gamma_{pred} = 0.097 \pm 0.002\,cm^{-1} \tag{9.2}$$

for the $v' = 0$, $N = 0$, $J = 1$ state, and a value for the collisional parameter for the same state:

$$\Gamma_{col} = (2.2 \pm 0.3) \times 10^{-4}\,cm^{-1}/mbar. \tag{9.3}$$

The same spectral recordings for the singly resolved $P_1(1)$ line in the (0,0) band were also used to assess collisional shifts in the Schumann-Runge band system. In the fits line centers were determined as displayed in Fig. 9.2. From a fit of the slope to the data in Fig. 9.2 a collisional shift parameter was determined at:

$$\delta_{shift} = (-7 \pm 2) \times 10^{-5}\,cm^{-1}/mbar. \tag{9.4}$$

9.4 Fine-structure dependent predissociation the (0,0) band

In Fig. 9.3 typical recordings of the P(3) line of the (0,0) band in $^{16}O_2$ are displayed, obtained by LIF and by CRD. Both spectra were recorded at a pressure of 300 mbar. Spectra of the P(5) triplet were obtained in the same way. In P(N) transitions for higher N values as well as in the R-branch the spin-splittings are too small for the intensities for the three individual components to be disentangled.

The rationale of a comprehensive analysis, using the information contained in both spectra, is as follows. In both detection methods the linewidths of the individual fine-structure components are determined by Doppler broadening, collisional

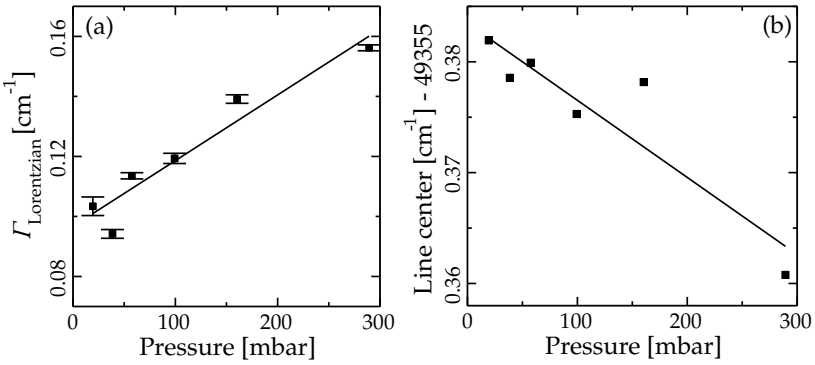

Figure 9.2 – *a) The combined effect of collisional broadening and predissociation as observed on the P(1) line of the $B^3\Sigma_u^- \leftarrow X^3\Sigma_g^-$ (0,0) band in $^{16}O_2$. Lorentzian contribution to the linewidth after deconvolution of the observed profile with a Doppler component (Gaussian profile) of 0.107 cm^{-1} (FWHM). b) Collisional shift effect as observed on the P(1) line of the $B^3\Sigma_u^- \leftarrow X^3\Sigma_g^-$ (0,0) band in $^{16}O_2$.*

broadening and predissociation broadening. Since the spectra were obtained from samples at 300 mbar in both cases the individual line shape and width of the F_i components is the same, while the relative intensities for the fine structure components will differ in both spectra. In the fitting procedures a Gaussian profile of a width fixed to the Doppler broadening of 0.107 cm^{-1} was convolved with three variable Lorentzian contributions $\Gamma(F_i)$. The Lorentzian components to the width represent a variable predissociation width and a constant contribution of 0.066 cm^{-1} (FWHM) associated with a pressure of 300 mbar; this value follows from the previous analysis on the $P_1(1)$ line and will finally be subtracted from the obtained fit results. The difference between the two detection methods is in the intensities; in fact we only use the information on the relative intensities between fine-structure components in each individual spectrum. Since CRD is a method probing direct absorption, the relative intensities for the spectral fine-structure components should follow the theoretical line strengths; hence in the fit on the CRD spectrum the relative intensities were kept fixed at the values as expected from the Hönl-London factors and room temperature Boltzmann factors. For the P(3) line that is $P_3(3)/P_1(3) = 0.427$ and $P_2(3)/P_1(3) = 0.683$ and for the P(5) line $P_3(5)/P_1(5) = 0.651$ and $P_2(5)/P_1(5) = 0.804$.

While CRD measures in fact direct absorption, and therewith probes the excitation oscillator strength, in LIF-detection excitation strength and fluorescence yield both affect the intensity. In the latter scheme the fluorescence intensity is reduced due to competition with predissociation. The collisional effects giving rise to the additional line broadening, as studied in the above for the P(1) line, may give rise to quenching of the fluorescence and affect the intensities obtained in the LIF study. However, that depends on the nature of the collisional processes and detailed information for such phenomena is lacking for the Schumann-Runge band systems. The

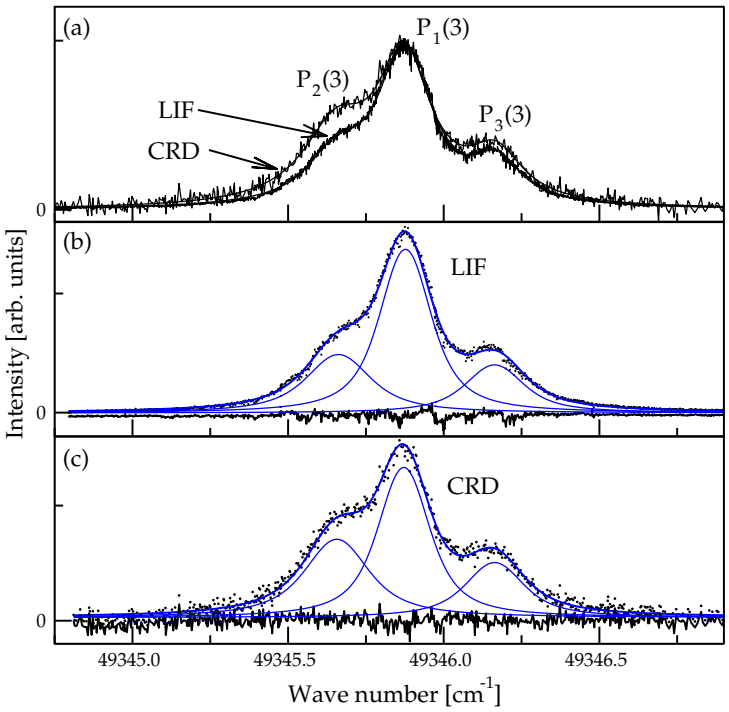

Figure 9.3 – *(color online) Spectral recordings of the three fine structure components of the P(3) line of the* $B^3\Sigma_u^- \leftarrow X^3\Sigma_g^-$ *(0,0) band in* $^{16}O_2$*, both by CRD spectroscopy and by LIF at a pressure of 300 mbar. Panel a) gives direct proof for the more rapid predissociation of* F_2 *and* F_3 *components, with respect to* F_1*. Panel b) shows the resulting fit for the spectral LIF profile using parameters* $\Gamma(F_i)$*, as described in the text. Panel c) shows the resulting fit to the CRD profile. In the lower panels the calculated contributions of each fine-structure component* F_i *are plotted, as well as residuals between experimental and calculated profiles.*

collisional effects may be related to elastic scattering, to rotational or vibrational energy transfer within the $B\,^3\Sigma_u^-$ state, or to collisional transfer to continuum states.

Considering the competition of predissociation and fluorescence, Fig. 9.3 shows in a qualitative but direct manner that the F_2 and F_3 components are more rapidly predissociated than the F_1 component. If it is assumed that the radiative lifetime is 50 ns,[169,172] then the fluorescence yield is on the order of 0.1 % for a predissociation width of 0.1 cm^{-1}. Thus the fluorescence rate k_{rad} is much smaller than the collisional decay rate k_{col} and the predissociation decay rate k_{pred}. Note that total decay rates k_{tot} relate to (Lorentzian) contributions Γ_L via $k_{tot} = k_{col} + k_{pred} + k_{rad} = 2\pi\Gamma_L$. Furthermore it can be shown that the relative fluorescence intensities $(F_i/F_j)_{LIF}$ can be expressed in terms of the relative absorption intensities $(F_i/F_j)_{ABS}$, via:

$$\left(\frac{F_i}{F_j}\right)_{LIF} = \left(\frac{F_i}{F_j}\right)_{ABS} \frac{k_j^{tot}}{k_i^{tot}} \tag{9.5}$$

where the $k_{i,j}^{tot}$ factors relate to the total decay rates of the excited states, including the collisional effects. Eq. (9.5) is valid, whether or not secondary fluorescence due to collision-induced inelastic scattering within the $B\,^3\Sigma_u^-$, v, N, J manifold plays a role.

The full information contained in both LIF and CRD spectra as displayed in Fig. 9.3, and similarly for the recording of the P(5) triplet, is used in one comprehensive fitting analysis, that is constrained by Eq. (9.5). Hence the line strengths in the CRD and LIF spectra follow different constraints in the combined fits. It should be noted that all statements on intensities hold for *integrated* intensities. The fits using a combined set of parameters for both traces are shown in the lower panels of Fig. 9.3. There the observed and calculated spectra are displayed, as well the calculated curves for the three fine-structure components. Also, displayed in a separate trace, are the deviations between observed and calculated spectra, demonstrating the quality of the procedure. Resulting values for $\Gamma_{pred}(F_i)$ from the combined fits are reduced by $0.066\,cm^{-1}$ to correct for the collisional broadening effect at 300 mbar.

9.5 Line broadening in the (0,10), (0,19) and (0,20) bands

At the very low pressure of O_3 (< 1 mbar) in the He buffer gas, pressure broadening of the $B\,^3\Sigma_u^- \leftarrow X\,^3\Sigma_g^-$ fluorescence spectra is negligible. The emission coefficient of the (0,20) band is 10^5 times larger than that of the (0,0) band. Those of the (0,19) and (0,10) bands are, respectively, factors of 3 and 40 times stronger than the (0,20). The essence of the experiment was to limit the power broadening in these SR bands, while retaining sufficient signal to noise to accurately measure the line profiles. To achieve the very low power densities required for these measurements, the LPD3000E was operated without its preamplifier and with a severely attenuated amplifier, at the cost of some degradation in the laser linewidth. In addition, the output beam was expanded by a factor of three or more to keep the effect of power broadening of the SR transitions to less than 10 % for transitions terminating in the lower rotational levels. At the required low power levels, the (0,19) spectra yielded the poorest signal-to-noise ratios of the three bands. Probe laser bandwidths, estimated from the features in the wavelength calibration spectra, an external etalon, and from analysis of the LIF line profiles, were approximately $0.04\,cm^{-1}$ for the (0,19) band, $0.1\,cm^{-1}$ for the (0,20) band, and $0.07\,cm^{-1}$ for the (0,10) band. In combination with the approximately room temperature Doppler broadening, consistent with the rotational temperature of the rotational line intensities, the total inhomogeneous (Gaussian) contributions to the LIF peak shapes were $0.071\,cm^{-1}$, $0.122\,cm^{-1}$, and $0.125\,cm^{-1}$ for the (0,19), (0,20), and (0,10) bands, respectively. Spectra are shown in Fig. 9.4 for the P- and R-branch lines in each band terminating in $N' = 6$.

Analysis of the LIF spectra followed the procedure given by Dooley *et al.*[167] using the Voigt line shape defined by equations (4) – (7) of reference.[169] These LIF line shape equations include the dependence of fluorescence intensity on lifetime described by Eq. (9.5) above. The values of Γ_L obtained in the line fits, following a

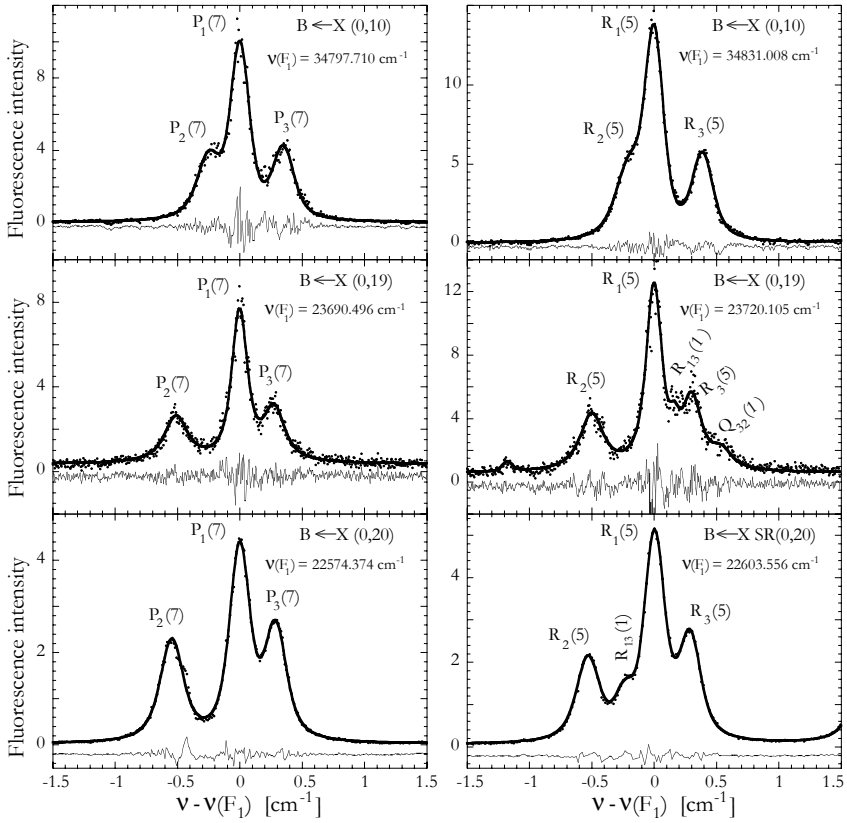

Figure 9.4 – *SRI LIF spectral recordings (points) of the P- and R- branch lines terminating in the $N' = 6$ levels of $B^3\Sigma_u^-$, $v = 0$ for the (0,10), (0,19), and (0,20) Schumann-Runge bands. Fits to the transitions, including several weak satellite transitions, are given by the thick lines. Thin lines at the bottom of each spectrum show the residuals in the fits.*

small correction for saturation broadening, are reported here as the predissociation level widths Γ_{pred}.

The determination of Γ_{pred} in the (0,20) band encompassed all main P- and R-branch lines with $N' < 26$. In the (0,10) band, coverage of the two main branches was complete for $N' < 18$, although the F_1 and F_2 components are effectively blended in both the P- and R-branches for $N' < 16 - 20$. Coverage of the (0,19) band was much less extensive, with both P- and R-branch lines measured only at $N' = 2$, 4, 6, and 14. Γ_{pred} are reported here for $B\,^3\Sigma_u^-$, $v = 0$ at $N' = 0 - 20$. From the combination of three bands and two branches for most levels, each of the values represents the average of at least three independent measurements, with 6 measurements contributing to most of the averages. For each of the bands, the differences in Γ_{pred} determined from the P and R lines terminating in a given N' were randomly distributed over

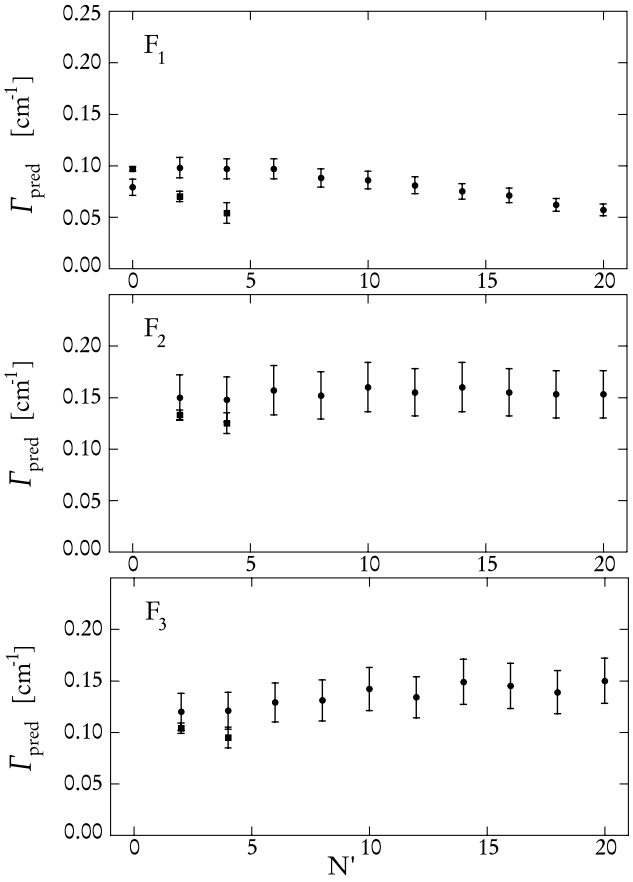

Figure 9.5 – *Predissociation widths Γ_{pred} measured for the $B^3\Sigma_u^-$, $v = 0, N, F_i$ fine structure levels in O_2. Points = SRI. Squares = Amsterdam.*

a range of ± 10 %. For the F_1 components, the differences in Γ_{pred} among the three bands were also consistent to within ± 10 %. However, for the F_2 and F_3 levels, the values of Γ_{pred} determined from the three bands showed systematic deviations for levels $N' < 12$, where the values of Γ_{pred} from the (0,19) band were consistently larger by 26 % for the F_2 levels and 29 % for the F_3 levels, than those obtained from the other two bands. Apart from the lower signal to noise ratios in the (0,19) band and its relatively scant coverage, no specific reason for the larger Γ_{pred} values in this band could be identified. Consequently, we consider these larger values to be characteristic of the measurement errors and used all three bands to determine the average values of Γ_{pred} and their uncertainties for the $B\,^3\Sigma_u^-$, $v = 0$ levels. The resulting predissociation level widths Γ_{pred} are shown by the points in Fig. 9.5, where the error bars represent one standard deviation in the uncertainty of the values.

9.6 Discussion and conclusion

There is a vast literature[134,156–169] on the predissociation in the Schumann-Runge bands reflecting the importance of oxygen dissociation from a theoretical as well as an atmospheric perspective. The present findings on a fine-structure dependent predissociation rate are well documented and are supported by the theoretical models of Lewis *et al.*[134] and Tong *et al.*,[166] showing that the F_1 is the least predissociated and that the F_2 component is the most strongly affected by predissociation.

A study of the lowest vibrational level of the $B\,^3\Sigma_u^-$ state in oxygen has been performed by combining input from independent measurement schemes executed at different laboratories. In their combination the procedures represent the state-of-the-art and the resulting values for the predissociation widths of the fine-structure levels in $B\,^3\Sigma_u^-$, $v = 0$ form benchmark results for testing theoretical models of predissociation in O_2. Previously discrepancies between rather strongly deviating findings obtained with different techniques in different laboratories have been addressed before with the aim of resolving them.[134,167]

The present investigations produce reasonable, but yet not perfect, agreement between findings of different laboratories. The remaining deviations may be considered to represent the true level of experimental accuracies, and may be associated with the different compromises troubling the experimental approaches: the requirement of relatively high pressures in the Amsterdam setup, resulting in relatively large collisional contributions to the linewidths, and the delicate balance between signal intensity and saturation in the SRI experiments, and the necessary methods of deconvolution in both experiments.

We note that improved use of the narrowband laser source could be made when detecting in the collision-free and Doppler-free conditions of a molecular beam; in such case no deconvolution nor extrapolation to zero pressure would be required to determine predissociation linewidths. Unfortunately, attempts to observe LIF signals in the B – X (0,0) band in a molecular beam failed thus far, due to the extremely small Franck-Condon factor combined with the small fluorescence rate.

The present value for the collisional broadening constitutes an independent verification at low and atmospherically relevant pressures of the results of the Canberra group, first at high pressures up to 60 bar,[170] and subsequently at sub-atmospheric pressures.[171] The resulting averaged value of $0.208 \pm 0.004\,\mathrm{cm^{-1}/bar}$, measured for excited states with $v' = 2 - 15$, is in excellent agreement with the present finding. The result on the collisional shift, here established for $v' = 0$ is in agreement with the finding of Dooley *et al.*[171] of $-5.6 \pm 0.8 \times 10^{-5}\,\mathrm{cm^{-1}/mbar}$ for vibrational levels $v' = 13 - 15$.

Acknowledgments

The authors wish to thank B. R. Lewis (Canberra) for discussions and advise. The Netherlands Foundation for Fundamental Research of Matter (FOM) and the Space Research Organisation Netherlands (SRON) are acknowledged for financial sup-

port. The stay of G.R. Wu (Dalian Institute of Chemical Physics) at the Laser Centre VU Amsterdam is supported by a collaborative project (98-CDP034) between the Netherlands Royal Academy of Sciences (KNAW) and the Chinese Academy of Sciences (CAS). The measurements at SRI were partially supported by a grant from the Atmospheric Sciences Division of the (US) National Science Foundation.

Zusammenfassung

Die vorliegende Doktorarbeit dokumentiert experimentelle Forschung im Bereich der Laserphysik und Laserspektroskopie. Das ursprüngliche Ziel war der Bau eines Lasersystem, welches benutzt werden sollte, mit Hilfe resonanzverstärkter Vierwellenmischung schmalbandiges, extrem ultraviolettes (XUV) Licht herzustellen. Während die Methode in einem Experiment erfolgreich demonstriert wurde (vergleiche Kapitel 6), verlagerte sich das Hauptinteresse der ausgeführten Arbeit hin zu Präzisionsmetrologie im tief ultravioletten (UV) Spektralbereich.

Das Lasersystem, welches zu Anfang des Projekts konstruiert wurde, ist ein injektions-geseedetes Oszillator-Verstärkersystem. Der gepulste Arbeitsmodus wird durch Gainswitching in einer Lasercavity mit niedriger Finesse erreicht. Um die erzeugten Pulse weiter zu verstärken, ist ein externer Multipass-Verstärker verfügbar. Damit vereint das Lasersystem Eigenschaften wie hohe Spitzenintensitäten in Pulslängen von typischerweise 20 ns mit relativ schmalen Linienbreiten von etwa 20 MHz. Es eignet sich zur effizienten Frequenzkonversion zu höheren harmonischen für hochaufgelöste Spektroskopie im ultravioletten und tief-ultraviolettem Wellenlängenbereich.

Um darüber hinaus Präzisionsmetrologie zu betreiben, wurden zwei Methoden zur absoluten Frequenzkalibration des kontinuierlichen (CW) Injektionsseedlichts implementiert: Dopplerfreie Sättigungsspektroskopie an einer Iodzelle und direkte Kalibration mit Hilfe eines Femtosekunden-Frequenzkammes. Diese beiden von einander unabhängigen Optionen zur absoluten Frequenzmessung drängten die Frage auf, ob die Laserpulse dieselbe Mittelfrequenz aufweisen wie das kalibrierte Seedlicht. Um dies zu untersuchen und gegebenenfalls Maßnahmen zur Kontrolle oder Kompensation möglicher Frequenzunterschiede ergreifen zu können, wurde eine als „Chirpanalyse“ bekannte Technik angewandt, welche als Einzelpulsmethode funktioniert und in den Kapiteln 2 und 5 detailliert beschrieben ist. Die Chirpanalyse wurde schließlich „online“ implementiert, d.h. sie wird zeitgleich mit der spektroskopischen Messung durchgeführt und ermöglicht so das unmittelbare Einbeziehen eventueller Frequenzoffsets. Diese Herangehensweise hat die Frequenzkalibration entscheidend verbessert. Genauigkeiten im Megahertzbereich werden erreicht und stehen nun in einem breiten durchgehenden Wellenlängengebiet zur Verfügung.

Neben präziser Laserfrequenzmessung wurde eine spezielle Methode zur Reduzierung von Dopplerverschiebungen in gekreuzten Atom/Molekular- und Laserstrahlexperimenten entwickelt, welche in Kapitel 3 vorgestellt wird. Die Technik ba-

siert auf der Optimierung der räumlichen Überlagerung zweier gegenläufiger Laserstrahlen gleicher Frequenz, die Teil eines Sagnac-Interferometers sind. In perfekter Justierung zeigt der Ausgang des Interferometers einen „Darkfringe". Hier unterliegen beide Laserstrahlen identischen Dopplerverschiebungen, welche jedoch entgegengesetzte Vorzeichen haben. Kleinste Abweichungen von perfekt antiparallelem Verlauf werden durch Interferenzstreifen angezeigt. Experimentelle Unsicherheiten, die aus Dopplerverschiebungen an gekreuzten Atom/Molekularstrahl- und Laserstrahlaufbauten hervorgehen, konnten so unter das Niveau von Unsicherheiten reduziert werden, die aus der Charakteristik des Lasersystems resultieren. Die Sagnac-Methode is hilfreich, wo immer klassische Doppler-freie Techniken nicht oder nur sehr schwer zur realisieren sind, z.B. an Übergängen im tief-UV oder Vakuum-UV, welche hohe Sättigungsintensitäten aufweisen. Darüber hinaus sind Doppler-freie Methoden unter bestimmten Umständen nur Doppler-frei im Sinne von nicht Doppler-verbreitert, unterliegen aber dennoch einer Dopplerverschiebung wenn sie auf Ensembles mit nicht isotropischer Geschwindigkeitsverteilung, z.B. auf Atom- oder Molekularstrahlen, angewandt werden. In solchen Fällen beruht die Genauigkeit des Ergebnisses auf der Qualität des räumlichen Überlapps zwischen beiden gegenläufigen Laserstrahlen. Die Sagnac-Methode zur Reduzierung von Dopplerverschiebungen wird an Ein- und Zweiphotonspektroskopien gezeigt.

Die Kombination von schmaler Linienbreite des Lasers, gepulstem Arbeitsmodus für effiziente Erzeugung von harmonischen Frequenzen, kontrollierter „Chirp"-Charakteristik, sowie präzisen absoluten Frequenzstandards machten Genauigkeiten von unter 10^{-9} in einem großen Spektralbereich verfügbar. Seine weite Durchstimmbarkeit und absolute Frequenzgenauigkeit zeichnen das Lasersystem aus und machen es zu einem vielseitig einsetzbaren Instrument der Präzisionsspektroskopie. Im Rahmen der Doktorarbeit wurde vor allem die vierte harmonische Oberfrequenz benutzt, u.a. für Cavity-Ring-Down-Spektroskopie, in Fluoreszenzspektroskopien, für Doppler-freie Zwei-Photonen-Spektroskopie sowie für resonanzverstärkte Vierwellenmischung.

Folgende Experimente wurden durchgeführt und in dieser Arbeit beschrieben: In Kapitel 2 wird ausführlich auf das Titan-Saphir-Lasersystem (Ti:Sa) eingegangen. Insbesondere der Oszillator wurde untersucht und quantitativ charakterisiert. Im Hinblick auf Anwendungen für Frequenzmetrologie richtete sich das Interesse besonders auf den zeitlichen Verlauf der Momentanfrequenz des gepulsten Lichts. Es wurden Methoden zur Beeinflussung von Frequenzunterschieden zwischen gepulstem und kontinuierlichem Seedlicht aufgezeigt und angewandt. Der Einfluß des Multipass-Verstärkers auf die zeitliche und spektrale Pulsform sind ebenfalls gemessen worden.

Im dritten Kapitel wird die Sagnac-Methode zur Veringerung von Dopplerverschiebungen beschrieben und demonstriert. Der $6s^2 \rightarrow 6s30p_{3/2}$ $J = 1$ Ein-Photonen-Übergang im Ytterbiumatom bei 199 nm wurde mit Hilfe von Laser-induzierter Fluoreszenzdetektion gemessen, und der $4p^6 \rightarrow 4p^5 5p[1/2]_0$ Zwei-Photonen-Übergang in Krypton (bei 2×212 nm) wurde unter Verwendung von Mehrphotonenio-

nisation und Time-of-Flight-Extraktion kalibriert. Experimentelle Unsicherheiten wurden auf einen Bereich von 6×10^{-10} reduziert, wo systematische Effekte resultierend aus den Lasereigenschaften überwiegen.

In Kapitel 4 wird die Frequenzkalibration der $3s^2 \rightarrow 3s4p$ Singlettlinie in Mg I nahe 202.5 nm beschrieben. Motiviert wurde dieses Experiment zum einen aus einem technischen Interesse, die höchstmögliche Präzision unter Verwendung eines Nanosekundenlasers zu erreichen. Zum anderen ist diese Linie ein Kandidat zur Implementierung in Many-Multiplett-Methoden zum Vergleich mit Quasar-Absorptions-Spektren mit hoher Rotverschiebung, welche zur Bestimmung einer möglichen Änderung der Feinstrukturkonstante α herangezogen werden.[1] Dieses Forschungsfeld benötigt genauere Linienpositionen, welche als Referenzlinien bei Abwesenheit der Rotverschiebung dienen.[2]

In Kapitel 5 geht es um Frequenzmetrologie am EF $^1\Sigma_g^+ \leftarrow$ X $^1\Sigma_g^+$ (0,0) Zwei-Photonen-Übergang in molekularem Wasserstoff und einigen seiner Isotopomeren (HD, D_2). Der EF-Zustand ist deshalb von besonderem Interesse, weil verschiedene und jeweils sehr genaue Messungen von Ionisations- und Dissoziationspotentialen relativ zum EF-Doppel-Zustand durchgeführt wurden bzw. werden können. Demzufolge wird ein genau bekannter Wert der Übergangsfrequenz zum EF-Zustand ebenfalls die Genauigkeit der experimentell bestimmten Ionisations- und Dissoziationspotentiale verbessern, was wiederum typische Testgrößen sind, die in *ab initio* Modellen berechnet werden können. Die erreichte Präzision der gemessenen Energien für die untersuchten EF $\leftarrow$ X Linien ist 10^{-9}.

Unter Verwendung der vierten harmonischen des Ti:Sa-Lasers bei 212.5 nm wurde resonanzverstärkte Vierwellenmischung mit Hilfe der Zwei-Photonen-Resonanz $4p^6 \rightarrow 4p^5 5p[1/2]_0$ in Krypton demonstriert. In Kapitel 6 wird das Experiment beschrieben, in welchem die Phasenanpassung für die Summenfrequenzmischung in einem gepulsten Gasjet mittels nicht kollinear justierter Laserstrahlen erreicht wird. Dies erlaubt die Auswahl der gewünschten Wellenlänge bei etwa 91 nm mit einem in Größe und Position verstellbaren Spalt statt mit einem optischen Gitter. Mit Hilfe dieser Methode wurden Linien des b′ $\leftarrow$ X (8–0) und des b $\leftarrow$ X (12–0) Bandes in molekularem Stickstoff sowie des B $\leftarrow$ X (19–0) Lymanbandes in molekularem Wasserstoff kalibriert. Letztere Wasserstofflinien sind Teil einer Datenbank von H_2-Spektren, welche benutzt werden können um eine mögliche Veränderung des Elektron-Proton Massenverhältnisses im Laufe der Geschichte des Universums untersuchen zu können.[3]

In Kapitel 7 wird ein Experiment zur Cavity-Ring-Down-Spektroskopie (CRDS) bei tief-ultravioletten Wellenlängen zwischen 204 nm – 197 nm vorgestellt — den kürzesten Wellenlängen bei denen CRDS bisher durchgeführt wurde. Extinktionskoeffizienten wurden für einige Gase bestimmt. Ferner wurden einige Schumann-Runge-Bänder in molekularem Sauerstoff gemessen, wobei deren Feinstruktur aufgelöst sowie Extinktionskoeffizienten des Herzberg-Kontinuums bestimmt wurden.

Eine detailierte spektroskopische Analyse der Schumann-Runge-Bänder (2,0), (1,0), (0,0), (2,1) in $^{16}O_2$ sowie der Bänder (1,0), (0,0) in $^{18}O_2$ wird in Kapitel 8 be-

sprochen. Die hohe Auflösung der Spektroskopie gestattete die Verbesserung der Genauigkeit der Werte für die Molekülkonstanten. Da das Schumann-Runge-System den ersten Dipol-erlaubten Übergang im Sauerstoffmolekül darstellt, spielt es eine wichtige Rolle bei der UV-Absorption in der Erdatmosphäre. Präzise Kenntnis der Molekülkonstanten wird für Berechnungen des Strahlunghaushaltes in der Atmosphere benötigt.

In Kapitel 9 wurden die Linien der Feinstruktur des Schumann-Runge-Bandes (0,0) genauer untersucht. Aufgrund des hohen Auflösungsvermögens des Lasersystems konnten Druckverbreiterung und -verschiebung quantifiziert werden. Aus einer kombinierten Fluoreszenz- und CRD-Spektroskopie konnten Feinstruktur abhängige Prädissoziationsraten für den angeregten Zustand $B\,^3\Sigma_u^-$, $v = 0$ extrahiert werden.

Die Vielfalt der demonstrierten Anwendungsmöglichkeiten und seine vorteilhaften Eigenschaften — weite Durchstimmbarkeit, schmale Linienbreite sowie die Verfügbarkeit hochpräziser Mittel der Frequenzkalibration — zeigen, daß das konstruierte Lasersystem ein vielseitig einsetzbares Werkzeug im Spektroskopielabor ist.

Diep ultraviolette frequentiemetrologie met een smalbandige titaan-saffier laser

Dit proefschrift beschrijft onderzoek op de gebieden van laserfysica en laser spectroscopie. Een laseropstelling is ontworpen en opgebouwd aanvankelijk om extreem ultraviolet (XUV) licht te produceren via resonantie-versterkte 'four-wave-mixing' in een gepulste gasjet. Terwijl die methode in een experiment succesvol is uitgevoerd en in hoofdstuk 6 beschreven is, veranderde het doel van het onderzoek echter naar precisiemetrologie in het diepe ultraviolette golflengtegebied.

Het lasersysteem, dat in het begin van de promotieperiode werd geconstrueerd, is een injection-seeded oscillator-versterkersysteem gebaseerd op het lasermateriaal titaan-saffier. De gepulste werking wordt bereikt door gain-switching in een optische trilholte met lage finesse. De lichtpulsen worden vervolgens versterkt in een externe multipass-versterker. Hiermee verenigt deze laser eigenschappen als hoge piekintensiteit (pulslengten van ongeveer 20 ns) met smalle spectrale breedtes (≈ 20 MHz) en is daardoor geschikt voor efficiënte conversie naar hogere harmonische frequenties, toe te passen in hoge resolutie spectroscopie in het ultraviolette en diep ultraviolette golflengtegebied.

Twee verschillende precisie-metrologische methoden voor absolute frequentie-ijking werden gebruikt: Dopplervrije verzadigingsspectroscopie aan jodium moleculen en directe frequentiemeting met een frequentiekam. Deze twee opties voor preciese frequentiebepaling maakten het noodzakelijk om te testen, of de centrale frequentie van de uitgaande pulsen gelijk is aan die van het seedlicht. Door toepassing van een techniek gebaseerd op Fourieranalyse kunnen frequentieverschillen voor elke afzonderlijke puls worden gemeten.[15,16] Uiteindelijk werd deze "chirp-analyse" online geïmplementeerd, en simultaan met de spectroscopie uitgevoerd. Ook zijn methoden gedemonstreerd om eventuele frequentieverschillen tussen seed en gepulst licht bij te regelen of te beperken. Deze benadering heeft de absolute frequentiemetingen flink verbeterd. Nauwkeurigheden op het MHz-niveau worden zo behaald en zijn toepasbaar over een breed golflengtegebied.

Naast precisiemetingen van laserfrequenties werd een speciale methode ontwikkeld om Doppler-verschuivingen in experimenten met gekruiste atoom/molekuul- en laserbundels te minimaliseren. Dit wordt in hoofdstuk 3 beschreven. De techniek is gebaseerd op de optimalisatie van de ruimtelijke overlap van twee tegen elkaar in lopende laserbundels met dezelfde frequentie; beide bundels maken on-

derdeel uit van een Sagnac-interferometer. Optimale uitlijning correspondeert dan met een “dark-fringe” in het interferentiepatroon; beide bundels ondergaan dezelfde Doppler verschuiving, echter met verschillend van teken. Kleine afwijkingen van perfecte overlap induceren een meetbare wijziging in het interferentiepatroon. Met deze methode is het mogelijk experimentele onzekerheden, die door Dopplereffecten tot stand komen, te verkleinen tot onder het niveau van andere onzekerheden, samenhangend met het lasersysteem en de opstelling. De Sagnacmethode is nuttig in die gevallen waar klassieke Dopplervrije technieken niet werken, of moeilijk te realiseren zijn, bij voorbeeld in het geval van overgangen in het UV of diepe-UV waar verzadigingsintensiteiten moeilijk te bereiken zijn. Bovendien zijn Dopplervrije methoden onder bepaalde omstandigheden alleen Dopplervrij in de zin van niet Doppler verbreed; een Doppleropschuiving kan wel optreden als sprake is van gas samples met een niet-isotrope snelheidsverdeling, zoals b.v. in atoom- en molekuulbundels. In zulke gevallen is de mate van ruimtelijke overlap van de twee tegen elkaar in lopende laserbundels bepalend voor de nauwkeurigheid van de metrologie. De voorgestelde Sagnacmethode wordt gedemonstreerd in zowel één-foton en twee-foton overgangen.

Door de combinatie van smalle bandbreedte van de laser, de "chirp-metingen, en preciese absolute frequentiestandaarden (verzadigingsspectroscopie of frequentiekam) kunnen nauwkeurigheden beneden 10^{-9} behaald worden in een breed spectraal gebied. De brede verstembaarheid van het lasersysteem en zijn absolute nauwkeurigheid maken het een veelzijdig instrument met velerlei toepassingen op het gebied van spectroscopie. Gedurende het promotieonderzoek is vooral de vierde harmonische gebruikt, onder andere voor cavity ring-down spectroscopie, fluorescentie spectroscopie, Dopplervrije twee-foton spectroscopie, en voor resonantieversterkte ’four-wave-mixing’.

De volgende experimenten zijn uitgevoerd en in dit proefschrift beschreven: In Hoofdstuk 2 wordt uitgebreid op het titanium:saffier lasersysteem ingegaan. Vooral de oscillator werd onderzocht en kwantitatief gekarakteriseerd. Met het oog op toepassingen voor frequentiemetrologie werd vooral aandacht besteed voornamelijk aan de tijdsafhankelijke frequentie-evolutie van de laserpulsen. Methoden om frequentieverschillen tussen seed- en gepulst licht te meten werden ontwikkeld en toegepast. Uiteindelijk is gekwantificeerd hoe de externe versterking de temporele en spectrale pulsvorm beïnvloedt.

Hoofdstuk 3 beschrijft de Sagnacmethode voor de minimalisatie van Dopplerverschuivingen. Ter demonstratie werd de $6s^2 \rightarrow 6s30p_{3/2}\, J = 1$ één-foton overgang in atomair ytterbium in de buurt van 199 nm gemeten met behulp van detectie van laser geïnduceerde fluorescentie; verder werd de twee-foton overgang $4p^6 \rightarrow 4p^5 5p[1/2]_0$ in krypton (vlak bij 2×212 nm) via multi-foton ionisatie en time-of-flight extractie gecalibreerd. Experimentele onzekerheden werden tot een niveau van 6×10^{-10} gereduceerd, waarbij systematische effecten gerelateerd aan de laser overheersen.

In hoofdstuk 4 wordt een nauwkeurige frequentiecalibratie van de singlet lijn

$3s^2 \rightarrow 3s4p$ in atomair magnesium ($\approx$ 202.5 nm) beschreven. Naast een technologisch doel om de best mogelijke precisie bij gebruik van een nanosecondenlaser te bereiken, ligt de motivatie van dit experiment in het gebruik van deze spectraallijn bij de detectie van een mogelijke verandering van de fijnstructuurconstante α op een kosmologische tijdschaal. De 4p resonantielijn van Mg komt voor in de lijst van Berengut *et al.*[2] van te calibreren spectraallijnen benodigd voor uitbreiding van de 'many-multiplet' methode.[1]

Hoofdstuk 5 beschrijft frequentiemetrologie aan de EF $^1\Sigma_g^+ \leftarrow$ X $^1\Sigma_g^+$ (0,0) twee-foton overgang in moleculair waterstof en zijn isotopische varianten HD, en D_2. De EF toestand is van speciale interesse omdat een aantal nauwkeurige bepalingen van ionisatie- en dissociatielimiet afhangen van de ligging van de EF toestand. De waarden van de ionisatie- en dissociatielimieten in waterstof lenen zich voor tests van *ab initio* moleculaire berekeningen.

Door gebruik van de vierde harmonische van de Ti:Sa laser bij 212.5 nm werd resonantieversterkte 'four-wave-mixing' met behulp van de twee-foton overgang $4p^6 \rightarrow 4p^5 5p[1/2]_0$ in krypton gedemonstreerd. In hoofdstuk 6 wordt een schema voor som-frequentie-menging beschreven, waarbij via niet-collineaire 'phase-matching' de gewenste somfrequentie wordt gescheiden van de andere frequentiecomponenten door middel van een spleet in plaats van een tralie. Het geproduceerde licht met een golflengte van $\approx$ 91 nm werd gebruikt om lijnposities en -breedtes in de b′ $\leftarrow$ X (8–0) en b $\leftarrow$ X (12–0) banden van moleculair stikstof te meten. Bovendien werden lijnen uit de B $\leftarrow$ X (19–0) Lyman band in moleculair waterstof gecalibreerd. Deze lijnposities zijn opgenomen in een database van H_2 spectra, die gebruikt kunnen worden om eventuele veranderingen van de proton-elektron–massaverhouding op de kosmologische tijdschaal van het universum te detecteren.[3]

Hoofdstuk 7 beschrijft een experiment, waarin cavity-ring-down-spectroscopie is toegepast bij de tot nu toe kortste golflengtes, tussen 204 nm en 197 nm. Extinctiecoëfficiënten voor een aantal gassen werden bepaald. Verder werden spectra van enkele Schumann-Runge-banden in moleculair zuurstof gemeten, waarbij dankzij de smalle lijnbreedte van het lasersysteem de fijnstructuur werd opgelost. Bovendien werden extinctiecoëfficiënten voor het Herzberg-continuum bepaald.

Een gedetailleerde spectroscopische analyse van de gemeten Schumann-Runge-banden (2,0), (1,0), (0,0), (2,1) in $^{16}O_2$ en de banden (1,0), (0,0) in $^{18}O_2$ wordt behandeld in hoofdstuk 8. Dankzij de hoge resolutie en de precisie frequentiemetingen konden nauwkeurige waardes van de moleculaire constanten bepaald worden. Omdat de Schumann-Runge banden de eerste dipool-toegestane overgangen in zuurstof representeren, zijn ze van groot belang voor de absorptie van ultraviolet licht in de aardse atmosfeer.

In hoofdstuk 9 worden de fijnstructuur opgeloste lijnen in de (0,0) Schumann-Runge band in detail bestudeerd. Door de smalle bandbreedte van de laser kunnen botsingseffecten (verbreding en verschuiving) gequantificeerd worden. Door combinatie van absorptie- (cavity-ring-down) en fluorescentiemetingen konden fijnstructuurafhankelijke predissociatie vervalsnelheden in de B $^3\Sigma_u^-$, $v = 0$ toestand worden

bepaald.

De diversiteit van gedemonstreerde toepassingen en de voordelige karakteristieken — brede verstembaarheid, smalle bandbreedte en de beschikbaarheid van methoden voor ultranauwkeurige frequentieijking — laten zien, dat de ontwikkelde titaan-saffier laser en veelzijdig toepasbaar instrument is in een spectroscopisch laboratorium.

Bibliography

[1] J. K. Webb, V. V. Flambaum, C. W. Churchill, M. J. Drinkwater and J. D. Barrow, 'Search for time variation of the fine-structure constant'. *Phys. Rev. Lett.* **82**, 884 (1999).

[2] J. C. Berengut, V. A. Dzuba, V. V. Flambaum, M. V. Marchenko and J. K. Webb, 'Laboratory spectroscopy and the search for space-time variation of the fine structure constant using QSO spectra', arXiv:physics/0408017 v3 (2006).

[3] E. Reinhold, R. Buning, U. Hollenstein, A. Ivanchik, P. Petitjean and W. Ubachs, 'Indication of a cosmological variation of the proton-electron mass ratio based on laboratory measurement and reanalysis of H_2 spectra'. *Phys. Rev. Lett.* **96**, 151 101 (2006).

[4] P. Moulton, 'Spectroscopic and laser characteristics of Ti:Al_2O_3'. *J. Opt. Soc. Am. B* **3**, 125 (1986).

[5] P. Brockman, C. H. Bair, J. C. Barnes, R. V. Hess and E. V. Browell, 'Pulsed injection control of a titanium-doped sapphire laser'. *Opt. Lett.* **11**, 712 (1986).

[6] P. Georges, F. Estable, F. Salin, J. P. Poizat, P. Grangier and A. Brun, 'High-efficiency multipass Ti:sapphire amplifiers for a continuous-wave single-mode laser'. *Opt. Lett.* **16**, 144 (1991).

[7] G. A. Rhines and P. Moulton, 'Performance of gain-switched Ti:Al_2O_3 unstable-resonator lasers'. *Opt. Lett.* **15**, 434 (1990).

[8] C. H. Bair, P. Brockman, R. V. Hess and E. A. Modlin, 'Demonstration of frequency control and CW diode laser injection control of a titanium-doped sapphire ring laser with no internal optical elements'. *IEEE J. of Quant. Elec.* **24**, 1045 (1988).

[9] T. D. Raymond and A. V. Smith, 'Injection-seeded titanium-doped-sapphire laser'. *Opt. Lett.* **16**, 33 (1991).

[10] F. Brandi, I. Velchev, D. Neshev, W. Hogervorst and W. Ubachs, 'A narrow-band wavelength-tunable laser system delivering high-energy 300 ps pulses in the near-infrared'. *Rev. Sci. Instrum.* **74**, 32 (2003).

[11] F. Brandi, D. Neshev and W. Ubachs, 'High-order harmonic generation yielding tunable extreme-ultraviolet radiation of high spectral purity'. *Phys. Rev. Lett.* **91**, 163 901 (2003).

[12] R. Seiler, T. Paul, M. Andrist and F. Merkt, 'Generation of programmable near-Fourier-transform-limited pulses of narrow-band laser radiation from the near infrared to the vacuum ultraviolet'. *Rev. Sci. Instrum.* **76**, 103 103 (2005).

[13] P. Dupré and T. A. Miller, 'Quasi-Fourier-transform limited, scannable, high energy Titanium-Sapphire laser source for High Resolution Spectroscopy'. *Rev. Sci. Instrum.* accepted (2007).

[14] C. Wieman and T. W. Hänsch, 'Precision measurement of the 1S Lamb shift and of the 1S – 2S isotope shift of hydrogen and deuterium'. *Phys. Rev. A* **22**, 192 (1980).

[15] K. Danzmann, M. S. Fee and S. Chu, 'Doppler-free laser spectroscopy of positronium and muonium: Reanalysis of the 1S – 2S measurements'. *Phys. Rev. A* **39**, 6072 (1989).

[16] M. S. Fee, K. Danzmann and S. Chu, 'Optical heterodyne measurement of pulsed lasers: Toward high-precision pulsed spectroscopy'. *Phys. Rev. A* **45**, 4911 (1992).

[17] S. Gangopadhyay, N. Melikechi and E. E. Eyler, 'Optical phase perturbations in nanosecond pulsed amplification and second-harmonic generation'. *J. Opt. Soc. Am. B* **11**, 231 (1994).

[18] N. Melikechi, S. Gangopadhyay and E. E. Eyler, 'Phase dynamics in nanosecond pulsed dye laser amplification'. *J. Opt. Soc. Am. B* **11**, 2402 (1994).

[19] I. Reinhard, M. Gabrysch, B. F. von Weikersthal, K. Jungmann and G. zu Putlitz, 'Measurement and compensation of frequency chirping in pulsed dye laser amplifiers'. *Appl. Phys. B* **63**, 467 (1996).

[20] K. S. E. Eikema, W. Ubachs, W. Vassen and W. Hogervorst, 'Lamb shift measurement in the $1\,^1S$ ground state of helium'. *Phys. Rev. A* **55**, 1866 (1997).

[21] P. Bakule, P. E. G. Baird, M. G. Boshier, S. L. Cornish, D. F. Heller, K. Jungmann, I. C. Lane, V. Meyer, P. H. G. Sandars, W. T. Toner, M. Towrie and J. C. Walling, 'A chirp-compensated, injection-seeded alexandrite laser'. *Appl. Phys. B* **71**, 11 (2000).

[22] R. T. White, Y. He, B. J. Orr, M. Kono and K. G. H. Baldwin, 'Control of frequency chirp in nanosecond-pulsed laser spectroscopy. 1. Optical-heterodyne chirp analysis techniques'. *J. Opt. Soc. Am. B* **21**, 1577 (2004).

[23] R. T. White, Y. He, B. J. Orr, M. Kono and K. G. H. Baldwin, 'Control of frequency chirp in nanosecond-pulsed laser spectroscopy. 2. A long-pulse optical parametric oscillator for narrow optical bandwidth'. *J. Opt. Soc. Am. B* **21**, 1586 (2004).

[24] R. T. White, Y. He, B. J. Orr, M. Kono and K. G. H. Baldwin, 'Pulsed injection-seeded optical parametric oscillator with low frequency chirp for high-resolution spectroscopy'. *Opt. Lett.* **28**, 1248 (2004).

[25] R. T. White, Y. He, B. J. Orr, M. Kono and K. G. H. Baldwin, 'Transition from single-mode to multimode operation of an injection-seeded pulsed optical parametric oscillator'. *Opt. Expr.* **12**, 5655 (2004).

[26] T. W. Hänsch and B. Couillaud, 'Laser frequency stabilization by polarization spectroscopy of a reflecting reference cavity'. *Opt. Commun.* **35**, 441 (1980).

[27] S. Hannemann, E. Salumbides, S. Witte, R. T. Zinkstok, K. S. E. Eikema and W. Ubachs, 'Frequency metrology on the EF $^1\Sigma_g^+ \leftarrow X^1\Sigma_g^+$ transition in H_2, HD and D_2'. *Phys. Rev. A* **74**, 062 514 (2006).

[28] S. Hannemann, E. Salumbides, S. Witte, R. T. Zinkstok, K. S. E. Eikema and W. Ubachs, 'Frequency metrology on the Mg $3s^2 - 3s4p$ line for comparison with quasar data'. *Phys. Rev. A* **74**, 012 505 (2006).

[29] E. Salumbides, S. Hannemann, K. S. E. Eikema and W. Ubachs, 'Isotopically resolved calibration of the 285 nm Mg I resonance line for comparison with quasar absorptions'. *Mon. Not. R. Astron. Soc.* **373**, L41 (2006).

[30] W. H. Press, S. A. Teukolsky, W. T. Vetterling and B. P. Flannery, *Numerical Recipies in C, 2nd edition*, Cambridge Univ. Press (1992).

[31] Y. Park, G. Guiliani and R. Byer, 'Single axial mode operation of a Q-switched Nd:YAG oscillator by injection seeding'. *IEEE J. Quantum Electron.* **20**, 117 (1984).

[32] J.-L. Lachambre, P. Lavigne, G. Otis and M. Noël, 'Injection locking and mode selection in TEA-CO_2 laser oscillators'. *IEEE J. Quantum Electron.* **12**, 756 (1976).

[33] M. S. Bowers and S. E. Moody, 'Cavity equations for a laser with an externally injected signal'. *J. Opt. Soc. Am. B* **11**, 2266 (1994).

[34] K. F. Wall, R. L. Aggarwal, M. D. Sciacca, H. J. Zeiger, R. E. Fahey and A. J. Strauss, 'Optically induced nonresonant changes in the refractive index of Ti:Al_2O_3'. *Opt. Lett.* **14**, 180 (1989).

[35] D. W. Chandler and L. R. Thorne, 'Measured radiative lifetimes for H_2 and HD in the EF $^1\Sigma_g^+$ electronic state'. *J. Chem. Phys.* **85**, 1733 (1986).

[36] B. L. Bean and J. R. Izatt, 'Verification of the Kramer-Kronig relations in optically pumped ruby'. *J. Opt. Soc. Am.* **63**, 832 (1973).

[37] R. A. Fisher and W. K. Bischel, 'Numerical studies of the interplay between self-phase modulation and dispersion for intense plane-wave laser pulses'. *J. Appl. Phys.* **46**, 4921 (1975).

[38] S. Hannemann, U. Hollenstein, E.-J. van Duijn and W. Ubachs, 'Production of narrowband tunable extreme-ultraviolet radiation by noncollinear resonance-enhanced four-wave mixing'. *Opt. Lett.* **30**, 1494 (2005).

[39] M. Sneep, S. Hannemann, E. van Duijn and W. Ubachs, 'Deep-UV cavity ring-down spectroscopy'. *Opt. Lett.* **29**, 1378 (2004).

[40] S. Hannemann, E. van Duijn and W. Ubachs, 'Deep-UV high resolution cavity ring-down spectroscopy of the Schumann-Runge bands in $^{16}O_2$ and $^{18}O_2$ at wavelengths 197 – 203 nm'. *J. Mol. Spectrosc.* **232**, 151 (2005).

[41] S. Hannemann, G. Wu, E.-J. van Duijn, W. Ubachs and P. Cosby, 'Pressure broadening and fine-structure dependent predissociation in oxygen $B\,^3\Sigma_u^-$, $v = 0$'. *J. Chem. Phys.* **123**, 174 318 (2005).

[42] W. Demtröder, *Laser spectroscopy, 3*rd *ed.*, Springer, Berlin, Heidelberg, New York (2002).

[43] R. L. Barger and J. L. Hall, 'Pressure shift and broadening of methane line at 3.39 μ studied by laser-saturated molecular absorption'. *Phys. Rev. Lett.* **22**, 4 (1969).

[44] C. Wieman and T. W. Hänsch, 'Doppler-free laser polarization spectroscopy'. *Phys. Rev. Lett.* **36**, 1170 (1976).

[45] B. Cagnac, G. Grynberg and F. Biraben, 'Spectroscopie d'absorption multiphotonique sans effet Doppler'. *J. Phys. France* **34**, 845 (1973).

[46] G. Sagnac, 'Sur la preuve de la réalité de l'éther lumineux par l'expérience de l'interférographe tournant'. *Comptes Rendus Acad. Sci.* **157**, 1410 (1913).

[47] E. J. Post, 'Sagnac Effect'. *Rev. Mod. Phys.* **39**, 475 (1967).

[48] A. Renault, F. Augé-Rochereau, T. Planchon, P. D'Oliveira, T. Auguste, G. Chériaux and J.-P. Chambaret, 'ASE contrast improvement with a nonlinear filtering Sagnac interferometer'. *Opt. Commun.* **248**, 535 (2004).

[49] B.-S. Shi and A. Tomita, 'Generation of a pulsed polarization entangled photon pair using a Sagnac interferometer'. *Phys. Rev. A* **69**, 013 803 (2004).

[50] N. P. Robins, B. J. J. Slagmolen, D. A. Shaddock, J. D. Close and M. B. Gray, 'Interferometric, modulation-free laser stabilization'. *Opt. Lett.* **27**, 1905 (2002).

[51] B. Qi, A. Tausz, L. Qian and H.-K. Lo, 'High-resolution, large dynamic range fiber length measurement based on a frequency-shifted asymmetric Sagnac interferometer'. *Opt. Lett.* **30**, 3287 (2005).

[52] Y. Chen, 'Sagnac interferometer as a speed-meter-type, quantum-nondemolition gravitational-wave detector'. *Phys. Rev. D* **67**, 122 004 (2003).

[53] K.-X. Sun, M. M. Fejer, E. Gustafson and R. L. Byer, 'Sagnac interferometer for gravitational-wave detection'. *Phys. Rev. Lett.* **76**, 3053 (1996).

[54] D. A. Shaddock, 'Operating LISA as a Sagnac interferometer'. *Phys. Rev. D* **69**, 022 001 (2004).

[55] S. Witte, R. Zinkstok, W. Ubachs, W. Hogervorst and K. Eikema, 'Deep ultraviolet quantum-interference metrology with ultrashort laser pulses'. *Science* **307**, 400 (2005).

[56] F. Brandi, W. Hogervorst and W. Ubachs, 'High resolution vacuum-ultraviolet and ultraviolet photionization spectroscopy of krypton'. *J. Phys. B* **35**, 1071 (2002).

[57] R. T. Zinkstok, S. Witte, W. Ubachs, W. Hogervorst and K. S. E. Eikema, 'Frequency comb metrology laser spectroscopy in the vacuum ultraviolet'. *Phys. Rev. A* **73**, 061 801(R) (2006).

[58] M. T. Murphy, J. K. Webb and V. V. Flambaum, 'Further evidence for a variable fine-structure constant from Keck/HIRES QSO absorption spectra'. *Mon. Not. R. Astron. Soc.* **345**, 609 (2003).

[59] M. T. Murphy, J. K. Webb, V. V. Flambaum, V. A. Dzuba, C. W. Churchill, J. X. Prochaska, J. D. Barrow and A. M. Wolfe, 'Possible evidence for a variable fine-structure constant from QSO absorption lines: motivations, analysis and results'. *Mon. Not. R. Astron. Soc.* **327**, 1208 (2001).

[60] R. Srianand, H. Chand, P. Petitjean and B. Aracil, 'Limits on the time variation of the electromagnetic fine-structure constant in the low energy limit from absorption lines in the spectra of distant quasars'. *Phys. Rev. Lett.* **92**, 121 302 (2004).

[61] R. Quast, D. Reimers and S. A. Levashkov, 'Probing the variability of the fine-structure constant with the VLT/UVES'. *Astron. Astroph.* **415**, L7 (2004).

[62] V. Dzuba, V. V. Flambaum and J. K. Webb, 'Space-time variation of physical constants and relativistic corrections in atoms'. *Phys. Rev. Lett.* **82**, 888 (1999).

[63] V. Dzuba, V. V. Flambaum and J. K. Webb, 'Calculations of the relativistic effects in many-electron atoms and space-time variation of fundamental constants'. *Phys. Rev. A* **59**, 230 (1999).

[64] T. P. Ashenfelter, G. J. Mathews and K. A. Olive, 'Chemical evolution of Mg isotopes versus the time variation of the finestructure constant'. *Phys. Rev. Lett.* **92**, 041 102 (2004).

[65] M. G. Kozlov, V. A. Korol, J. C. Berengut, V. A.Dzuba and V. V. Flambaum, 'Space-time variation of the fine-structure constant and evolution of isotope abundances'. *Phys. Rev. A* **70**, 062 108 (2004).

[66] Y. Fenner, M. T. Murphy and B. K. Gibson, 'On variations in the fine-structure constant and stellar pollution of quasar absorption systems'. *Mon. Not. R. Astron. Soc.* **358**, 468 (2005).

[67] J. C. Berengut, V. A. Dzuba, V. V. Flambaum and M. G. Kozlov, 'Configuration-interaction calculation for the isotope shift in Mg I'. *Phys. Rev. A* **69**, 044 102 (2004).

[68] J. C. Berengut, V. V. Flambaum and M. G. Kozlov, 'Calculation of relativistic and isotope shifts in Mg I'. *Phys. Rev. A* **72**, 044 501 (2005).

[69] G. Risberg, 'Spectrum of atomic magnesium Mg I'. *Arkiv Fysik* **28**, 381 (1965).

[70] N. Beverini, E. Maccioni, D. Pereira, F. Strumia, G. Vissani and Y. Z. Wang, 'Wavelength, isotopic shift, and transition rate of the Mg I resonance line'. *Opt. Commun.* **77**, 299 (1990).

[71] J. C. Pickering, A. P. Thorne and J. K. Webb, 'Precise laboratory wavelengths of the Mg I and Mg II resonance transitions at 2853, 2803 and 2796 Å'. *Mon. Not. R. Astron. Soc.* **300**, 131 (1998).

[72] L. Hallstadius, 'Extended measurements of isotope shifts in Mg I'. *Z. Physik A* **291**, 203 (1979).

[73] S. L. Boiteux, A. Klein, J. R. Rios and M. Ducloy, 'Doppler-free spectroscopy and isotopic shift of the Mg I resonance line at 285 nm'. *J. Phys. France* **49**, 885 (1988).

[74] A. Amy-Klein, O. Gorceix, S. L. Boiteux, J. R. RiosLeite and M. Ducloy, 'Doppler-free spectroscopy of Mg using UV-visible saturated absorption'. *Opt. Commun.* **90**, 265 (1992).

[75] H. J. Kluge and H. Sauter, 'Level-crossing experiments in first excited $^1P_1$ states of alkaline earths'. *Zeitschr. f. Physik* **270**, 295 (1974).

[76] S. Witte, R. T. Zinkstok, W. Hogervorst and K. Eikema, 'Control and precise measurement of carrier-envelope phase dynamics'. *Appl. Phys. B* **78**, 5 (2004).

[77] T. N. Chang, 'Radiative lifetimes of the bound excited states of magnesium and beryllium'. *Phys. Rev. A* **41**, 4922 (1990).

[78] J. Steiner and L. J. Curtis, 'Branching fractions for the Mg-like 3s3p – 3s3d and 3s3p – $3p^2$ transition arrays'. *J. Phys. B* **37**, 3771 (2004).

[79] H. Knöckel, B. Bodermann and E. Tiemann, 'High precision description of the rovibronic structure of the I_2 B – X spectrum'. *Eur. J. Phys. D* **28**, 199 (2004).

[80] These calculations were performed by L. Veseth (University of Oslo) and kindly made available to us.

[81] K. J. R. Rosman and P. D. Taylor, 'Isotopic compositions of the elements 1997'. *Pure & Appl. Chem.* **70**, 217 (1998).

[82] M. Aldenius, S. Johansson and M. T. Murphy, 'Accurate laboratory ultraviolet wavelengths for quasar absorption-line constraints on varying fundamental constants'. *Mon. Not. R. Astron. Soc.* **370**, 444 (2006).

[83] E. E. Eyler, 'Tests of basic molecular physics using high-resolution laser spectroscopy of H_2'. *Comments At. Mol. Phys.* **24**, 299 (1990).

[84] B. P. Stoicheff, 'On the dissociation energy of molecular hydrogen'. *Can. J. Phys.* **79**, 165 (2001).

[85] W. Kołos, 'Extrapolated Born-Oppenheimer energy for the ground state of the hydrogen molecule'. *J. Chem. Phys.* **101**, 1330 (1994).

[86] L. Wolniewicz, 'Nonadiabatic energies of the ground state of the hydrogen molecule'. *J. Chem. Phys.* **103**, 1792 (1995).

[87] A. Balakrishnan, V. Smith and B. P. Stoicheff, 'Dissociation energy of the hydrogen molecule'. *Phys. Rev. Lett.* **68**, 2149 (1992).

[88] E. F. McCormack and E. E. Eyler, 'Perturbed structure of molecular hydrogen near the second dissociation limit'. *Phys. Rev. Lett.* **66**, 1042 (1991).

[89] Y. P. Zhang, C. H. Cheng, J. T. Kim, J. Stanojevic and E. E. Eyler, 'Dissociation energies of molecular hydrogen and the hydrogen molecular ion'. *Phys. Rev. Lett.* **92**, 203 003 (2004).

[90] G. M. Greetham, U. Hollenstein, R. Seiler, W. Ubachs and F. Merkt, 'High-resolution VUV photoionization spectroscopy of HD between the $X\,^2\Sigma^+$ $v^+ = 0$ and $v^+ = 1$ thresholds'. *Phys. Chem. Chem. Phys.* **5**, 2528 (2003).

[91] A. de Lange, E. Reinhold and W. Ubachs, 'Precision spectroscopy on some *g* symmetry states in H_2 and determination of the ionization potential'. *Phys. Rev. A* **65**, 064 501(R) (2002).

[92] C. Jungen, I. Dabrowksi, G. Herzberg and M. Vervloet, 'High orbital angular momentum states in H_2 and D_2. III. Singlet-triplet splittings, energy levels, and ionization potentials'. *J. Chem. Phys.* **93**, 2289 (1990).

[93] W. L. Glab and J. P. Hessler, 'Multiphoton excitation of high singlet np Rydberg states of molecular hydrogen: spectroscopy and dynamics'. *Phys. Rev. A* **35**, 2102 (1987).

[94] E. E. Eyler, J. Gilligan, E. F. McCormack, A. Nussenzweig and E. Pollack, 'Precise two-photon spectroscopy of E ← X* intervals in H_2'. *Phys. Rev. A* **36**, 3486 (1987).

[95] E. F. McCormack, J. M. Gilligan, C. Cornaggia and E. E. Eyler, 'Measurement of high Rydberg states and the ionization potential of H_2'. *Phys. Rev. A* **39**, 2260 (1989).

[96] J. M. Gilligan and E. E. Eyler, 'Precise determinations of ionization potentials and EF-state energy levels of H_2, HD, and D_2'. *Phys. Rev. A* **46**, 3676 (1992).

[97] D. Shiner, J. M. Gilligan, B. M. Cook and W. Lichten, 'H_2, D_2, and HD ionization potentials by accurate calibration of several iodine lines'. *Phys. Rev. A* **47**, 4042 (1993).

[98] M. Vervloet and D. Bailly, private communication.

[99] A. Osterwalder, A. Wuest, F. Merkt and C. Jungen, 'High-resolution millimeter wave spectroscopy and multichannel quantum defect theory of the hyperfine structure in high Rydberg states of molecular hydrogen H_2'. *J. Chem. Phys.* **121**, 11 810 (2004).

[100] A. Yiannopoulou, N. Melikechi, S. Gangopadhay, J. C. Meiners, C. H. Cheng and E. E. Eyler, 'Determinations of EF $^1\Sigma_g^+ \leftarrow$ X $^1\Sigma_g^+$ transition frequencies in H_2, D_2, and HD'. *Phys. Rev. A* **73**, 022 506 (2006).

[101] Database and program for calculating absolute frequencies of hyperfine components in the I_2 saturation spectrum kindly provided by Dr. Knöckel, the University of Hannover; see also Ref. [79].

[102] M. J. J. Vrakking, A. S. Bracker, T. Suzuki and Y. T. Lee, 'Ultrasensitive detection of hydrogen molecules by (2+1) resonance-enhanced multiphoton ionization'. *Rev. Sci. Instrum.* **64**, 645 (1993).

[103] R. W. Boyd, *Nonlinear Optics*, Academic Press, San Diego (1992), ISBN 0 12 121680 2.

[104] H. Li, F. Zhou, X. Zhang and W. Ji, 'Bound electronic Kerr effect and self-focusing induced damage in second-harmonic-generation crystals'. *Opt. Commun.* **144**, 75 (1997).

[105] R. DeSalvo, D. J. Hagan, M. Sheik-Bahae, G. Stegeman, E. W. van Stryland and H. Vanherzelle, 'Self-focusing and self-defocusing by cascaded second-order effects in KTP'. *Opt. Lett.* **17**, 28 (1992).

[106] E. Jones, T. Olifant and P. Peterson, 'SciPy: Open source scientific tools for Python', http://www.scipy.org/ (2000).

[107] G. C. Bjorklund, 'Effects of focusing on third-order nonlinear processes in isotropic media'. *IEEE J. Quant. Electr.* **6**, 287 (1975).

[108] G. Hilber, A. Lago and R. Wallenstein, 'Broadly tunable vacuum-ultraviolet/extreme-ultraviolet radiation generated by resonant third-order frequency conversion in krypton'. *J. Opt. Soc. Am. B* **4**, 1753 (1987).

[109] J. P. Marangos, N. Shen, H. Ma, M. H. R. Hutchinson and J. P. Connerade, 'Broadly tunable vacuum-ultraviolet radiation source employing resonant enhanced sum difference frequency mixing in krypton'. *J. Opt. Soc. Am. B* **7**, 1254 (1990).

[110] K. Miyazaki, H. Sakai and T. Sato, '2-Photon resonances in Xe and Kr for the generation of tunable coherent extreme UV-radiation'. *App. Opt.* **28**, 699 (1989).

[111] E. Cromwell, T. Trickl, Y. T. Lee and A. H. Kung, 'Ultranarrow bandwidth VUV-XUV laser system'. *Rev. Sci. Instr.* **60**, 2888 (1989).

[112] U. Hollenstein, H. Palm and F. Merkt, 'A broadly tunable extreme ultraviolet laser source with a $0.008\,\mathrm{cm}^{-1}$ bandwidth'. *Rev. Sci. Instr.* **71**, 4023 (2000).

[113] A. Eckbreth, 'BOXCARs - crossed-beam phase-matched CARs generation in gases'. *Appl. Phys. Lett.* **32**, 421 (1978).

[114] W. Ubachs, K. S. E. Eikema, W. Hogervorst and P. C. Cacciani, 'Narrowband tunable extreme-ultraviolet laser source for lifetime measurements and precision spectroscopy'. *J. Opt. Soc. Am. B* **14**, 2469 (1997).

[115] P. C. Hinnen, W. Hogervorst, S. Stolte and W. Ubachs, 'Sub-Doppler laser spectroscopy of H_2 and D_2 in the range 91 – 98 nm'. *Can. J. Phys.* **72**, 1032 (1994).

[116] W. Ubachs and E. Reinhold, 'Highly accurate H_2 Lyman and Werner band laboratory measurements and an improved constraint on a cosmological variation of the proton-to-electron mass ratio'. *Phys. Rev. Lett.* **92**, 101 302 (2004).

[117] T. Namioka, 'Absorption spectra of H_2 in the vacuum-ultraviolet region. I. The Lyman and the Werner bands'. *J. Chem. Phys.* **40**, 3154 (1964).

[118] H. Abgrall, E. Roueff, J.-Y. Roncin and J.-L. Subtil, 'Table of the Lyman band system of molecular hydrogen'. *Astr. & Astroph. Suppl. Series* **101**, 273 (1993).

[119] H. Abgrall, E. Roueff, J.-Y. Roncin and J.-L. Subtil, 'The Lyman and Werner band systems of molecular hydrogen'. *J. Mol. Spectr.* **157**, 512 (1993).

[120] D. E. Jennings, S. L. Bragg and J. W. Brault, 'The $v = 0 - 0$ spectrum of H_2'. *Astroph. J.* **282**, L85 (1984).

[121] W. Ubachs, K. S. E. Eikema and W. Hogervorst, 'Narrowband extreme ultraviolet radiation tunable in the range 90.5 – 95 nm: application to spectroscopy of N_2'. *Appl. Phys. B* **57**, 411 (1993).

[122] P. K. Carroll, C. P. Collins and K. Yoshino, 'The high energy $^1\Sigma_u^+$ states of N_2'. *J. Phys. B* **3**, L127 (1970).

[123] J.-Y. Roncin, J.-L. Subtil and F. Launay, 'The high-resolution vacuum ultraviolet emission spectrum of molecular nitrogen from 82.6 – 124.2 nm: level energies of 10 excited singlet electronic states'. *J. Mol. Spectr.* **188**, 128 (1998).

[124] A. O'Keefe and D. Deacon, 'Cavity ring-down optical spectrometer for absorption measurements using pulsed laser sources'. *Rev. Sci. Instrum.* **59**, 2544 (1988).

[125] R. Engeln, E. van den Berg, G. Meijer, L. Lin, G. M. H. Knippels and A. F. G. van der Meer, 'Cavity ring down spectrocopy with a free-electron laser'. *Chem. Phys. Lett.* **269**, 293 (1997).

[126] G. Berden, R. Peeters and G. Meijer, 'Cavity ring-down spectroscopy: Experimental schemes and applications'. *Int. Rev. in Phys. Chem.* **19**, 565 (2000).

[127] P. Zalicki, Y. Ma, R. N. Zare, E. H. Wahl, J. R. Dadamio, T. G. Owano and C. H. Kruger, 'Methyl radical measurement by cavity ring-down spectroscopy'. *Chem. Phys. Lett.* **234**, 269 (1995).

[128] R. T. Jongma, M. G. H. Boogaarts, I. Holleman and G. Meijer, 'Trace gas detection with cavity ring down spectroscopy'. *Rev. Sci. Instrum.* **66**, 2821 (1995).

[129] H. Naus and W. Ubachs, 'Experimental verification of Rayleigh scattering cross sections'. *Opt. Lett.* **25**, 347 (2000).

[130] H. Naus, I. H. M. van Stokkum, W. Hogervorst and W. Ubachs, 'Quantitative analysis of decay transients applied to a multimode pulsed cavity ring-down experiment'. *Appl. Opt.* **40**, 4416 (2001).

[131] M. Ogawa, 'Absorption cross sections of O_2 and CO_2 continua in the Schumann and far-UV regions'. *J. Chem. Phys.* **54**, 2550 (1971).

[132] D. Vukovic, G. A. Woolsey and G. B. Scelsi, 'Refractivities of SF_6 and SOF_2 at wavelengths of 632.99 and 1300 nm'. *J. Phys. D* **29**, 634 (1996).

[133] N. J. Bridge and A. D. Buckingham, 'The polarization of laser light scattered by gases'. *Proc. R. Soc. A.* **295**, 334 (1966).

[134] B. R. Lewis, S. T. Gibson and P. M. Dooley, 'Fine-structure dependence of predissociation linewidth in the Schumann-Runge bands of molecular oxygen'. *J. Chem. Phys.* **100**, 7012 (1994).

[135] M. Coquart, M.-F. Mérienne and A. Jenouvrier, 'O_2 Herzberg continuum absorption cross-sections in the wavelength region 196 – 205 nm of the Schumann Runge bands'. *Planet. Space Sci.* **38**, 287 (1990).

[136] A. J. Blake and D. G. McCoy, 'The pressure dependence of the Herzberg photoabsorption continuum of oxygen'. *J. Quant. Spectrosc. Radiat. Transfer* **38**, 113 (1987).

[137] P. Brix and G. Herzberg, 'Fine structure of the Schumann-Rungs bands near the convergence limit and the dissociation energy of the oxygen molecule'. *Can. J. Phys.* **32**, 110 (1954).

[138] M. Ackerman and F. Biaume, 'Structure of the Schumann-Runge bands from the 0 – 0 to the 13 – 0 band'. *J. Mol. Spectrosc.* **35**, 73 (1970).

[139] K. Yoshino, D. E. Freeman, J. R. Esmond and W. H. Parkinson, 'High resolution absorption cross section measurements and band oscillator strengths of the (1,0) – (12,0) Schumann-Runge bands of O_2'. *Planet. Space Sci.* **31**, 339 (1983).

[140] K. Yoshino, D. E. Freeman and W. H. Parkinson, 'Atlas of the Schumann-Runge absorption bands of O_2 in the wavelength region 175 – 205 nm'. *J. Phys. Chem. Ref. Data* **13**, 207 (1984).

[141] A. S.-C. Cheung, K. Yoshino, W. H. Parkinson and D. E. Freeman, 'Herzberg continuum cross-section of oxygen in the wavelength region 193.5 – 204.0 nm and band oscillator-strengths of the (0,0) and (1,0) Schumann-Runge bands'. *Can. J. Phys.* **62**, 1752 (1984).

[142] A. S.-C. Cheung, K. Yoshino, W. H. Parkinson and D. E. Freeman, 'Molecular spectroscopic constants of O_2 ($B\,^3\Sigma_u^-$) - the upper state of the Schumann-Runge bands'. *J. Mol. Spectrosc.* **119**, 1 (1986).

[143] K. Yoshino, D. E. Freeman, J. R. Esmond and W. H. Parkinson, 'High resolution absorption cross-sections and band oscillator strengths of the Schumann-Runge bands of oxygen at 79 K'. *Planet. Space Sci.* **35**, 1067 (1987).

[144] A. S.-C. Cheung, K. Yoshino, D. E. Freeman and W. H. Parkinson, 'Wavelength measurement and analysis of the Schumann-Runge absorption bands of $^{18}O_2$ in the region 175 – 205 nm'. *J. Mol. Spectrosc.* **131**, 96 (1988).

[145] A. S.-C. Cheung, K. Yoshino, D. E. Freeman, R. S. Friedman and W. H. Parkinson, 'The Schumann-Runge absorption bands of $^{16}O^{18}O$ in the wavelength region 175 – 205 nm and spectroscopic constants of isotopic oxygen molecules'. *J. Mol. Spectrosc.* **134**, 362 (1989).

[146] T. Matsui, A. S.-C. Cheung, K. W.-S. Leung, K. Yoshino, W. H. A. P. Thorne, J. E. Murray, K. Ito and T. Imajo, 'High resolution absorption cross-section measurements of the Schumann-Runge bands of O_2 by VUV Fourier transform spectroscopy'. *J. Mol. Spectrosc.* **219**, 45 (2003).

[147] A. S.-C. Cheung, D. K.-W. Mok, Y. Sun and D. E. Freeman, 'The potential energy curve for the $B\,^3\Sigma_u^-$ state of oxygen and accurate Franck-Condon factors for the Schumann-Runge bands'. *J. Mol. Spectrosc.* **163**, 9 (1994).

[148] H. Naus and W. Ubachs, 'The $b\,^1\Sigma_g^+ \leftarrow X\,^3\Sigma_g^-$ (3,0) band of $^{16}O_2$ and $^{18}O_2$'. *J. Mol. Spectrosc.* **193**, 442 (1999).

[149] I. Velchev, R. van Dierendonck, W. Hogervorst and W. Ubachs, 'A dense grid of reference iodine lines for optical frequency calibration in the range 571 – 596 nm'. *J. Mol. Spectrosc.* **187**, 21 (1998).

[150] G. Rouillé, G. Millot, R. Saint-Loup and H. Berger, 'High-resolution stimulated Raman spectroscopy of O_2'. *J. Mol. Spectrosc.* **154**, 372 (1992).

[151] H. Naus, A. de Lange and W. Ubachs, '$b\,^1\Sigma_g^+ - X\,^3\Sigma_g^-$ (0,0) band of oxygen isotopomers in relation to tests of the symmetrization postulate in $^{16}O_2$'. *Phys. Rev. A* **56**, 4755 (1997).

[152] H. Naus, S. J. van der Wiel and W. Ubachs, 'Cavity-ring-down spectroscopy on the $b\,^1\Sigma_g^+ - X\,^3\Sigma_g^-$ (1,0) band of oxygen isotopomers'. *J. Mol. Spectrosc.* **192**, 162 (1998).

[153] H. Naus, K. Navaian and W. Ubachs, 'The gamma-band of $^{16}O_2$, $^{16}O^{17}O$, $^{17}O_2$ and $^{18}O_2$'. *Spectrochimica Acta* **55**, 1255 (1999).

[154] W. Steinbach and W. Gordy, 'Microwave spectrum and molecular constants of $^{16}O^{18}O$'. *Phys. Rev. A* **11**, 729 (1975).

[155] J. Rosenfield, 'The sensitivity of stratospheric photodissociation rates to the solar spectral resolution in the Schumann-Runge bands'. *J. Atm. Terrestr. Phys.* **57**, 847 (1995).

[156] B. R. Lewis, L. Berzins, J. H. Carver and S. T. Gibson, 'Rotational variation of predissociation linewidth in the Schumann-Runge bands of $^{16}O_2$'. *J. Quant. Spectr. Rad. Transfer* **36**, 187 (1986).

[157] B. R. Lewis, L. Berzins and J. H. Carver, 'Oscillator-strengths for the Schumann-Runge bands of $^{16}O^{18}O$'. *J. Quant. Spectr. Rad. Transfer* **37**, 219 (1987).

[158] B. R. Lewis, L. Berzins and J. H. Carver, 'Predissociation linewidths for the Schumann-Runge bands of $^{18}O_2$'. *J. Quant. Spectr. Rad. Transfer* **37**, 229 (1987).

[159] A. S.-C. Cheung, K. Yoshino, J. R. Esmond, S.-L. Chiu, D. E. Freeman and W. H. Parkinson, 'Predissociation linewidths of the (1,0) – (12,0) Schumann-Runge absorption bands of O_2 in the wavelength region 179 – 202 nm'. *J. Chem. Phys.* **92**, 842 (1990).

[160] S. S.-L. Chiu, A. S.-C. Cheung, K. Yoshino, J. R. Esmond, D. E.Freeman and W. H. Parkinson, 'Predissociation linewidths of the (3,0) – (11,0) Schumann-Runge absorption bands of $^{18}O_2$ and $^{16}O^{18}O$ in the wavelength region 180 – 196 nm'. *J. Chem. Phys.* **93**, 5539 (1990).

[161] X. Yang, A. Wodtke and L. Hüwel, 'Direct observation of orbit rotation predissociation in the O_2 Schumann-Runge system'. *J. Chem. Phys.* **94**, 2469 (1990).

[162] P. S. Julienne, '$^3\Sigma_u^- - {}^3\Sigma_u^+$ coupling in the O_2 $B\,^3\Sigma_u^-$ predissociation'. *J. Mol. Spectrosc.* **63**, 60 (1976).

[163] S. S.-L. Chiu, A. S.-C. Cheung, M. Finch, M. J. Jamieson, K. Yoshino and W. H. Parkinson, 'Predissociation of oxygen in the $B\,^3\Sigma_u^-$ state'. *J. Chem. Phys.* **97**, 1787 (1992).

[164] A. S.-C. Cheung, D. K.-W. Mok, M. J. Jamieson, M. Finch, K. Yoshino, A. Dalgarno and W. H. Parkinson, 'Rotational dependence of the predissociation linewidths of the Schumann-Runge bands of O_2'. *J. Chem. Phys.* **99**, 1086 (1993).

[165] A. S.-C. Cheung, D. K.-W. Mok, K. Yoshino, W. H. Parkinson, M. J. Jamieson, A. Dalgarno and M. S. Child, 'Isotopic dependence of predissociation linewidths in the Schumann-Runge bands of oxygen'. *J. Chem. Phys.* **103**, 2369 (1995).

[166] G. S. M. Tong, A. S.-C. Cheung and M. J. Jamieson, 'Predicted predissociation linewidths in the Schumann-Runge bands of O_2 compared with recent high resolution measurements'. *J. Chem. Phys.* **114**, 7969 (2001).

[167] P. M. Dooley, B. R. Lewis, S. T. Gibson, K. G. H. Baldwin, P. C. Cosby, J. L. Price, R. A. Copeland, T. G. Slanger, A. P. Thorne, J. E. Murray and K. Yoshino, 'A comparative high-resolution study of predissociation linewidths in the Schumann-Runge bands of O_2'. *J. Chem. Phys.* **109**, 3856 (1998).

[168] Y. Li, H.-P. Liebermann and R. J. Buenker, '*Ab initio* calculation of predissociation linewidths in the Schumann-Runge bands of the oxygen molecule'. *J. Chem. Phys.* **114**, 10 396 (2001).

[169] P. C. Cosby, H. Park, R. A. Copeland and T. G. Slanger, 'Predissociation linewidths in O_2 $B\,^3\Sigma_u^-$ $(v = 0, 2)$'. *J. Chem. Phys.* **98**, 5117 (1993).

[170] B. R. Lewis, L. Berzins, C. J. Dedman, T. T. Scholz and J. H. Carver, 'Pressure-broadening in the Schumann-Runge bands of molecular oxygen'. *J. Quant. Spectr. Rad. Transfer* **39**, 271 (1988).

[171] P. M. Dooley, K. Waring, S. T. Gibson and K. G. H. Baldwin, 'Fine-structure-resolved collisional broadening in the Schumann-Runge bands of O_2'. *J. Quant. Spectr. Rad. Transfer* **58**, 93 (1997).

[172] B. R. Lewis and S. T. Gibson, 'Comment on "The potential energy function for O_2 X $(^3\Sigma_g^-)$ and the transition dipole moment of the Schumann-Runge band near X state dissociation"'. *J. Chem. Phys.* **93**, 7532 (1990).

Acknowledgments

This thesis would not be what it is if there have not been so many people supporting it. Wim Ubachs, has given me the opportunity to work on this interesting project in the Laser Centre. You have always been around, coming up with new ideas, giving encouraging and critical comment where ever appropriate. You were the first person consequently talking Dutch to me, which finally helped me much to get started speaking it as well. When it comes to paper writing, your replies to drafts are finished within an astonishing short period of time.

Eric-Jan van Duijn, my co-promoter, was always a very helpful colleague, and I am not just talking about the amounts of equipment that you offered (I hope not too often sacrificed) for our lab, but also your encouraging attitude, at the more difficult times.

Dragomir Neshev has given me support during the first half year's period when Wim was at sabbatical. The introduction into the "real" lasers, i.e. the bulky pulsed lasers in the XUV section of the lab, I received from you, as well as a number of instructions on how to deal with infrared lasers. Also Fernando Brandi, "senior" PhD student when I started, was always available for immediate discussions and beginner's questions.

Arjan Sprengers and Josselin Philipp alias 'Riri and Jojo Lapin' deserve a special note here, as the funny couple at the neighbouring experiment, cursing in French 'Tu es stupide!' and always being ready for all kinds of strange jokes. Hilarious working atmosphere was guaranteed having you around.

Urs Hollenstein, the Swiss influence in the lab, offering croissants in the morning coffee break, telling memorable stories of the Swiss army service, knowing everything about the tiniest details of typesetting math and physical quantities. You actually convinced me of using XMGRACE, which I am still doing.

Maarten Sneep wrote a LABVIEW program for cavity ring-down spectroscopy which I was using as well. You were the next person to teach me some Dutch, most notably the infamous bits of the language ;-). Guorong Wu dropped by for a couple of months working with me on the Schumann-Runge spectroscopy and the time consuming ytterbium scans.

Edcel John Salumbides joined in autumn 2004 linking the Ti:sapphire laser system with the femto-lab. I must say, that I am really happy that everything worked out so nicely since then. Not only, that a bunch of nice papers are a sign of good and productive working spirit, but also those never ending night shifts were a lot of fun

with a colleague always being prepared to pull some crazy prank, and being "tuned to the same wavelength", as we say in German.

Kjeld Eikema, Roel Zinkstok, and Stefan Witte — our femto-gurus — were always available for technical questions, for hours of aligning the frequency comb, when the "beatnote was pathetic" once again, and for showing the tricky bits of the system. Not to forget that this PYTHON-infection I contracted came definitely from your side of the lab.

Jacques Bouma, our technician, has a very efficient philosophy: good solutions are quick, easy, and flexible; good equipment has to fulfil the rule: everything fits on everything. Polyflow and standardized equipment make a complete change from one atomic beam setup to an entirely different one a matter of one or two days! Just to list the typical changes: the vacuum pumps from oily diffusion and rotary vane pumps to dry turbo and membrane pumps, the filament heated oven source to a pulsed gas valve, and the detection scheme from LIF to TOF ion extraction. I think this is quite unique and very practical.

A lot of people were around during my time at the VU, available for a chat or for discussions, and playing an important role in maintaining the nice working atmosphere in the Laser Centre: Martynas Barkauskas, Rick Bethlem, Ruth Buning, Petra de Gijssel, Norbert Herschbach, Toncho Ivanov, Dmitry Ityaksov, Tom Jeltes, Harold Linnartz, Dominik Kandula, Jeroen Koelemeij, John McNamara, Joop Mes, Elmar Reinhold, Amandine Renault, Mourad Roudjane, Lineke van der Sneppen, Paul Tol, Andrej Tychkov, Wim Vassen, Ofelia Vieitez, Anne-Lisa Wolf, and more.

Special thanks go to Gordon and Bernd for doing major contributions to the layout of the book cover and invitation card.

Last but not least my wife's contribution cannot be overestimated. You have always made everything possible to support my research, which allowed me to carry out round-the-clock shifts in the lab and to spend countless weekends of writing. Thank you so much.

List of Publications

The following publications are reproduced in the thesis:

i) S. Sneep, S. Hannemann, E.-J. van Duijn and W. Ubachs, 'Deep-UV Cavity Ring-Down Spectroscopy'. *Opt. Lett.* **30**, 1378 (2004).

ii) S. Hannemann, U. Hollenstein, E.-J. van Duijn, and W. Ubachs, 'Production of narrowband tunable extreme-ultraviolet radiation by noncollinear resonance-enhances four-wave mixing'. *Opt. Lett.* **30**, 1494 (2005).

iii) S. Hannemann, E.-J. van Duijn, and W. Ubachs, ' Deep-UV high resolution cavity ring-down spectroscopy of the Schumann-Runge bands in $^{16}O_2$ and $^{18}O_2$ at wavelength 197 – 203 nm'. *J. Mol. Spectrosc.* **232**, 151 (2005).

iv) S. Hannemann, G. Wu, E.-J. van Duijn, W. Ubachs, and P. Cosby, 'Pressure broadening and fine-structure dependent predissociation in oxygen B $^3\Sigma_u^-$, $v = 0$'. *J. Chem. Phys.* **123**, 174 318 (2005).

v) S. Hannemann, E. J. Salumbides, S. Witte, R. Th. Zinkstok, K. S. E. Eikema, and W. Ubachs, 'Frequency metrology on the Mg $3s^2$ – 3s4p line for comparison with quasar data'. *Phys. Rev. A* **74**, 012 505 (2006).

vi) S. Hannemann, E. J. Salumbides, S. Witte, R. Th. Zinkstok, K. S. E. Eikema, and W. Ubachs, 'Frequency metrology on the EF $^1\Sigma_g^+ \leftarrow$ X $^1\Sigma_g^+$ transition in H_2, HD, and D_2'. *Phys. Rev. A* **74**, 062 514 (2006).

vii) S. Hannemann, E. J. Salumbides, and W. Ubachs, 'Reducing first order Doppler shifts in a Sagnac interferometer'. accepted, *Opt. Lett.*, (2007).

Furthermore, the author contributed to the following papers:

viii) E. J. Salumbides, S. Hannemann, K. S. E. Eikema, and W. Ubachs, 'Isotopically resolved calibration of the 285 nm Mg I resonance line for comparison with quasar absorption'. *Mon. Notices Roy. Astr. Soc.* **373**, L41 (2006).

ix) J. Kleinert, S. Hannemann, U. Eisenbarth, B. Eike, M. Grieser and R. Grimm, G. Gwinner, S. Karpuk, G. Saathoff, U. Schramm and D. Schwalm, M. Weidemüller, 'Laser-Cooled Ions and Atoms in a Storage Ring'. *Hyperf. Int.* **146**, 189 (2003).

x) G. Saathoff, U. Eisenbarth, S. Hannemann, I. Hoog, G. Huber and M. Grieser, S. Karpuk, S. Krohn, J. Lassen, D. Schwalm and M. Weidemüller, G. Gwinner, 'Towards a new test of the relativistic time dilation factor by laser spectroscopy of fast ions in a storage ring'. *Hyperf. Int.* **146**, 71 (2003).

xi) S. Hannemann, 'Laser cooling of coasting Be^+-ion beams', *Diplomarbeit*, MPI H-V5-2002 (2002).